LIQUID FLOW MEASUREMENT: FROM INLINE HYDROCEPHALUS SHUNT FLOW MONITOR TO FLOWMETRY IN THE NANOLITER/MINUTE SCALE.

by

CHUCHU QIN

Presented to the Faculty of the Graduate School of

The University of Texas at Arlington in Partial Fulfillment

of the Requirements

for the Degree of

DOCTOR OF PHILOSOPHY

THE UNIVERSITY OF TEXAS AT ARLINGTON

August 2019

Acknowledgments

I am extremely fortunate to have Dr. Purnendu K. Dasgupta as my mentor during the long journey of the doctoral program. His never-ending supply of new ideas and enthusiasm for research was a huge source of inspiration for me. His persistence in research encouraged me to overcome so many obstacles in my work. He guided me to turn the impossible into the possible. I greatly appreciate the opportunity to work with him.

I would like to thank my committee members, Dr. Daniel W. Armstrong, Dr. Kevin A. Schug and Dr. Hyejin Moon for their time and valuable suggestions on this dissertation.

I am very grateful to Dr. Mallet, Dr. Yurvati and researchers from UNT health science center. Thanks them for being so supportive, responsive and encourages.

I have encountered so many wonderful and talented labmates during graduate school. I would like to extend my sincerest thanks to all of these people for their friendship and support. Special thanks to Phillip, Brian, Dr. Huang, Hongzhu, Min and Akinde. They have helped define who I am in research and getting me to this point. Thank you Fereshteh, Bikash, Sajad, Stephanie, Mai and Noohn.

July 23, 2019

Abstract

LIQUID FLOW MEASUREMENT: FROM INLINE HYDROCEPHALUS SHUNT FLOW MONITOR TO FLOWMETRY IN THE NANOLITER/MINUTE SCALE.

CHUCHU QIN, PhD

The University of Texas at Arlington, 2019

Supervising Professor: Purnendu K. Dasgupta

This dissertation primarily focuses on designing and developing novel sensing strategies and instruments for ultra-low liquid flow measurement.

An inline thermal flow sensor based on a single common thermistor has been developed to quantitatively measures cerebral spinal fluid flow rate in hydrocephalus shunt. The technique facilitates the diagnosis of shunt failure due to blockage or over-drainage. This allows timely remediation of shunt-flow malfunctions, thereby avoiding severe complications that can arise.

The thermal flow sensor utilizes the bidirectional ability of the thermistor to both heat the surrounding and to sense the temperature. The net temperature change from immediately before and after the heat pulse, along with the surrounding temperature was used to predict the flow rate between 0-52.5 mL/h at 32-39 ˚C with 6.3% RMS relative error. The functionality of the flow monitor has been verified on a healthy pig model. Six of eight tests with experimental pigs were successfully conducted with > 4300 acceptable flow measurements. Very good correlation was observed between measured and predicted flow rates (r > 0.9). The average slope of measured vs predicted flow rates was 1.04 ± 0.15, indicating that the flow monitor accurately measured porcine CSF flow.

Precise flowmetry is essential for the overall reliability and integrity of analytical systems. Nowadays, many capillary scale analytical approaches operate at flow rates below 25 nL/min. At this level, any leak evaporates long before it is visible. An affordable monitor applicable in this flow regime can greatly facilitate instrument/method development as well as help troubleshoot processes that operate in this flow scale.

Thus, we developed a flow measurement technique works in the 1.5-15 nL/min flow range with good precision (<1% RSD). The motion of a conductive/nonconductive immiscible segmental interface in a capillary is followed by an admittance detector in a fluorosilylated fused silica capillary flow cell. A four-port valve was used to change the flow direction in the flow cell so that flow marker moves back-and-forth across the admittance detector, triggers a series of flow analysis. Three flow-depended features were studied, each providing good linear relationships with flow rate ($R^2 > 0.995$). The useful range of flow rate can easily be changed if needed, simply by using a larger or smaller inner diameter fused silica capillary as a flow cell. In a single capillary, the measurement range can be widened by introducing multiple different length conductive liquid segments segregated by fluorocarbon.

Table of Contents

List of Illustrations

List of Tables

Chapter 1

INTRODUCTION

This dissertation primarily focuses on designing and developing liquid flow sensing strategy and electronic instruments, expressed in two independent projects: (1) Inline shunt flow monitor for hydrocephalus; and (2) time of sight liquid flow measurements in the low nanoliter per minute scale.

The first project is composed of two parts: Part I consist of the principles, electronics, and functionality of the hydrocephalus flow sensor on benchtop. Part II is the application of hydrocephalus flow sensor in animal tests. These two parts are based on the following papers: *Analytical Chemistry* 2017, 89 (15), 8170-8176(1) and *Medical engineering & physics* 2019, 67, 66-72(2). Part I and II are reproduced as they were published in chapter 2 and 3, respectively.

The second project is discussed in chapter 4.

The other project I participated, “attenuation coefficients of tubular conduits for liquid phase absorbance measurement. Shot noise-limited optimum pathlength”, is included in appendix B since it is not directly related to flow rate measurement. This work is reproduced from the paper: DOI:10.1021/acs.analchem.9b00067.

The brief introduction for chapter 2, 3, 4 and appendix B are given below.

Chapter 2: In hydrocephalus, cerebrospinal fluid (CSF) builds up in the cranial cavity causing swelling of the head and potentially brain damage. A shunt to drain the fluid into a body cavity is now universally used, but failure is all too common. Techniques for ascertaining shunt failure are time-consuming, expertise-dependent, and often inconclusive. We report here an inline system that reliably and quantitatively measures the CSF flow rate. The system uses a single thermistor to both heat the surrounding and to sense the temperature. In the heating mode, the thermistor is subjected to a 5 s

voltage pulse. In the sensing mode, it is part of a Wheatstone's bridge, the output being proportional to temperature. The signal, $V_i - V_f$, which is the net change ΔV in the bridge output immediately before and after the heat pulse, depends both on the flow rate and the surrounding temperature. In vitro, a single equation, flow rate = $3.75 \times 10^{-6} \times \Delta V^{(-9.568+1.088Vi)}$ provided a good prediction for the flow rate, with 6.3% RMS relative error. The sensor behavior is reported for flow rates between 0–52.5 mL/h at 32–39 °C, adequately covering the range of interest.

Chapter 3: Shunts are commonly employed to treat hydrocephalus, a severe central nervous disease caused by the buildup of cerebrospinal fluid in the brain. These shunts divert excessive cerebrospinal fluid from brain ventricles to other body cavities, thereby relieving the symptoms. However, these shunts are highly prone to failure due to obstruction from cellular debris, leading to cerebrospinal fluid accumulation in the brain and exacerbation of neurological symptoms. Therefore, there is a clinical need for a reliable, non-invasive method of monitoring shunt performance. Recently, a simple inline flow sensor was reported for monitoring ventriculoperitoneal shunting of cerebrospinal fluid in hydrocephalus treatment. The present work aimed to evaluate the performance of the device in an animal model of hydrocephalus. Sensor-equipped shunt tubes were placed in anesthetized, juvenile swine. The flows reported by the sensor were compared with gravimetric flow measurements. Robust correlations ($r \approx 0.87$–0.96) between the gravimetric and sensor-reported flows were obtained in 4 of the 6 experiments. The mean slope of the linear relationship of the gravimetrically determined vs. sensor flow rates was 0.98 ± 0.09 in the 6 experiments, indicating the sensor accurately reported shunt flows up to 35 ml/h. The sensor responded immediately to abrupt flow changes following cerebroventricular fluid injections. Minor hardware problems were identified and corrected. These experiments provide practical guidance for future preclinical testing.

Chapter 4: We describe an affordable and robust flow measurement technique applicable to nanoscale liquid flow rates. The approach can provide good precision (<1% RSD) in the 1.5-15 nL/min flow range. The motion of a conductive/nonconductive immiscible segmental interface in a capillary is followed by an admittance detector. The conductive marker segment is protected on both sides from the principal flow stream by individual guard segments of significantly greater impedance. The guard segments are immiscible both with the flow stream and the indicator segment. In a typical deployment, the guard segments comprise a fluorocarbon liquid that bracket a conductive segment comprising a salt solution, several mM in concentration. Perfect-piston behavior of the guard segments (no other liquid film at the wall interface) is ensured by fluorosilylation of the capillary. A common problem of interface/front tracking systems is a given interface or marker can be used only once. This is solved by incorporating the detection capillary as a loop in a 4-port valve that reverses the flow direction in the capillary before the guard/marker segments leave the loop. Several strategies are possible to interpret flow rate from the sensor output, including the most obvious, the reciprocal of the time between the leading edge and the trailing edge crossing the detection zone, or the rate of the interface movement. A change in this rate of movement can be detected in <1 s. Small temperature variations in the 25 - 35°C range do not affect sensor behavior.

Appendices B:

We trace the history of Liquid Core Waveguides (LCWs, also called Liquid Core Optical Fibers) and the role Teflon® AF (TAF) has played in their development. We show that in any shot-noise limited situation, the optimum signal to noise ratio (SNR) occurs at a path length of $\frac{1}{\alpha_a}(\ln\left(1+2\frac{\alpha_a}{\alpha_b}\right))$, approximately $\frac{2}{\alpha_b}$ under most conditions, α_a and α_b being the light attenuation coefficient due to the analyte and the background, respectively. The analysis shows that LCW length should be selected depending on the

applicable α_b value. An overly long LCW may exhibit a lower signal to noise ratio. Water-filled TAF-clad fused silica (FS) tubes show the lowest attenuation across the wavelength range. Nevertheless, except at $\lambda \geq 600$ nm, the observed α_b values far exceed those reported for pure water: it appears that both impurities in the water and waveguide losses are involved. In examining the attenuation in various water-filled tubes, we find that the transmissions of air-surrounded FS tubes are second only to TAF clad FS tubes and are better than TAF tubes or externally mirrored FS tubes. Surprisingly, except for a window centered at ~250 nm, light transmission in a water-filled PTFE tube is worse than in PEEK tubing. Light transmission in PTFE tubes improves with increasing wall thickness.

Chapter 2

BENCHTOP INLINE SHUNT FLOW MONITOR FOR HYDROCEPHALUS

2.1 Introduction

Hydrocephalus, “water in the brain”, is a central nervous system disease. The condition is caused by the accumulation of cerebrospinal fluid (CSF) in the ventricles due to excess secretion and/or disruption in circulation/reabsorption. While hydrocephalus is mostly congenital, occasionally it develops later in life, often due to brain injury. There is increasing consensus that slow-developing “normal pressure hydrocephalus” in seniors largely goes undiagnosed. Hydrocephalus incidence in the live and stillborn is ~0.1%.(3)

Hydrocephalus is incurable. If not treated promptly, fluid buildup can cause brain damage and even death. A surgically inserted “shunt”, a tube with a one-way valve, is used to drain the excess CSF into other body cavities. Since its origin, (4) many designs and modifications have been reported, especially for infants.(5, 6) Complications abound: Shunt failure rate is 40% within the first year of placement (obstruction/under-drainage, 31.4%; infection, 8.1%; over-drainage, 3.5%), and 4.5% annual failure thereafter. (7, 8) Shunt failure is almost inevitable (98%) during a patient’s lifetime. (9)

Shunt failure is not readily diagnosed. The fast reaccumulation of CSF results in emergency situations. Khan(10) reviewed the clinical recognition and emergency management of shunt malfunction and also illustrated how clinical symptoms and observations by computed tomography (CT), magnetic resonance imaging (MRI), shunt tap, Doppler ultrasonography, intracranial pressure monitoring, etc. may be clinically used to investigate and assess shunt malfunction. Still, most approaches have drawbacks. By the time shunt failure symptoms emerge or CT/MRI can detect ventricle enlargement, the brain has been exposed to abnormal pressures long enough to cause irreversible damage. Tomography exposes the newborn to unwanted radiation. Children

do not lie still for an MRI; sedation or general anesthesia is needed. Fast-sequence MRI is possible, (11) but sensitivity is low. Magnetically programmable shunt valves often need to be reset after an MRI. (12) Invasive procedures, shunt-tap or radioisotope infusion, are better diagnostic tests but present infection risks. (13)

Feasibility of reaching a definitive diagnosis has improved over the years. (14) However, procedures remain expensive and often unavailable in the developing world. They consume time at a juncture when time is exponentially critical. Hospitalization cost of pediatric hydrocephalus shunt cases already exceeded $2 billion annually in the U.S. in 2003. (15) The ability to diagnose shunt malfunction at home or in a doctor's office will greatly reduce this.

Narayanaswamy et al. (16) utilized a series of pressure sensors to provide flow information but only at flows ≥180 mL/h, higher than the maximum reported CSF flow of 116 mL/h. (17) Shunt manufacturers typically confine data to 5−50 mL/h. (18) Raj et al. (19) also used pressure transducers and were able to calibrate in the 0−25 mL/h range. Time-of-flight (TOF) flow measurement has been known since the thermal pulse TOF technique was introduced. (20) TOF flow measurement with electrolytically generated bubbles(21) requires three pairs of electrodes and adherence of bubbles to the tube wall is a known problem. Pennell et al. (22) used a commercial ultrasonic TOF flow meter in a hospital setting with the fluid draining outside. Enikov et al. (23) tested ferromagnetic cantilevers for magnetoresistive sensing but drift/noise was too high. Bork et al. (24) reported ±10% accuracy in vitro with thermal anemometry over a 2−40 mL/h flow rate range. Clark et al. (25) deployed an array (to be fair, a single one could have been used) of piezoresistive pressure sensors to measure flow in the 2−35 mL/h range; measurement outside this range did not appear possible. Importantly, the cross-section of the conduit used for flow sensor testing is not always specified. (23) Using a smaller

diameter conduit for the sensor facilitates measurement of the all-important low flow rates, but in reality such conduits will be more prone to blockage. Actual shunt inner diameters are often 1.5 mm (cross-section 1.77 mm^2, http://implantesclp.com/uploads/pdf/Codman.pdf, http://www.medtronic.com/us-en/patients/treatments-therapies/hydrocephalus-shunt/lpshunts.html). All sensors above have been tested with conduit cross-sections that are much smaller: 0.50,(20) 0.78,(17, 22) and 0.81(25) mm^2, except when the sensor dimensions dictated a larger cross-section,(24) 8 mm^2.

Presently, the only FDA-approved device for checking shunt flow is the ShuntCheck (http://neurodx.com/shuntcheck/index.asp). An ice cube is placed on the skin over the shunt, and a thermosensor array patch is placed on the skin over the shunt a bit lower. Arrival of a lower temperature slug indicates the presence of shunt flow. However, CSF flow is intermittent. ShuntCheck does not statistically predict shunt failure; the measurement time can also be long. (26, 27)

TOF flow meters obligatorily use two transducers as a transmitter-receiver pair but do not necessarily utilize bidirectional abilities of such transducers, nor do they take advantage of essentially constant composition of CSF or the narrow range of physiological temperature. Thermal anemometry does but the obligatory continuous operation is power intensive. Presently we use a single common thermistor, applying a momentary heating pulse and then monitoring the flow-dependent rate of cooling.

2.2 Experimental section

2.2.1 Materials and instrumentation

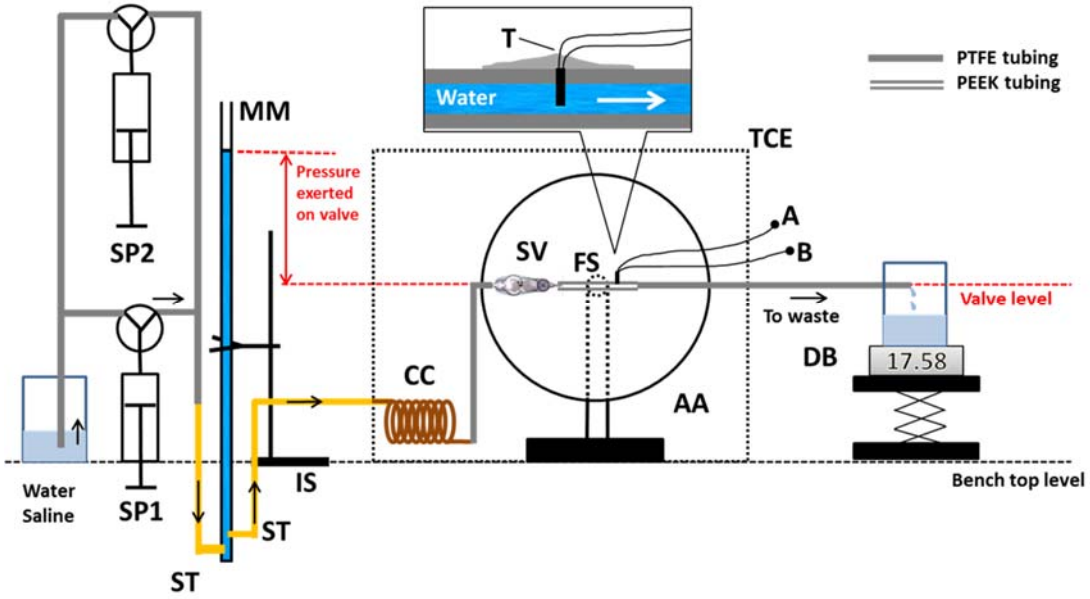

Figure 2- 1 SP1/2, syringe pump; MM, manometer; ST, Santoprene tube; IS, iron stand; T, thermistor; TCE, temperature-controlled enclosure; CC, copper coil; SV, shunt valve; FS, flow sensor; AA, adjustable angle platform; A/B, thermistor lead wires; DB, digital balance. The difference between the liquid level in MM and valve level and the cracking pressure of SV determined the flow rate. The waste outlet is always at the same level as SV. In flow rate calibration and programmed stepwise flow rate experiments, MM, SV, and AA were not present.

The experimental arrangement is shown in Figure 2-1. Milli-Q water or normal saline exhibited the same thermal properties and was used interchangeably. Either fluid was continuously delivered by two syringe pumps SP1 and SP2 (V6, P/N 24520, www.kloehn.com) in hand-shake mode. Syringes of 1 mL capacity were used for flow rate calibration with a resolution of 0.075 mL/h; for continuous or staircase flow testing, 5 mL syringes were used with a flow resolution of 0.375 mL/h. The manometer MM was made from a bottom-sealed graduated acrylic tube (90 cm × 1.9 cm diameter). Flexible Santoprene tubes ST were attached to the bottom of the manometer by hot-melt

adhesive for liquid I/O. The flow coming through ST entered a temperature-controlled enclosure TCE (chromatography oven LC30, www.dionex.com, temperature stability 0.1 °C), first going through a coiled copper tube CC for thermal equilibration and then through a shunt valve SV (adjustable pressure valve with hydrophilic surface modification, Strata II 42866, www.medtronic.com) and then through the flow sensor FS, which is mounted on an adjustable angle platform AA (to simulate different inclinations of the head). The sensor output is collected in a waste container placed on a digital balance DB which is continuously monitored. The flow sensor FS comprises of a small length (3.2 cm) of a flow-through PEEK tube (1.6/3.2 mm i.d./o.d., 1.99 mm^2 cross-section) with a 0.5 mm diameter hole drilled through the wall. A thermistor (0.45 mm diameter × 2 mm, R_{37}°C = 15.32 kΩ, temperature coefficient −0.85%/°C, SEMITEC; 223Fμ5183-15U004, www.mouser.com, see Figure 2-2) was inserted through the hole, its tip exposed to the flow stream, with only enough of the tail outside the tube wall to be immobilized by hot-melt adhesive.

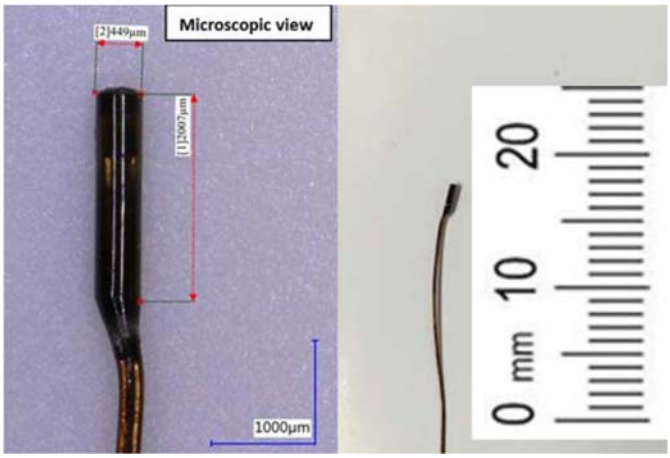

Figure 2- 2 Thermistor tip under a microscope and next to a scale.

2.2.2 Schematic and operational sequence

A Programmable System on a Chip (PSoC) (Cypress Semiconductor PSoC5LP as contained in a FreeSoC2 board, www.sparkfun.com) was addressed by the PSoC Creator graphical interface controlled the system. A LabVIEW (www.ni.com) program controlled the FreeSoC2; the LabVIEW and PSoC programs are provided in the Appendix A. The functional schematic is shown in Figure 2-3; The thermistor is part of a bridge circuit, with two 20 kΩ fixed resistors and one 20 kΩ adjustable resistor to balance the bridge. The circuit either (a) senses the temperature or (b) heats the thermistor. Automated operation sequentially goes through (1) sensing mode for 5 s (initial temperature measured); (2) heating mode for 5 s (a voltage pulse applied to the thermistor); and (3) a longer duration (20 s) sensing mode (maximum temperature of the thermistor, immediately after the heat pulse is turned off, measured and recorded). In Figure 2-3, the black lines are always connected; the blue and red traces exclusively operate in the sensing and heating modes, respectively. During either sensing step, 1.5 V is applied to the bridge and the output is amplified 10× by an instrumentation amplifier (AD623ANZ, www.analog.com) and sampled at 1 kHz by the 18-bit ADC of the FreeSoC2 with a span of 2048 mV. In the heating mode, a TTL signal from the FreeSoC2 triggers an N-channel logic level MOSFET (IRF630) to turn on a set of microminiature relays that simultaneously disconnect the bridge power and connect the thermistor to a 8.2 V supply for 5 s (measured, 5.0001 ± 0.0004 s). The sensing-heating-sensing cycle repeats automatically, generating a set of measurements every 30 s.

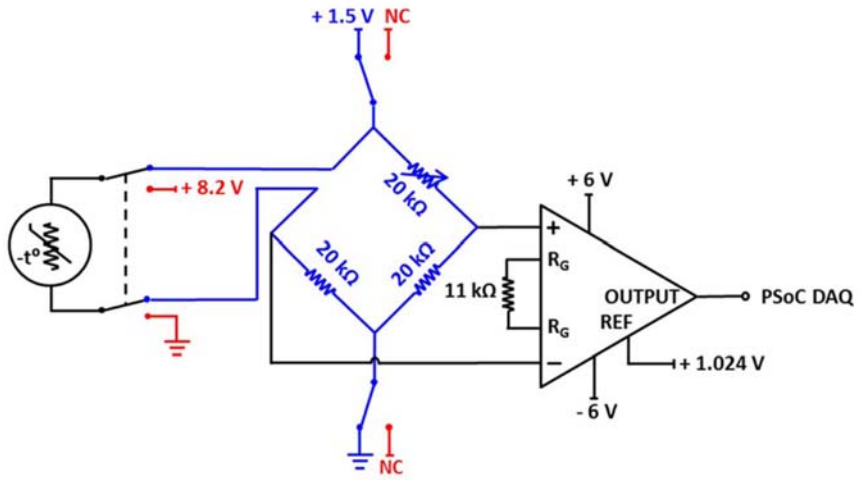

Figure 2- 3 System has two operational modes. Black lines are always connected and functional. In the sensing mode, the blue traces are operative. In the heating mode, the thermistor is connected to the 8.2 V heating voltage (red).

2.3 Results and discussion

2.3.1 Choice of sensing strategy

The prime requirement of a shunt flow monitor is to provide a flow or no-flow decision. The second is to provide an approximate measure of the flow rate if there is flow. The flow transducer needs to be small; for simple circuits, all other components, including a wireless transmitter, are readily integrated as in numerous present implanted devices. Time needed and power dissipation per measurement are also important, but advances in wireless recharging of implanted batteries(28) and inductive charging (particularly convenient for a CSF shunt, deliberately placed close to the outer body surface for valve setting manipulations)(29, 30) have made the latter less critical.

The present application operates over a very limited range of temperature (virtually constant during a short measurement period) and essentially constant fluid thermal properties. We use a single common small thermistor intended for medical

catheter applications, bidirectionally. The device utilizes an ultrathin sensing film on an alumina substrate encapsulated by a thin glass layer with a response time of 70 ms. (31)

2.3.2 Choice of experimental temperature range and temperature effects.

The core temperature of a healthy individual ranges from 36.2−37.5 °C. (32) However, the majority of a hydrocephalus shunt is close to the surface and is highly subject to environmental influence. Exposed to 15 °C for 2−3 h, the subcutaneous temperature can drop to 32 °C. (33) At the high end, fevers rarely exceed 39 °C, thanks to antipyretic medication. The experiments therefore encompassed a span of 32−39 °C with 1 °C steps.

The temperature dependence of the thermal conductivity of CSF has not been specifically measured; that for water changes by around 2.4% within 30−40 °C. Although the specific heat of water is constant in this interval, changes in the thermal conductivity necessitate some form of temperature correction. The challenge is to do so without the need for a reference thermistor.

2.3.3 Data collection and interpretation.

The three-step measurement cycle is 30 s in duration, resulting in 30 000 data points. Of these, the 109 data points from t = 4.891 to 4.998 s are averaged and recorded as the initial voltage V_i. Over the experimental range, V_i was linearly related to the temperature, T (see also Figure 2-4):

$$V_i = -(9.152 \pm 0.076) \times 10^{-2} \times T + (4.411 \pm 0.027), r^2 = 0.9996 \quad (1)$$

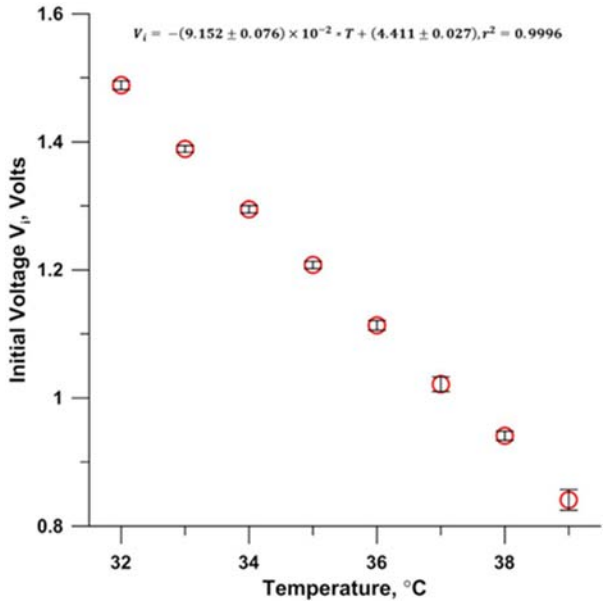

Figure 2- 4 The initial signal has a linear relationship with the surrounding temperature.

The manufacturer provides operational data for the valve used for 5−50 mL/h. We provide for quantitation between 3 and 52.5 mL/h based on the signal measured immediately after the heat pulse ceases. The post pulse maximum temperature was taken to be the lowest voltage signal (V_f, the bridge output decreases with increasing temperature) measured during the first 10 ms after the heating step. This was invariably the third or fourth point measured following the cessation of the current pulse (3 or 4 ms after). The net change in the signal, $V_i - V_f$, ΔV, corresponds approximately to 2 °C (Figure 2-5) with the exact value depending on the flow rate and the surrounding temperature (Figure 2-6) for reasons below.

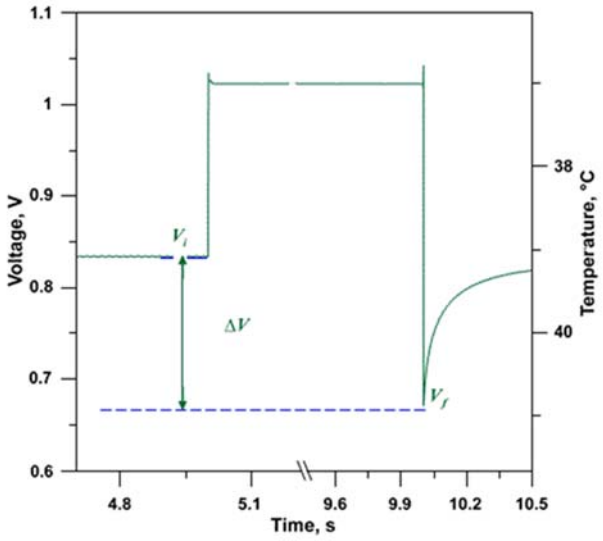

Figure 2- 5 Anatomy of a single measurement cycle conducted at a temperature of 39 °C. Data is collected continuously at 1 kHz. The signal between 4.891 – 4.998 s is stored and averaged as the initial voltage V_i. Note the break in the abscissa. The lowest temperature measured after the cessation of the heat pulse and reestablishment of the bridge is taken as the final voltage V_f and the difference $\Delta V (=V_i - V_f)$ is related to the flow rate F. Data collection continues to 30 s to ensure a return to the initial temperature. See Figure 2-6 for an overlay of the same experiment done at multiple temperatures.

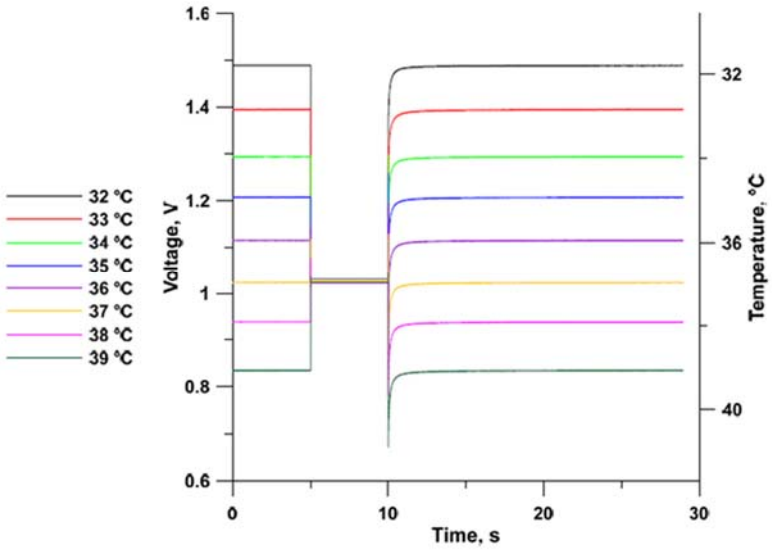

Figure 2- 6 Multiple temperature overlay of the same experiment described in Figure 2-5.

First, the flowing fluid cools the thermistor during the time the current flows and thereafter. Obviously faster flow leads to greater cooling. Figure 2-7 shows the post-heating cooling curve as a function of flow rate after a short (120 ms) voltage pulse.

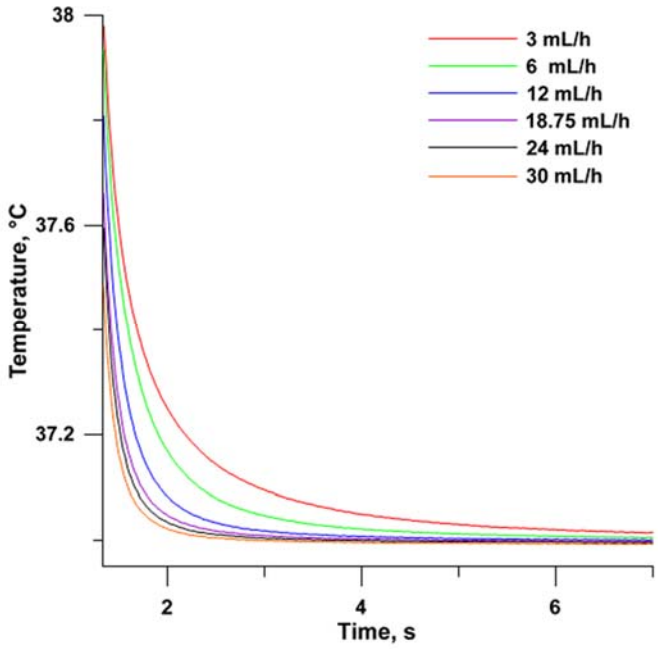

Figure 2- 7 Early experiments with a different protocol. Time zero begins with sensing mode (1 s) to determine the initial temperature. This is followed by an auto-zero operation (instantaneous), a voltage pulse of 120 ms duration, and sensing mode of 18.880 s duration to complete a 20 s measurement cycle. The abscissa presented begins at 1.33 s. The exponential decay curve ($y = a - e^{-bt}$) is fit for the data from t = 1.42 - 6.40 s. The relationship with the exponential decay constant b and the flow rate is shown in Figure 2-8.

The signal follows an exponential decay function of the form y = a − exp(−bt). We initially explored the relationship of the exponential parameter b with flow rate F (F = p exp(bq)), where p and q are constants) (Figure 2-8) to measure the flow rate. However, as may be obvious from Figure 2-7, the resolution (and hence accuracy) is poor at higher flow rates.

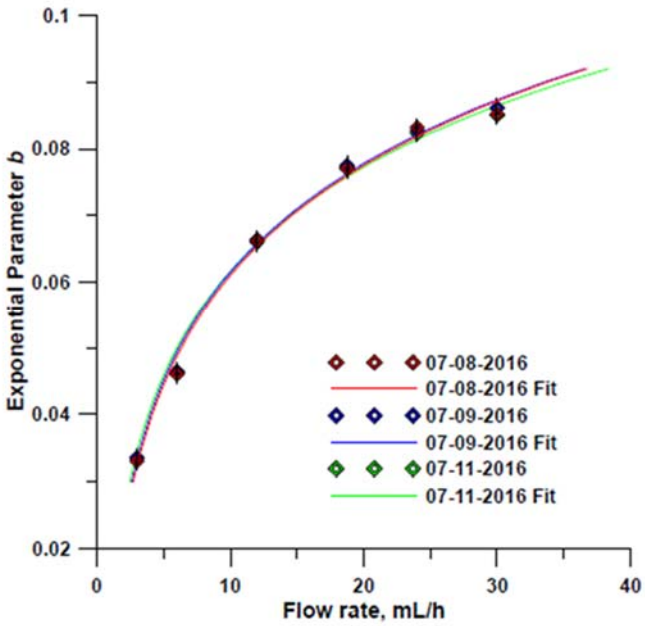

Figure 2- 8 The exponential decay constant *b* (Figure 2-7) is related to the flow rate *F as* $F = pe^{bq}$ as indicated.

Compared to the application of a short pulse while monitoring the cooling profile, thermal anemometry measures the steady-state temperature with constant heating. It provides good resolution at high flow rates at the expense of power consumption. We settled on a compromise: a longer duration pulse (5 s). The highest temperature difference (expressed in terms of ΔV) resulting from the pulse provided good resolution and accuracy from 3−52.5 mL/h. The relevant calibration plots of ΔV as a function of the flow at eight different temperatures are shown in (Figure 2-9a). At each temperature the relationship:

$$F = m\Delta V^n \tag{2}$$

shows excellent agreement. It is more convenient to use the linearized form of eq 2:

$$\log F = \log m + n\ log\Delta V \tag{3}$$

A plot of log ΔV vs log F in all eight cases exhibit a linear coefficient of determination (r^2) in the range of 0.9955−0.9986, see (Figure 2-9b) and Table S1.

Second, at any flow rate, the temperature rise is always higher for higher ambient temperature (Figure 2-9b). This arises from constant voltage heat pulse application: more current flows and more power is dissipated as the device resistance is lower at a higher temperature with only a minor ameliorating effect of the slightly greater fluid thermal conductivity at a higher temperature. With a constant current pulse, temperature rise would have been less at a higher temperature. A constant power pulse is not difficult to implement;(34) this would lead to a temperature-independent calibration curve. However, an acceptable level of error can be attained with the present arrangement as shown below.

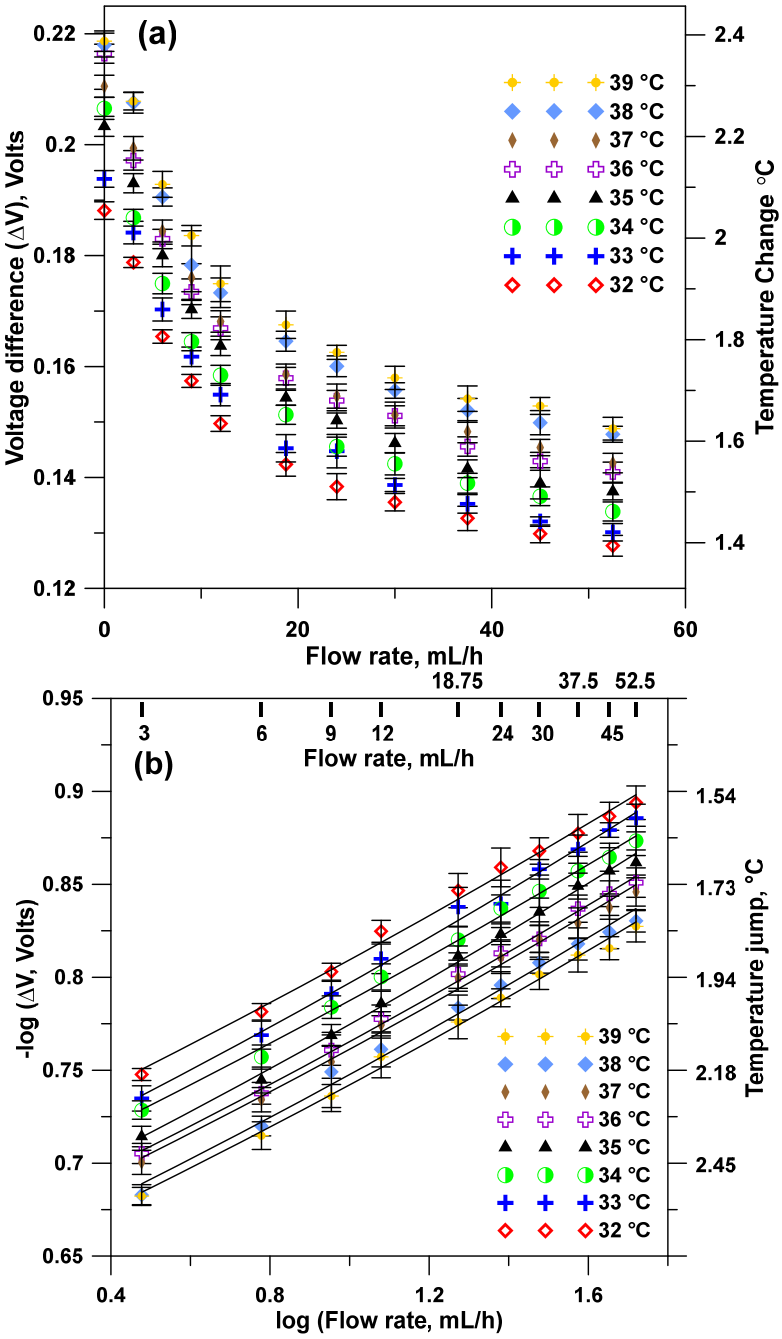

Figure 2- 9 (a) Voltage difference ΔV (the difference between bridge voltage immediately before and immediately after application of the voltage pulse as a function of flow rate F and its dependence on the ambient temperature. (b) log ΔV vs log F has a highly linear relationship, see Table 2-1 for numerical details.

Table 2- 1 Best fit parameters for eq. 3

Temp °C	- *log m* (eq.3)	- *n* (eq. 3)	r^2	%RMSRE
32.0	5.79 ± 0.14	8.38 ± 0.17	0.9967	5.17
33.0	5.47 ± 0.14	8.11 ± 0.17	0.9964	5.39
34.0	5.62 ± 0.12	8.40 ± 0.15	0.9975	4.34
35.0	5.29 ± 0.10	8.10 ± 0.13	0.9980	3.90
36.0	5.42 ± 0.09	8.38 ± 0.11	0.9986	3.35
37.0	5.42 ± 0.13	8.42 ± 0.17	0.9969	5.00
38.0	5.26 ± 0.15	8.36 ± 0.20	0.9955	5.96
39.0	5.33 ± 0.12	8.51 ± 0.16	0.9972	4.68

2.3.4 Temperature-independent interpretation of signal to provide flow rate.

The excellent linearity of the plots in Figure 2-9 (b) indicates that at any given temperature the relationship described in eq 2 or 3 can be used to compute the flow rate. The data in Table 2-1 indicates that at any particular temperature the root-mean-square relative error (RMSRE) is modest (3.4−6.0%; mean ± sd, 4.72 ± 0.84%). As the temperature is given by V_i, a lookup table can store applicable values of m and n in eq 3 corresponding to different V_i values. However, a single relationship is esthetically desirable. While single best fit values of log m and n (−5.445 and −8.179, respectively) led to a relatively large error (39.4% RMSRE), rendering the exponential term into a V_i-dependent function reduced the error drastically (<6.3% RMSRE):

$$F = 3.75 \times 10^{-6} \times \Delta V^{(-9.568+1.088V_i)}, \%RMSRE = 6.28 \quad (4)$$

The entire data set (eight temperatures, ten flow rates) is shown in Figure 2-10 as actual vs predicted (eq 4) flow rates.

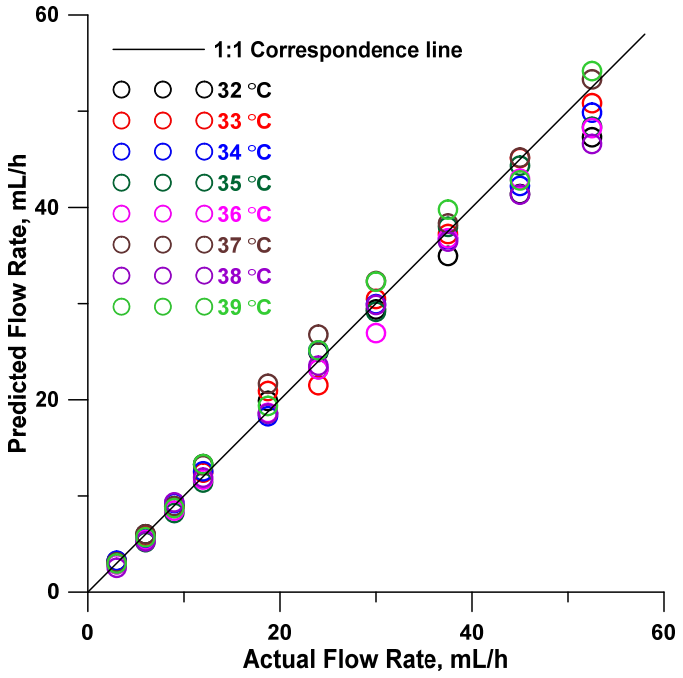

Figure 2- 10 Regardless of the temperature, a single equation $F = 3.75 \times 10^{-6} \times \Delta V^{(-9.568+1.088Vi)}$ provides a good prediction for the flow rate, with 6.3% RMS relative error.

2.3.5 No-flow confirmation

Beyond the accuracy of flow rate measurement, it is particularly important to ascertain that no flow is occurring. In each measurement cycle, data are recorded for around 20 s past the cessation of the heat pulse. Under most flow conditions, this is enough time for the temperature to return to the initial preheating value. However, as the flow rate decreases and especially when there is no flow, the cooling is not complete. Consider the difference between the initial signal V_i and the end of the cycle signal V_{end} (last 50 data points averaged). There is an obvious marker of no flow: $V_i - V_{end}$ has a positive value statistically different from zero and always higher than those with flow present. In addition, $|V_i - V_{end}|$ decreases from the first measurement to subsequent ones much more for no-flow condition, as V_i fails to return to the initial starting point. Figure 2-11 shows that this makes it facile to demarcate and confirm a no-flow condition.

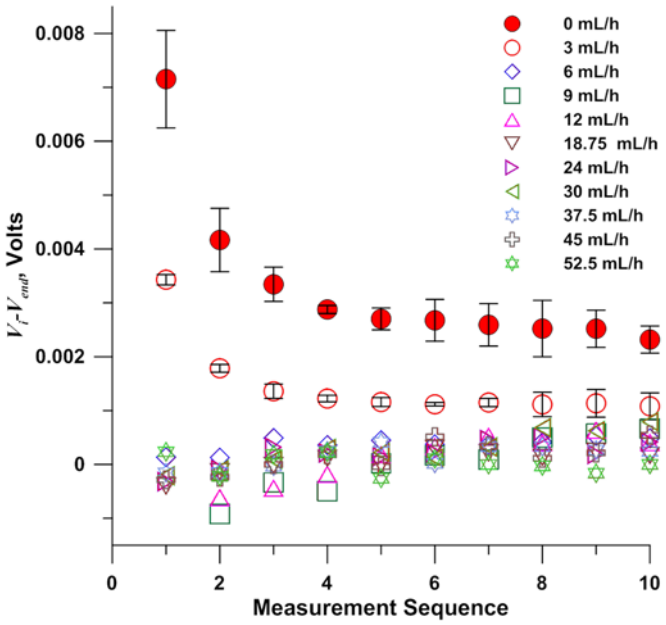

Figure 2- 11 Difference between no flow (0 mL/h) and all other conditions is that under no-flow conditions, the difference between the bridge voltage at the beginning (V_i) and at the end of a measurement cycle (V_{end}) is the highest and statistically well above all others, including 3 mL/h, the lowest nonzero flow studied. The $V_i - V_{end}$ values for F > 3 mL/h are essentially indistinguishable from each other and as a function of the measurement sequence. The standard deviation of the measurements are shown for F = 0 and 3 mL/h flow rates based on repeat measurements (n = 3) of the entire sequence. The standard deviation is by far the highest for the stagnant conditions as is the drop between the first and the second measurement. Standard deviations, not shown for F > 3 mL/h, are comparable to those at 3 mL/h. As an index, for a conduit of 1.59 mm i.d., the flow velocity is 420 μm/s at 3 mL/h.

2.3.6 Stepped flow testing at constant and stepped temperature

The ability of the sensor to perform under different temperature and flow conditions were tested first at a constant temperature of 37 °C and a stepped non-monotonic flow sequence of 15.00, 3.70, 22.50, 28.125, 10.33, 5.26, 33.75, 41.25, 48.75, and 6.66 mL/h with 6 min flow steps. Gravimetric measurements agreed within ±2% of the nominally programmed flow rate. The same flow-step experiment was then repeated with a simultaneous stepwise increase of temperature from 32 to 38 °C. Figure 2-12 (a),(b) indicate good sensor performance.

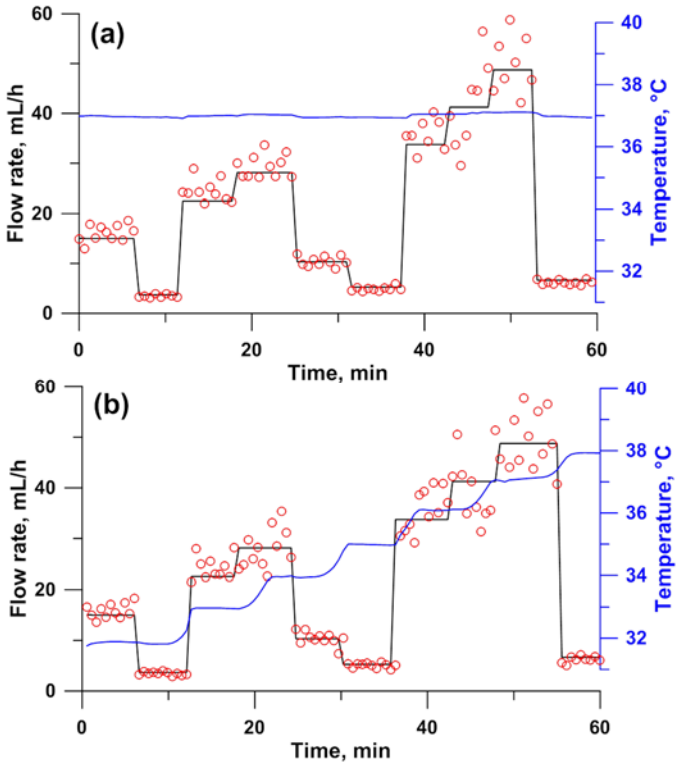

Figure 2- 12 Flow tests in 6 min steps with non-monotonic flow changes (a) at 37 °C and (b) as temperature is increased from 32 to 38 °C. The nominal flow rates are indicated by the black traces whereas the red circles indicate the values reported by the sensor every 30 s. The blue trace indicates the temperature as measured by the sensor.

2.3.7 24-h continuous testing with variable angular placement with simulated accumulation and release

CSF drainage through a shunt is not continuous. Fluid accumulates in the cranial cavity with little or no drainage until the set pressure is reached. At this point, the valve opens and drainage occurs until the pressure drops. The pressure at which the valve opens fully can be adjusted and may also depend on the gravitational orientation of the patient (and hence the valve). In this experiment, the valve was preset to a performance setting of 2.5 (highest of its adjustable range). As indicated in Figure 2-1, simulated CSF is pumped into the manometer system that connects to the valve and the flow sensor

mounted in a rotatable platform (permits the vertical orientation to be changed). Beginning with an upright standing position (90°), as indicated in Figure 2-13, the orientation was changed every 8 h to reclining (45°) and supine (0°) positions, and the level of the waste outlet was also simultaneously changed. The thermostated enclosure doors needed to be opened for access during this change; this shows up as a transient in the temperature record. Gravimetry and the present sensor provided respective measurements every 60 and 30 s. Parts (a) and (b) of Figure 2-13, respectively, show results for one experiment in which the temperature was unchanged and another where the temperature was stepped from 32 to 39 °C. The results indicate good agreement between the sensor results and gravimetry. Although our simulated CSF generation rate was constant (fluid pumped into the manometer at a constant rate), the zero flow periods varied, resulting in different pressures at which the valve actually opened. Naturally, the longer the zero flow periods, the greater was the accumulated pressure (maximum observed was 30 cm H_2O; the majority of the time the pressure was maintained in the 13−14 cm range) and greater was the initial flow rate when the valve opened. While the manufacturer data is limited to <50 mL/h, both gravimetry and sensor measurements (especially in the constant temperature trial) indicated post-opening transient flow rates much higher than 50 mL/h. Even though these “surge” flow rates were considerably beyond those underlying eq 4, the use of eq 4 nevertheless provided good agreement with the gravimetrically measured rates.

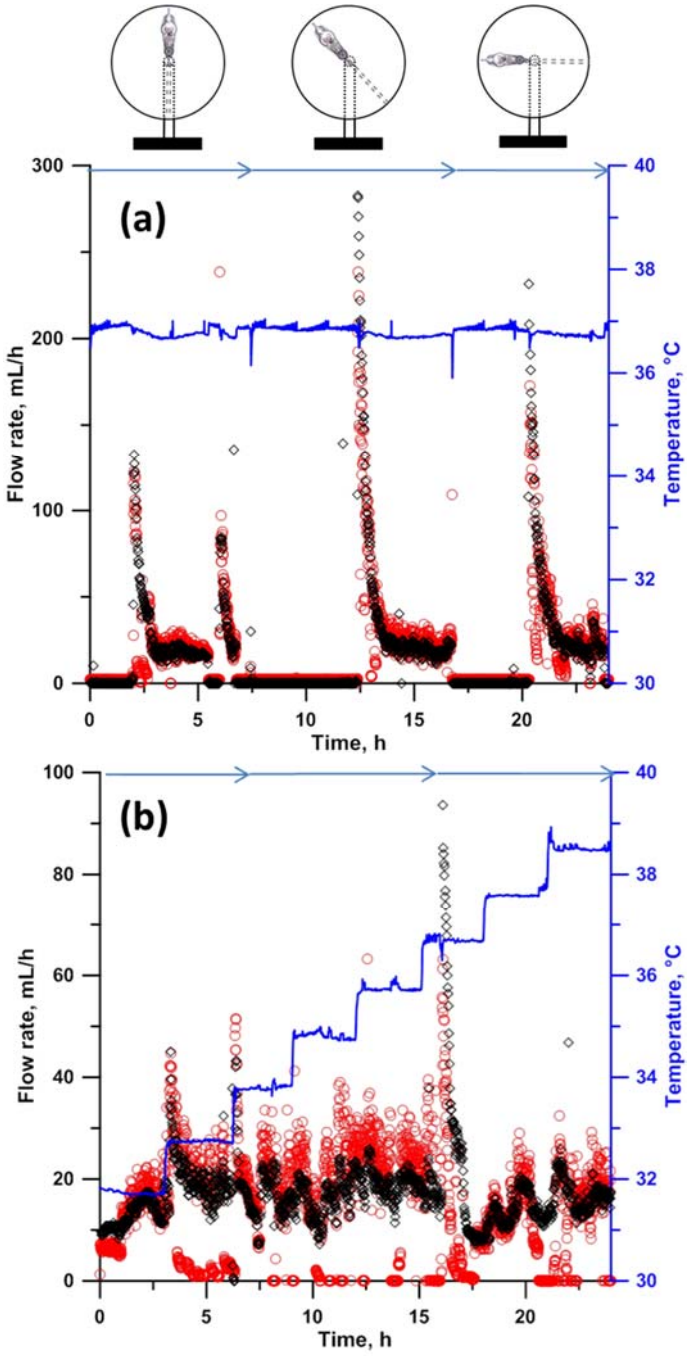

Figure 2- 13 24 h tests (a) at 37 °C and (b) gradient ambient temperature from 32 to 39 °C. Good agreement was observed between measurements by the present sensor (red circle) and gravimetric flow measurements (black diamond). Blue trace indicates the ambient temperature as measured by the thermistor.

2.4 Conclusions

We have demonstrated the feasibility of a hydrocephalus shunt flow sensor using a single thermistor as a bidirectional transducer. It cannot only measure CSF flow in the expected flow rate range (<50 mL/h) but also surge flow rates of ≥200 mL/h. Temperature variation within the expected range is compensated for. Measurements can be made every 30 s, greatly reducing the waiting period and potentially simplifying clinical investigations. The sensor provides additional confirmation that there is no flow, providing critical actionable information. All experiments, thus far, however, were in vitro. Dual thermistor based cardiac output monitors were introduced around 50 years ago(35) and continue to be used to date even with infants. (36) It seems reasonable to be optimized that the present sensor can be provided with a biocompatible coating and deployed in practice. We will report on animal experiments in the near future.

Chapter 3

INLINE FLOW SENSOR FOR VENTRICULOPERITONEAL SHUNTS: EXPERIMENTAL EVALUATION IN SWINE

3.1 Introduction

An inline sensor for monitoring ventriculoperitoneal shunting of cerebrospinal fluid for hydrocephalus treatment is reported in chapter 2. To evaluate the sensor's performance in vivo, studies were conducted after placement of sensor-equipped shunts in 8 anesthetized, juvenile swine.

The inline flow sensor was inserted in a ventriculoperitoneal shunt which was installed in the third cerebral ventricle and routed externally to the abdominal cavity. The flow sensor continuously reported shunt flow in 30 s intervals throughout the experiment. Concurrently, shunt flow was diverted from the abdomen and collected in pre-weighed vials at 1 or 5 min intervals for gravimetric flow measurements. At designated times, 5-20 ml boluses of artificial cerebrospinal fluid were injected into the third ventricle. The flow rates reported by the two methods were analyzed and compared.

Six of the eight experiments were successfully conducted, in which more than 4300 acceptable flow measurements were obtained by the sensor. The sensor responded immediately to abrupt flow changes following ventricular fluid injections. Robust correlations ($r = 0.87$-0.96) between the gravimetric and sensor-reported flows were obtained in 4 of the 6 successful experiments. The mean slope of the linear relationship of the gravimetrically determined vs. sensor flow rates was 0.98 ± 0.09 in these six experiments, indicating the sensor accurately reported shunt flows up to 35 ml/min.

The results indicate successful testing of the device in an acute in vivo large animal preparation. The sensor is sensitive and accurate in reporting shunt flows over a

wide range. Water can serve as a universal calibration medium for flow measurements of more complex fluids. Mild hardware problems were identified and corrected. These experiments provide practical guidance for future preclinical testing of the device.

3.2 Methods

3.2.1 Inline shunt flow monitor for swine testing

The principle of the thermistor-based shunt flow monitor evaluated in this study was presented in chapter 2. In brief, a single micro thermistor (0.5 x 2 mm; R30 °C = 17.48 kΩ, temperature coefficient = −0.85%/°C; SEMITEC 223Fμ5183-15U004, www.mouser.com) was used alternately as a heater and as a temperature sensor. In the sensing mode, the thermistor is part of a Wheatstone bridge that measures resistance; the bridge output voltage is directly related to the temperature. Next the thermistor is disconnected from the bridge and a short duration (5 s) voltage pulse is applied to heat the adjacent fluid by ~2°C, and then the circuit reverts to temperature measurement. At 30°C the sensing and heating currents through the thermistor are 80 and 560 μA, respectively. The rate of shunt flow past the thermistor is derived from the rate of shunt fluid cooling. The temperature difference of the thermistor before and after the heat pulse (corresponding to the difference in the bridge output voltage, ΔV, immediately before and after the pulse) is sufficient to determine the flow (F). At a given F, the temperature difference also is affected by the initial temperature of the thermistor, which is revealed by the initial bridge voltage (V_i).

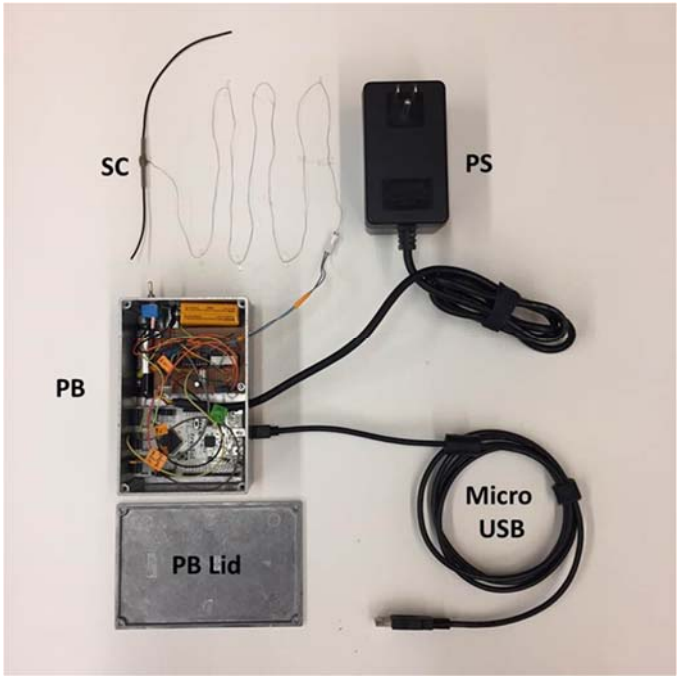

Figure 3- 1 Sensor instrumentation. SC, sensor cell: thermistor is inserted in a PEEK tube and secured with hot adhesive. Two PTFE tubes connect to the silicone shunt. PB, project box with circuit board and microcontroller inside; PB Lid, project box lid; PS, power supply for the circuit board. The micro USB cable is used for instrumental control and interfaces with a computer for data acquisition.

The sensor configuration is shown in Figure 3-1. Minor modifications were made to the original design to improve compactness and portability. The sensor cell was pre-calibrated to detect flows between 0-52.5 mL/h at 32-39°C (experiment 1), 26-34°C (experiments 2-7) or 28-32°C (experiments 8). This flow range fully encompasses CSF flow rate ranges reported in hydrocephalus patients (18, 37). Three thermistors of the same design were used during the present experiments: Experiments 1-4 were conducted with the first thermistor, experiments 5-7 with the second, and experiment 8 with the third.

Each sensor was individually calibrated in-vitro and the calibration pertaining to that particular device was applied during the experiment to derive flow values from the thermistor readout. The calibration equations for the three sensors were as follows (Figures 3-2, 3-3, 3-4):

$$Sensor\ 1: F = 8.138\ \times 10^{-5} \times \Delta V^{(-8.840+0.895\times V_i)}$$

$$Sensor\ 2: F = 9.713\ \times 10^{-4} \times \Delta V^{(-10.266+1.438\times V_i)}$$

$$Sensor\ 3: F = 1.923\ \times 10^{-3} \times \Delta V^{(-9.057+1.112\times V_i)}$$

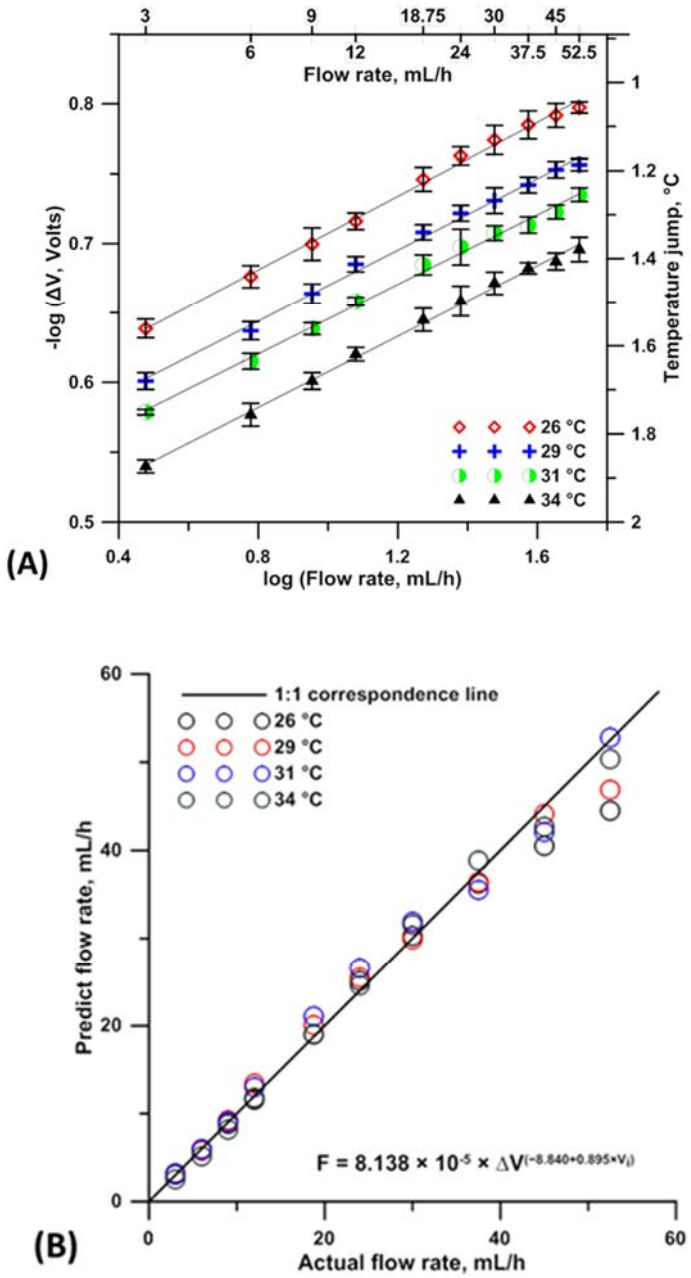

Figure 3- 2 Sensor 1 was calibrated as previously described. Similar sensor behaviors were observed between 0 – 52.5 mL/h at 26 – 34 ˚C. (A) log ΔV vs log F has a highly linear relationship. (B) The equation $\mathrm{F} = 8.138 \times 10^{-5} \times \Delta \mathrm{V}^{(-8.840+0.895\times \mathrm{V_i})}$ provides a good prediction for the flow rate, with 6.9% RMS relative error.

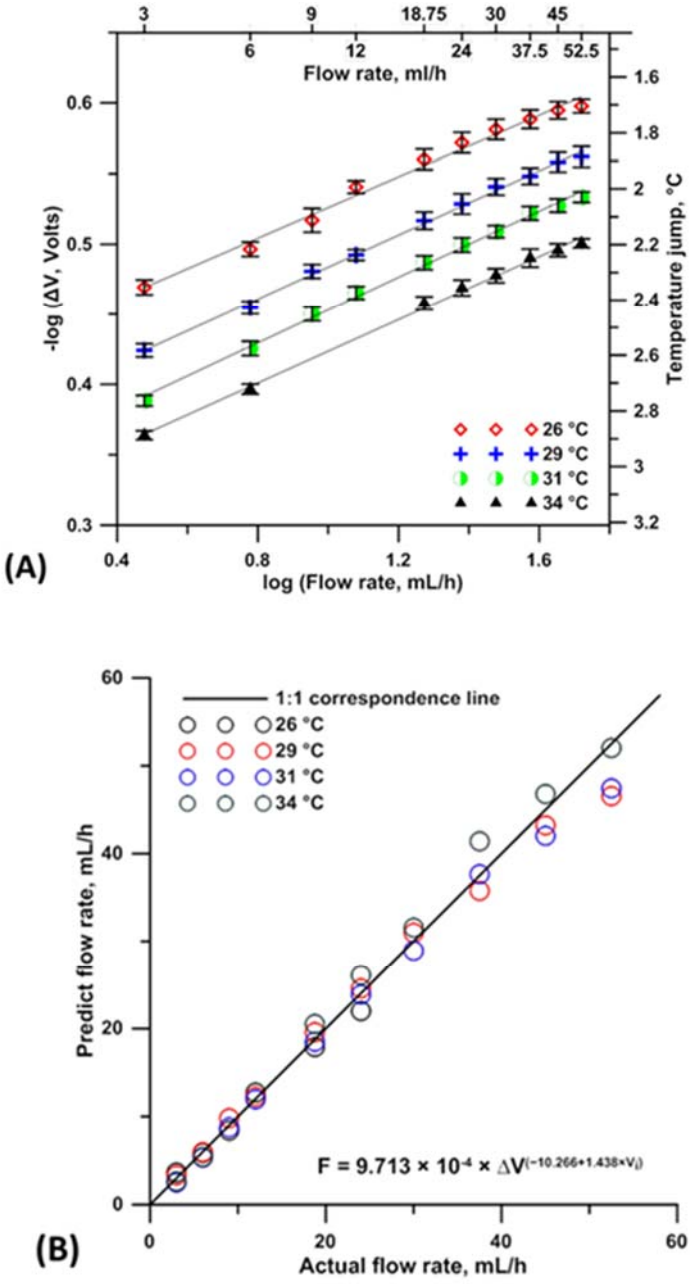

Figure 3- 3 Sensor 2 was calibrated as previously described. Similar sensor behaviors were observed between 0 – 52.5 mL/h at 26 – 34 ˚C. (A) log ΔV vs log F has a highly linear relationship. (B) The equation $\mathrm{F} = 9.713 \times 10^{-4} \times \Delta \mathrm{V}^{(-10.266+1.438\times \mathrm{V_i})}$ provides a good prediction for the flow rate, with 7.9% RMS relative error.

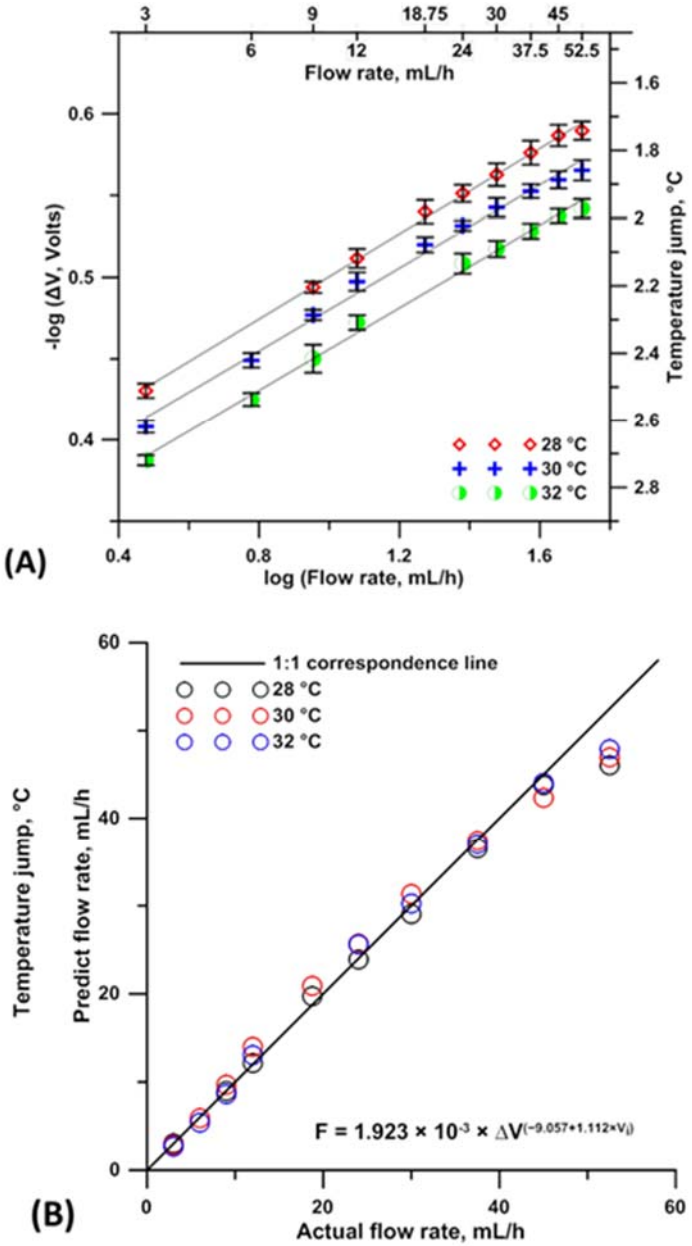

Figure 3- 4 Sensor 3 was calibrated as previously described. Similar sensor behaviors were observed between 0 – 52.5 mL/h at 28 – 32 ˚C. (A) log ΔV vs log F has a highly linear relationship. (B) The equation $\mathrm{F} = 1.923 \times 10^{-3} \times \Delta \mathrm{V}^{(-9.057+1.112\times \mathrm{V_i})}$ provides a good prediction for the flow rate, with 7.0% RMS relative error.

In the original in vitro experiments as discussed in chapter 2, the amplitude of the voltage pulse applied for heating was 8.2 V. The present experiments were conducted with a 9.6 V pulse, with the expectation that increasing the voltage amplitude would increase the temperature difference and thereby improve flow resolution. Based on first principles, the temperature rise is proportional to the square of the applied voltage; on average the temperature rise in the present experiments would be expected to be around 30% higher than in the previous in vitro experiments.

3.2.2 Animals and surgical procedures

Animal experimentation was approved by the Institutional Animal Care and Use Committee of the University of North Texas Health Science Center (protocol # IACUC-2017-0029) and was conducted in accordance with the Guide to the Care and Use of Laboratory Animals (U.S. National Research Council publication 85-23, revised 2011). Experiments were conducted in 8 juvenile Yorkshire swine (4 males) weighing 34-42 kg. After an overnight fast, the pigs were premedicated with telazol (6.7 mg/kg im) and xylazine (1.3 mg/kg im), intubated, and maintained under a surgical plane of anesthesia by mechanical ventilation (12-14 cycles/min; tidal volume 15 ml/kg) with 1-3% isoflurane in 100% O_2.

Animal preparation is shown in Figure 3-5. Pigs were placed on a heated pad in the left lateral recumbent position, and body temperature was monitored via a rectal probe. Epidermal electrode patches were applied to the limbs to capture the standard lead II electrocardiogram. The mid-sagittal frontoparietal region of the scalp was incised to expose the cranium. A 5 mm diameter burr hole was drilled approximately 5 mm to the right of the sagittal suture and 1 cm rostral to the frontal-parietal suture, and a vinyl catheter was inserted and advanced into the third cerebral ventricle. Catheter positioning in the third ventricle was verified by the spontaneous flow of straw-colored fluid into the

catheter. After application of bone wax to seal the hole, the catheter was connected to a tubing to effect a ventriculoperitoneal shunt, via two 3-way stopcocks placed in series approximately 5-10 cm distal to the burr hole: one connected to a pressure transducer for monitoring cerebroventricular pressure, and the other for bolus injections of the artificial CSF described below. The distal end of the external shunt was inserted into the abdominal cavity for drainage.

An aqueous solution containing physiological concentrations of the major CSF electrolytes (141 mM Na^+, 120 mM Cl^-, 2.9 mM K^+ and 22 mM HCO^{3-}) (38) was freshly prepared and maintained in a 37°C water bath. This fluid was injected (5, 10, 15 or 20 ml bolus) into the cerebral ventricle via the cerebroventricular catheter.

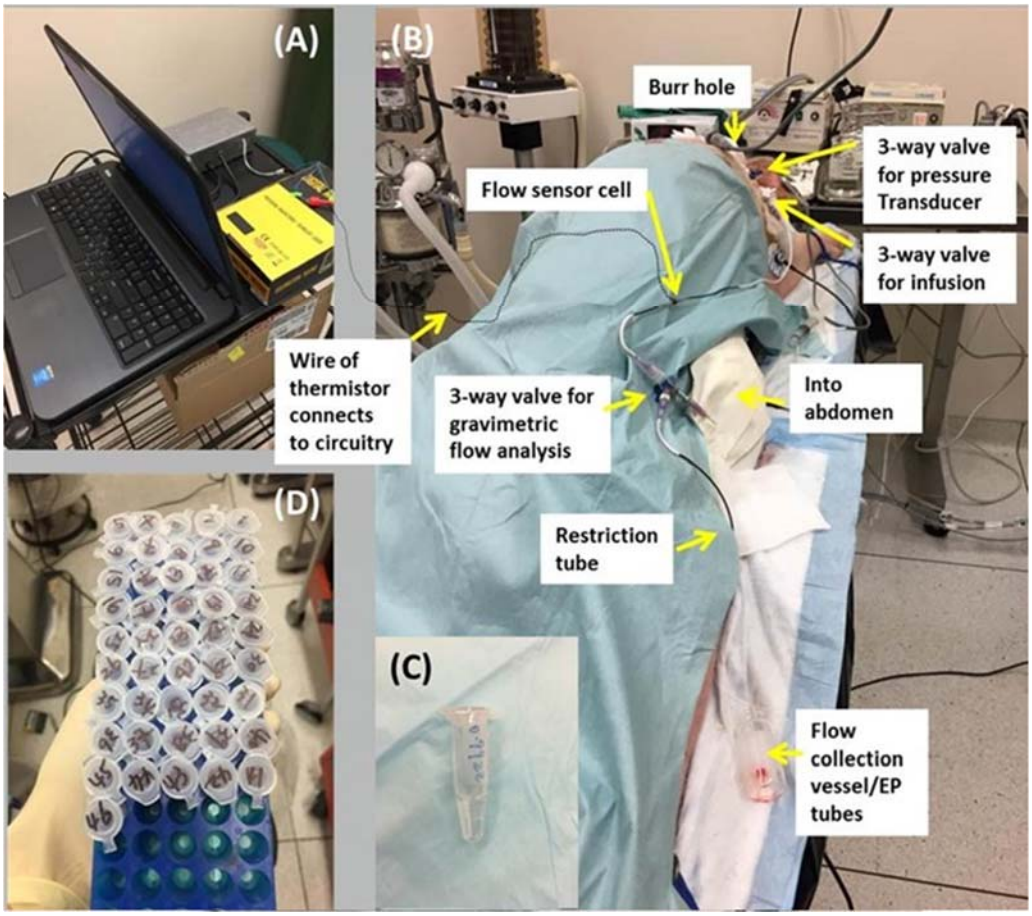

Figure 3- 5 Experimental setup for studies in anesthetized swine. (A) Shunt flow monitor and computer are located on a portable table on the left side of the operating table. (B) Top-rear view of the pig and flow system on the operating table. (C) A pre-weighed vial containing 5 min collection of CSF for gravimetric flow measurements is shown. (D) Vials are collected in a tray and are re-weighed after the experiment for gravimetric flow determination.

3.2.3 Experimental protocol

The duration of experiments to evaluate flow sensor performance was 6-7 h. In-line sensors were installed at approximately the midpoint of the cerebroventricular-peritoneal tract. The sensor signal was transmitted via a thin wire (broken line in Figure 3-5) to the flow monitor and laptop computer. To optimize the detection of flow fluctuations, check valves were omitted from the shunt to avoid prolonged zero-flow periods. A 3-way stopcock was placed in the shunt tract distal to the sensor, permitting diversion of shunt flow from the abdomen to a port permitting timed fluid collection for gravimetric flow analysis.

3.2.3.1 Tubing configurations

Opening or closure of stopcocks provided three different tubing configurations for flow measurement by the sensor, gravimetric flow measurement, and cerebroventricular injection of artificial CSF (Figure 3-6). For sensor flow measurements, fluid flowed via the shunt from the third cerebral ventricle into the abdominal cavity. For concomitant sensor and gravimetric flow measurements, the shunt fluid was diverted through a restriction tube and collected in pre-weighed Eppendorf vials. The restriction tube (Figure 3-7) had a smaller internal diameter than the shunt tube, enabling it to function as a shunt valve to provide constant flow restriction. This configuration permitted simultaneous sensor and empirical flow measurements to evaluate the sensor's performance. Artificial CSF (37°C) was injected manually (5, 10, 15 or 20 ml bolus) into the cerebroventricular cannula. Injections were delivered at a steady rate over a 60 s period, during which the sensor

continued to monitor shunt flow, but fluid collection for gravimetric analysis was suspended. There were 3-5 bolus injections over the course of each experiment. After each injection, shunt flow returned to baseline before the next injection. A solid-state pressure transducer (Digi-Med TXD-310, Micro-Med, Inc., Louisville, KY) was connected to the shunt via a stopcock. Cerebroventricular pressures were monitored and recorded during the sensor and gravimetric flow measurements.

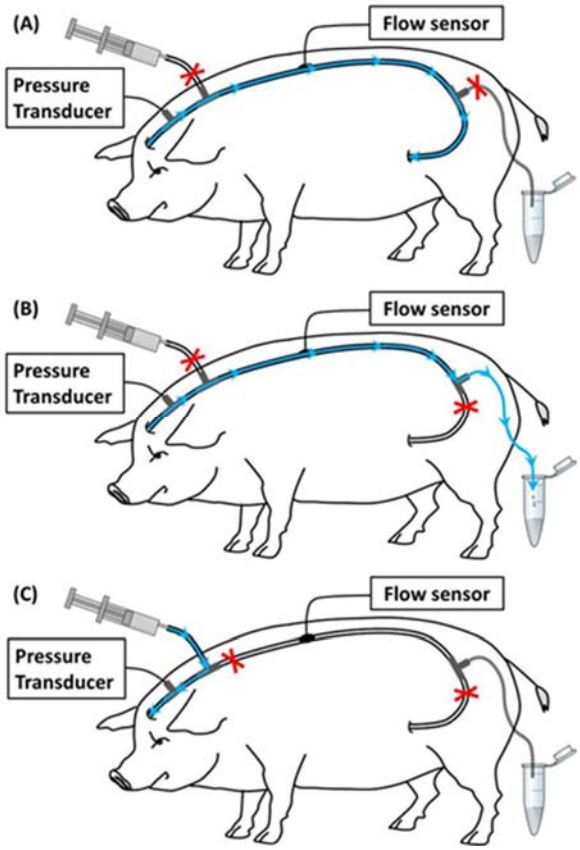

Figure 3- 6 Shunt flow and cerebroventricular pressure measurements. The blue arrows indicate flow direction, and the red crosses indicate the closed ports. (A) Shunt flow measurement by the in-line sensor during venting of CSF from cerebral ventricle to abdominal cavity. (B) Collection of CSF in pre-weighed vials through a restriction tube for gravimetric flow measurements. (C) Assessment of cerebroventricular pressure responses to injection of artificial CSF into the third cerebral ventricle.

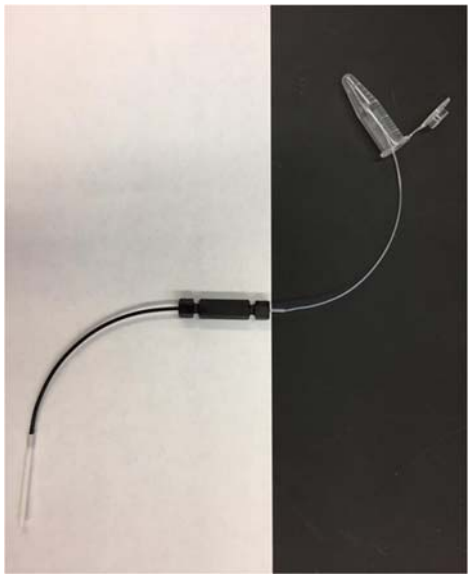

Figure 3- 7 Restriction tube used during animal testing to limit flow rate. The black PTFE (i.d., 1 mm; o.d., 1.63 mm; length, 12 cm) was connected to 3-port valve with a short piece of silicone tube. CSF was collected in a pre-weighed vial from transparent PTFE tubing (i.d., 0.3 mm; o.d., 0.81 mm; length, 15.3 cm).

3.2.3.2 Sensor-reported flow

The flow sensor started reporting flows after the surgical preparation was completed and fluid was flowing through the shunt from cerebral ventricle to peritoneal cavity. The time of the first measurement was defined as t = 0 h. All other measurements were logged relative to this reference. Once started, the sensor continuously measured flows in 30 s segments until the end of the experiment. Each 30 s measurement cycle included 5 s for baseline sensing, 5 s for heating the shunt fluid at the sensor, and 20 s for measuring the flow-dependent decrease in fluid temperature. Figure 3-8 presents the signal obtained over a typical measurement cycle.

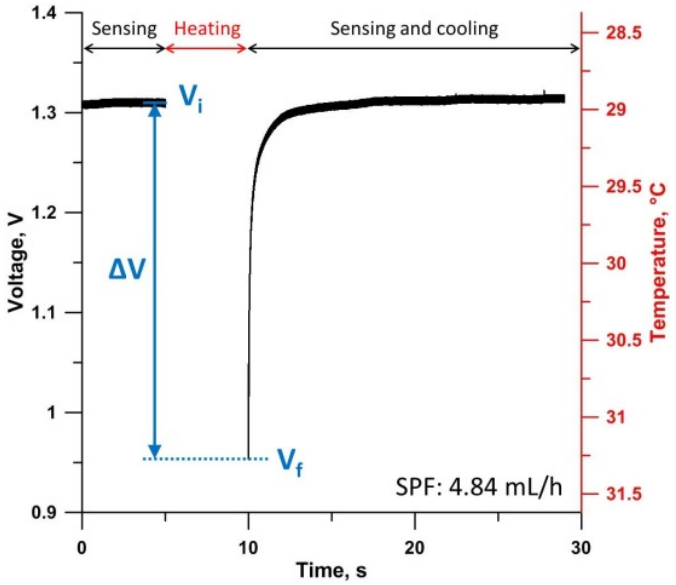

Figure 3- 8 Flow sensor voltage output of a single 30 s flow measurement cycle. Initial voltage V_i is defined as the average signal between 4.891 – 4.998 s. Final voltage V_f is the lowest voltage measured immediately after cessation of the 5 s heat pulse and reestablishment of the Wheatstone bridge. The difference ΔV (= $V_i - V_f$) is proportional to the shunt flow. Data collection continues from 10 to 30 s before initiation of the next cycle. This cycle reported SPF = 4.84 ml/h.

A LabVIEW program automatically performed data analysis at the end of each cycle. V_i, V_f and ΔV were extracted, and then flow (F) was calculated from the calibration curves based on V_i and ΔV, and saved on an Excel spreadsheet. Because CSF shunt flow fluctuations in patients typically follow time courses lasting for hours (37), the sensor's flow measurements at 30 s intervals permit high-resolution detection and quantification of shunt flow fluctuations.

3.2.3.3 Gravimetric flow analysis

Flow was empirically determined by timed collection in pre-weighed Eppendorf vials of effluent from the restriction tube, while sensor-reported flow was monitored concomitantly. Effluent was collected for 5 min per vial, except during the first 10 min after artificial CSF injection, when fluid was collected for 60 s per vial. The vials were

reweighed after the experiment. Effluent volumes were computed based on a CSF density of 1 g/ml (39, 40). Approximately 80-100 gravimetric flow measurements were made in each experiment.

3.2.4 Statistics

Microsoft Excel was used for all statistical analyses. The sensor-reported flows (SRF) were generated every 30 s while samples for gravimetric flow (GMF) measurements were collected for 1 or 5 minutes. The SRF data obtained over the duration of each GMF sample collection were averaged. Outliers were identified based on the SRF/GMF ratio, by the interquartile range (IQR) value. Data that fell below Q1-1.5*IQR or above Q3+1.5*IQR were discarded. The mean and standard deviation of the slope, as well as the correlation coefficient r are shown in Table 3-1; standard statistical functions in Excel were used. The SRF/GMF ratio in these experiments was 0.98 ± 0.09 (mean value ± SD, n = 6), and the 95% confidence interval was 0.88 - 1.07. The linear relationship between GMF as the independent variable and SRF as the dependent variable was examined by standard linear regression methods with or without forcing the intercept through the origin. In no case could the intercept be statistically distinguished from zero, so further analyses examined best fit relationships with intercepts at the origin. These relationships yielded best fit slopes of 0.88 ± 0.01 (mean value ± SD, n = 6) and 95% confidence interval of 0.87-0.90.

Table 3- 1 Slopes and regression coefficients for linear regression analyses of gravimetrically measured (GMF) vs. sensor-reported (SRF) shunt flows.

Experiment #	Slope GMF vs. SRF	SD	r
2	0.91	0.15	0.9476
3	1.20	0.23	0.7256
5	1.17	0.11	0.9612
6	1.13	0.18	0.9467
7	0.85	0.38	0.6200
8	1.01	0.11	0.9629

3.3 Results and Discussion

3.3.1 Sources of error and corrective measures

Two of the eight experiments did not produce processable data. In the first (Experiment 1), the sensor was pre-calibrated in the range of body temperature of the animal (32-39°C). From the cranial entrance, the fluid travels ~35 cm through the shunt outside the body before passing through the sensor housing, and thus has an opportunity to cool towards ambient temperature. To maintain the fluid temperature within the calibration range, in the first experiment we covered the exposed tubing with a heating pad. However, the pad positioning in close proximity to the sensor electronics shifted the sensor response, producing erroneous flow values. A second problem stemmed from the absence of any restriction at the fluid exit during sample collection for gravimetric flow measurement, producing flows that exceeded the upper limit of reported CSF flows by up to fivefold. In subsequent experiments, these problems were solved by (a) calibrating the sensor around the ambient temperature range in which the sensor actually measured flow and (b) adding a restriction tube at the sampling port to limit the flow rate during gravimetric measurement. In Experiment 4, unknown to the experimenters at the time, the thermistor had a poor connection resulting in unpredictable and often subtle baseline shifts which impeded subsequent analysis of the SRF data. A new thermistor was

utilized for the next set of experiments. The other 6 experiments yielded suitable flow signals.

3.3.2 Flow and pressure changes produced by artificial CSF injections

Figure 3-9A presents shunt flows reported by SRF and GMF, and cerebroventricular pressures over the course of a typical experiment (Experiment 8). Altogether, 756 SRF and 108 GMF values were obtained over this 7.2 h experiment. At the beginning of the experiment, shunt flows ranged from 8-10 ml/h. Flows and cerebroventricular pressures gradually fell and eventually stabilized as CSF drained through the shunt. To test sensor performance at various flow rates, 5, 10 or 15 ml of artificial, pre-warmed (37°C) artificial CSF electrolyte solution were injected into the third cerebral ventricle at 1.7, 3.3, 4.5 and 6.3 h. These injections produced abrupt flow surges and brief increases in cerebroventricular pressure that were roughly proportional to the injected volume. In the 6 experiments, pre-injection baseline cerebroventricular pressures averaged 3.3 $\pm$ 0.6 mm Hg (mean $\pm$ SEM). Injections of 5, 10, 15 and 20 ml produced peak pressure increases of 12.5 $\pm$ 2.5, 45 $\pm$ 6.2, 56 $\pm$ 5.3 and 74 $\pm$ 2.1 mm Hg, respectively. Thus, there was a roughly linear relationship between the injected fluid volume and the resultant increase in cerebroventricular pressure. These pressure increases were temporary and returned to baseline within 2-5 min as the injected volume exited the ventricle, either through the ventriculoperitoneal shunt or, as discussed below, via the normal anatomical drainage through the cerebral aqueduct and fourth ventricle.

In Experiment 5 (Figure 3-9B), flow was diverted into the peritoneal cavity at t = 1.3 and 1.75 h. Because the ventriculoperitoneal shunt configuration imposed less resistance than the resistance tube drainage, shunt flow increased during these diversions. In each case, the sensor reported the flow surges promptly. In Experiment 6 (Figure 3-9C), the shunt was clamped six times to temporarily interrupt flow, at 1.7, 2.9,

3.3, 3.7, 4.3, 4.7 and 5.2 h, and in each case, the flow sensor reported zero flow. At t = 5.1 h, a 20 ml artificial CSF injection produced a peak flow of 20 ml/h followed by a decline to 10 ml/h within 2-3 min. Thus, the injections produced temporary increases in cerebroventricular pressure and shunt flow that gradually subsided as the fluid drained.

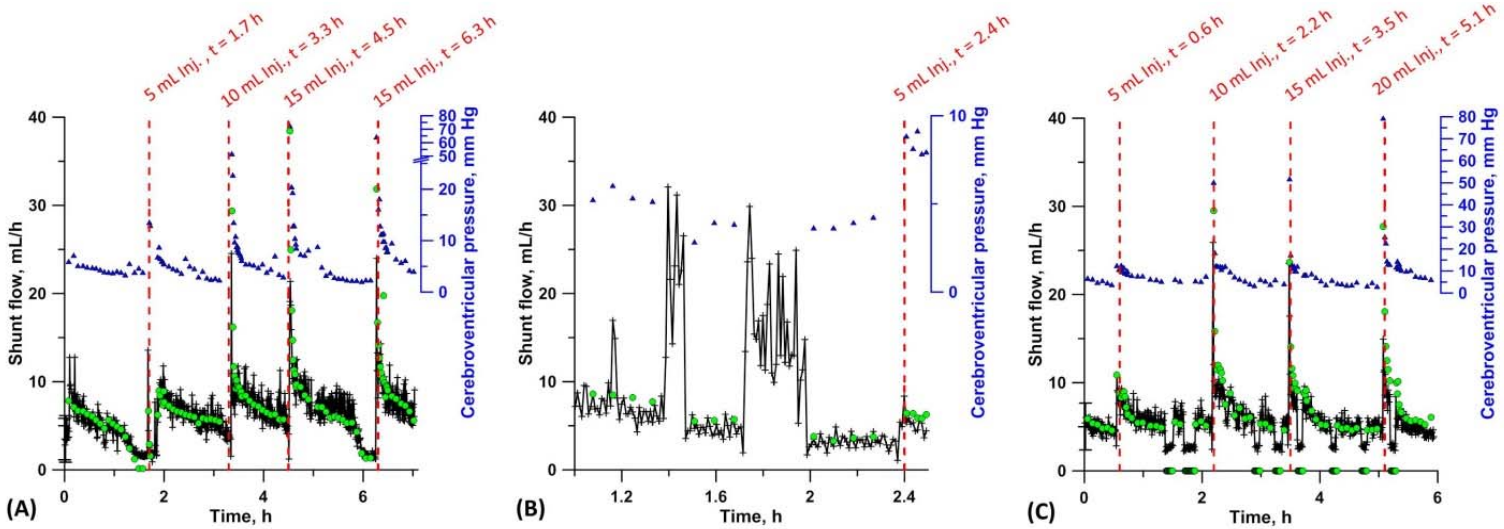

Figure 3- 9 Impact of bolus injections (vertical broken red lines) of artificial CSF on cerebroventricular pressures (blue traces) and temporal shunt flows determined by the flow sensor (black traces) and gravimetric measurements (green circles). (A) Flows and pressures during experiment 8. Volumes and times of intracerebral injections are indicated. (B) A 90 min portion of experiment 5 is shown to demonstrate the rapid response of the flow sensor to phasic changes in shunt flow following artificial CSF injections. (C) Values from experiment 6, in which the consistency of these zero-flow readings demonstrated a stable sensor baseline.

A baseline shunt flow of 1.81 $\pm$ 0.26 ml/h/kg body mass was determined by GMF measurement. Analysis of the increased post-injection flow revealed that 28.7 $\pm$ 2.1% of the injected volume was recovered from the shunt; thus, approximately 70% of the injected fluid did not drain through the shunt. The experiments were conducted on healthy animals with anatomically intact CSF circulation, which very likely allowed most but not all of the injected fluid to pass from the third to the fourth ventricle, and ultimately into the subarachnoid space. The temporarily elevated cerebroventricular pressures produced by the injections would have increased this natural CSF drainage, causing shunt flows to subside within a few min after injection. Figure 3-10 shows the complete results of the six experiments.

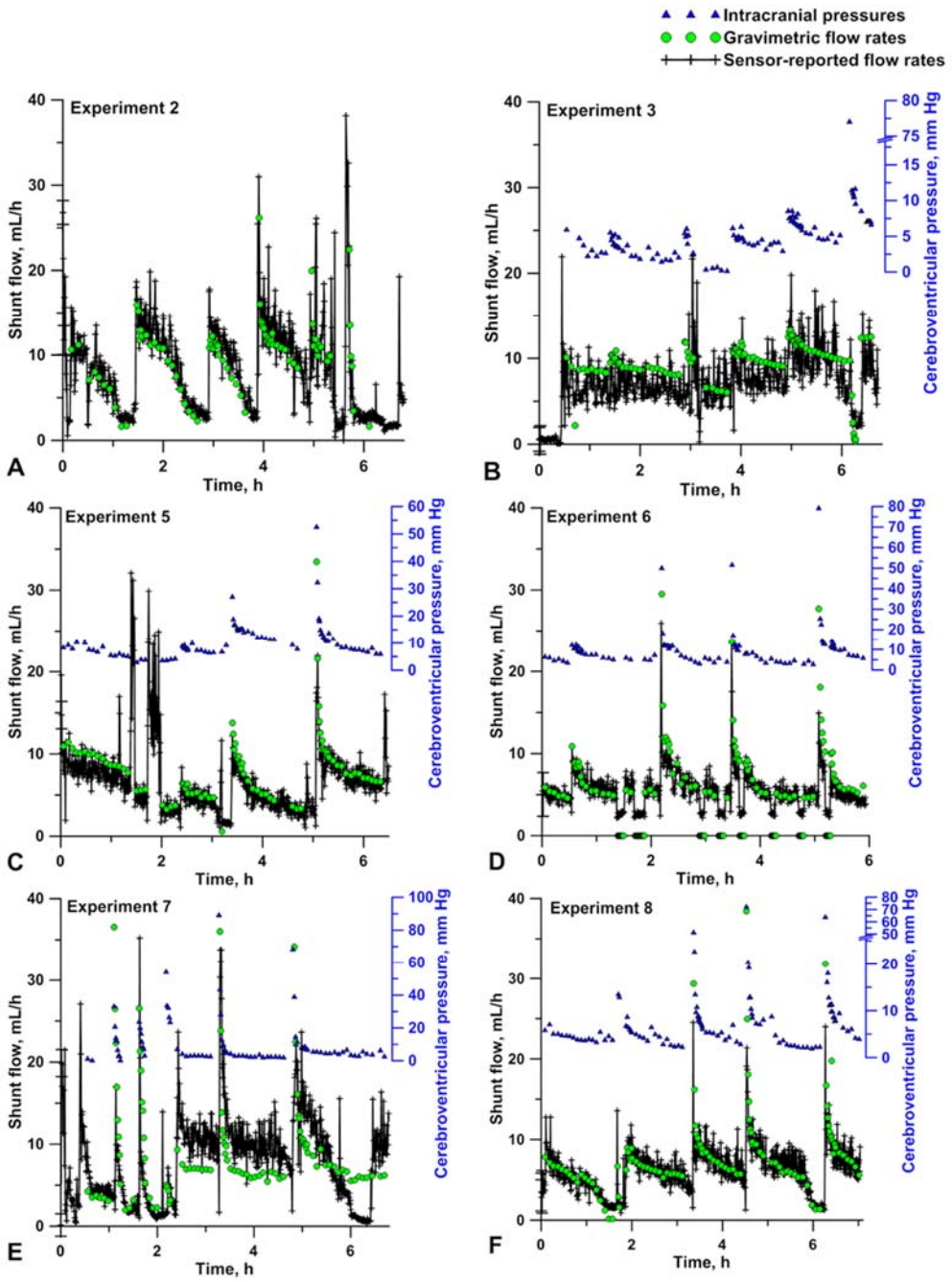

Figure 3- 10 Steady-state shunt performance and effect of cerebroventricular fluid injections. Cerebroventricular pressures (blue triangles), gravimetric flow (green dots) and sensor-reported flow (black crosses) are plotted vs. time for the six successful experiments.

Table 3-2 Total number of flow rate measurements and the time and volume of infusions.

Experiment #	# flow sensor measurements	# gravimetric measurements	1st infusion		2nd infusion		3rd infusion		4th infusion		5th infusion		6th infusion	
			Volume (mL)	Time (h)	Volume (mL)	Time (h)	Volume (mL)	Time (h)	Volume (mL)	Time (h)	Volume (mL)	Time (h)	Volume (mL)	Time (h)
1	456	41	10	2.9	20	3.0	30	3.3	10	3.6	20	3.9	30	4.1
2	756	90	10	1.4	5	2.9	15	3.9	15	4.9	15	5.6	\	\
3	720	103	5	1.4	10	2.9	10	3.8	15	4.9	25	6.2	\	\
4	456	84	10	0.0	5	1.4	15	2.6	20	3.7	\	\	\	\
5	732	88	5	2.4	10	3.3	15	5.0	\	\	\	\	\	\
6	636	83	5	0.6	10	2.2	15	3.5	20	5.1	\	\	\	\
7	732	86	5	1.1	10	3.3	10	4.8	\	\	\	\	\	\
8	756	108	5	1.7	10	3.3	15	4.5	15	6.3	\	\	\	\

3.3.3 Sensor Calibration

Preliminary work showed no difference between sensor calibrations conducted with simulated CSF solutions vs. pure water; this may indeed be expected based on their virtually identical thermal properties. Sensor calibrations were therefore carried out with water, generating the data shown in Figure 3-2, 3-3 and 3-4. The sensor output during the actual experiments was translated to flow rates using such calibration data. The close correspondence of the SRF and GMF values in the animal experiments suggests water can serve as a convenient flow calibrant. The sensor baseline output fluctuated in synchrony with the respiratory rhythm of the animal (Figure 3-11); this can be ascribed at least in part to CSF flow changes associated with fluctuations in cerebroventricular pressure during positive-pressure, mechanical ventilation (41, 42). Despite these fluctuations, the sensor generated accurate flow metrics.

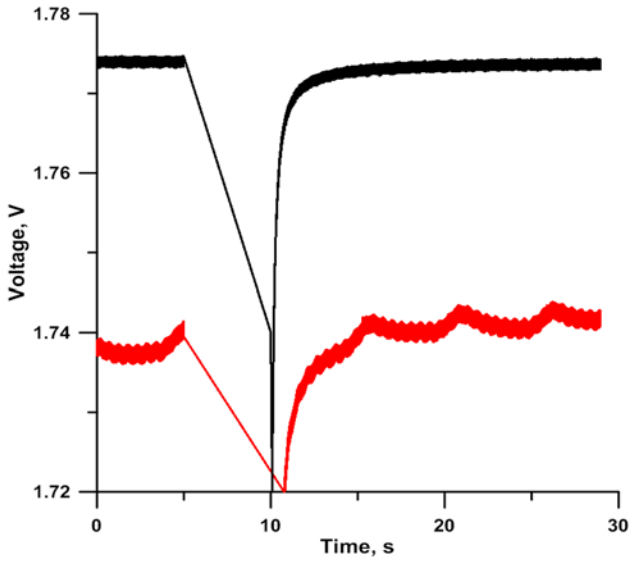

Figure 3- 11 Voltage output of the flow sensor in flow measurements. Heat pulse was applied to thermistor during t = 5 – 10 s; during all other times thermistor was in the sensing mode. The black trace shows a measurement trace during a controlled temperature laboratory set up. The red trace is from one of the animal experiments; the voltage signal (the observed temperature) fluctuates in synchrony with the respiratory rhythm of the animal.

3.3.4 SRF and GMF Comparison

Figure 3-12A presents a scatter plot of the values reported by the SRF vs. GMF methods. A total of 506 pairs of SRF and GMF data obtained simultaneously from six experiments are shown. Least-squares linear regression correlation coefficients for individual experiment were between 0.88 and 0.99, indicating robust concordance of SFR and GMF. Although some variation around the line of identity was observed, the average SRF/GMF ratio was 0.98 ± 0.09, and the 95% confidence range of 0.88-1.07 encompassed unity, indicating the sensor accurately measured shunt flow.

The accuracy of SRF was further examined by a Bland-Altman plot, where the differences between the two paired measurements are plotted against the average (Figure 3-12B). On average, GMF reports flows only 0.07 ml/h above SRF, indicating the sensor accurately reported shunt flow. The Bland-Altman plot revealed widening of the SRF-GMF difference at higher flows, suggesting the variability of the difference is not constant. When the differences are expressed as percentages of the mean of SRF and GMF, the data scatter is nearly constant over a broad flow range (Figure 3-12C). The two methods showed robust agreement from a statistical point of view, but from a clinical standpoint, little information is presently available about the acceptable limits of shunt flow measurement. Currently available hydrocephalus diagnostics provide only “on/off” information about CSF flow; consequently, the intermittence of CSF flow (27) may produce false findings. The sensor’s robust detection of shunt flow in the present study suggests this technology may eventually afford greater reliability and precision than current methods for clinical assessment of shunt performance

.

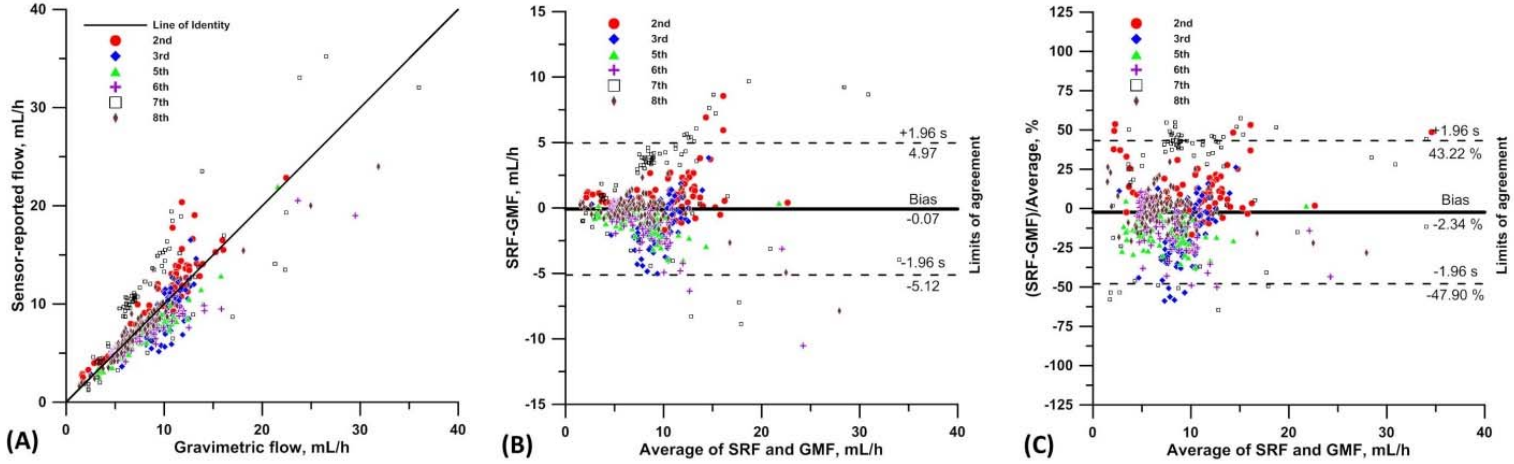

Figure 3- 12 Comparisons of flows reported by the sensor vs. gravimetric determination by (A) regression analysis, (B) Bland-Altman plot of the differences between the concurrent sensor and gravimetric values, and (C) Bland-Altman plot of differences presented as percentages of the mean flow values. In panel A, the different symbols represent data from each of the six experiments. The two flow measurements yielded robust correlations approximating the line of identity, where linear regression analysis of plotted data yielded r2 = 0.9412. In panels B and C, the solid lines represent the mean value of the difference between sensor-reported and gravimetric flows, and the broken lines represent the upper and lower limits encompassing 95% of the individual differences

3.3.5 Choice of pulse voltage

In retrospect, the choice of using a 9.6 V pulse compared to the original 8.2 V operation was unwise. Although there was no obvious indication of malfunction (the signal returned to baseline before the next pulse) the devices apparently did suffer from the added thermal stress. Post-hoc examination of the data indicates that the sensors performed well for two experiments plus added calibration runs at 9.6 V, but began to falter by the third experiment and failed by the fourth. When 8.2 V pulses were applied in vitro, the sensors performed reliably without functional deterioration (1).

3.4. Conclusions

We have demonstrated the functionality of a previously reported hydrocephalus shunt flow sensor in anesthetized pigs. More than 4300 acceptable flow measurements were taken in six acute experiments. The sensor proved to accurately report flow of porcine CSF at ambient temperatures. The shunt and sensor were placed externally to permit gravimetric flow measurements; a crucial next step in development will be to interrogate the long term performance of the sensors when implanted subcutaneously in chronically instrumented animals, using wireless communication and instrument control technology. Application of higher voltage pulses produced minimal enhancement of flow resolution and adversely affected sensor longevity. Accordingly, future experiments will utilize electrical pulses < 8.2 V.

Chapter 4

TIME OF SIGHT LIQUID FLOW MEASUREMENTS IN THE LOW NANOLITERS PER MINUTE SCALE

4.1 Introduction

Aside from microfluidic systems, many present capillary scale analytical approaches operate at flow rates below 25 nL/min. Recent examples include open tubular ion chromatography columns with a van Deemter optimum at 18 nL/min,(43) LC-MS/MS systems based on packed 25 μm i.d. columns operating at ≤ 10 nL/min,(44) CE-MS systems operating at 5 nL/min,(45) to open tubular reverse phase LC separations in 2 μm i.d. columns operating at a flow rate of 0.2 nL/min. (46) Pumping and gradient generation systems that can operate at the nL/min scale have been described;(47-49) some are commercially available. Low pressure infusion pumps used in biomedical research routinely operate down to 17 nL/min;(50) even implantable versions that go down to 33 nL/min with a battery life of up to 7 years are in routine use. (51) Reviews cover how high pressure pumps may operate in a split or splitless manner(52, 53) to generate flows in the nL/min regime but practical methods for reliably monitoring such flow rates, especially those that can accommodate solvent gradients, are scant. Precise flowmetry is essential for the overall reliability and integrity of analytical systems. At sub-μL/min flow rates, any leak evaporates long before it is visible. We know firsthand that an affordable monitor applicable in this flow regime can greatly facilitate instrument/method development as well as help troubleshoot processes that operate in this flow scale.

Low liquid flow measurements have traditionally relied on gravimetry, thermal methods, or front tracking measurements (see below). The liquid is allowed to flow into a small vessel, or a narrow bore transparent tube. This allows (periodic) mass or volume estimation. Such approaches become tedious and error-prone for sub-μL/min flow rates

because of inordinately long times needed for a single measurement. Corrections for evaporation, thermal influence, pulsation, buoyancy, etc. need to be implemented. (54) While in some cases all of these can be properly carried out, near real-time flow measurements simply are not possible, of particular concern when flow rates vary. The urgent need for a device that can measure flow rates down to ~1 nL/min has been elegantly stated by NIST researchers. (55)

4.1.1 Thermal flowmeters

The only commercial liquid flow sensors operable in the sub-μL/min scale are thermal mass flow sensors. They operate on the same decades-old proven principles as their larger flow counterparts. The review by Kuo et al. (56) covers these principles, which can be broadly classified as relying on calorimetry and anemometry as well as measurement of time of flight of a thermal pulse. Commercially available sub-μL/min sensors rely solely on calorimetry. Such sensors justly boast of no moving parts, small size, low power consumption, fast (40 ms) response and bidirectional flow sensing capability. Drawbacks include nonlinear and acutely temperature-dependent response; however, both are compensated for by appropriate firmware, active temperature sensing and/or thermal isolation. Some question their long-term stability,(57) but by far their greatest Achilles heel is fluid-dependent response. This renders them incompatible with temporally variable fluid composition, as in gradient liquid chromatography. Individual flow sensors in separately pumped component streams add cost and complexity; in any case, different liquid volumes are not strictly additive. Also, thermal diffusion effectively sets a lower limit to the smallest measurable flow rate. Currently such sensors cannot quite reach the low flow rate measurement limits attainable by front-tracking (see below). The lowest flow range commercial sensor has a full scale span of 0-1500 nL/min and the lowest calibrated flow rate (LCFR) of 70 nL/min (~5% of full scale). (58) At the LCFR, the

noise equivalent is 2 nL/min, from which the lower measurement limit will be ca. 6 nL/min (~0.5% of full scale). Although the vendor will not specify an accuracy of better than 10% of the measured value or 7.5 nL/min, whichever is greater, repeatability specifications are an order of magnitude better.

Articles on microfabricated thermal flow sensors are simply too numerous to be adequately covered here. While many have impressive features, e.g., ready manufacturability,(59) isolation of the sensor from the fluid,(60) routine operation at 50 nL/min,(61) or an entire array of sensors along the flow channel to provide unique capabilities,(62) none directly demonstrate a lower measurement limit than the commercial sensor cited above.

4.1.2 Gravimetry and front/interface tracking

Many efforts have been made to reduce the lower limit of the applicable measurement range. Richter et al. (63) considered flow measurements in channels of different geometry and made measurements over a 10 -106 nL/min range, using both gravimetry and tracking of the meniscal front. They found gravimetry to be impractical below 100 nL/min and developed a microscope system to track the meniscus. Ahrens et al. (64) mounted the observation setup on a high precision linear stage, permitting observation of 15 cm length of a 150 μm i.d. precision bore glass capillary. At a flow rate of 5 nL/min, the uncertainty was 8.3% for a 60 s observation period. The observation length permitted up to 9 h of measurement at this flow rate. The uncertainty asymptotically approached a minimum of 5.4% for longer observation periods or higher flow rates. Westin et al. (65) also used an optical approach in the form of a laser-based distance meter by looking at the meniscus from the top. Flow rates as low as 1.8 nL/min could be measured in a 2 mm dia. micromachined well with an uncertainty of 3 % for a non-volatile fluid like hexadecane. For ethanol, subject to evaporation, this deteriorated to

6 nL/min, after compensation for evaporation. Quite possibly this approach can be extended to lower flow rates with smaller i.d. observation wells. Optical interface-tracking approaches are indeed promising for further pushing down the lower measurement limit; however, the cost/size of the optical components hardly enable stand-alone flow sensors.

To this end, IBM researchers provided a simple and inexpensive way to monitor liquid displacement in a microfluidic chip environment by monitoring the capacitance between two parallel electrodes patterned longitudinally along the flow channel. (66) Although it was not exactly experimentally demonstrated as such, the authors suggested an attainable resolution of 1 nL/min at a 1 Hz data rate. The actual lowest flow rate measured was not stated. Unlike optical meniscus tracking, the response will be dependent on the dielectric properties of the liquid. One common limitation for all methods tracking a moving liquid-air interface is the need for evaporation compensation; this can become acute at low flow rates, and variable temperatures. Perhaps even more vexing is that all the above methods are subject to the finite observation window problem; once the interface moves out of the observation window, one will have to clean the slate/empty the bucket and begin anew.

4.1.3 Time of flight (TOF) sensors

In fluid flowmetry, TOF measurements have a long and illustrious history. In his 1964 paper, Levy(67) traces soap bubble-based gas flowmetry at least to 1875. The soap bubble closely meets the necessary criteria of being a frictionless piston. (68) The obverse case, introducing gas bubbles in a liquid flow stream and noting the time of passage between two fixed observation points is a logical extension. In this case, the “frictionless” criterion may seem unnecessary as liquids are incompressible; however, if there is a significant pressure drop between the two observation points, the volume of the gas bubble can change. The piston aspect, i.e., that there is no liquid slip around the

bubble via a liquid wall film is, however, a requirement. It also becomes more difficult as the observation tube diameter is decreased to accommodate very low flow rates, increasing the bubble wall contact area to bubble volume ratio. In a remarkable paper (only 5 pages long, in which he also studied pressure-drop based and calorimetric flow sensors), Schnell(69) described an air bubble-based TOF sensor, the passage of the bubble/liquid interface being detected optically. While the observation portion was a 2 mm ϕ glass tube, the rest of the manifold was of elastomeric silicone. He devised a set of four electromechanical pinch valves to periodically reverse the flow to prevent the bubble from exiting the system. Because of finite solubility of air in aqueous liquids, it would, however, eventually dissolve. So a fifth valve was used to introduce a ~50 μL volume air bubble when needed. Geller(70) first proposed the generation of H_2 bubbles as flow markers, others have followed since. (71, 72) These sensors operated at a high flow rate range. Wu and Sansen(73) chose to both generate and sense O_2 electrochemically and demonstrated operation at low μL/min scale. More recently, using a microfabricated setup, Lippman et al. (74) passed the fluid over a zone heated by a voltage pulse sufficient to boil the liquid to create a short bubble (ca. 10 mm) or introduced longer bubbles with a syringe. They had an array of sensing electrodes (each ca. 1 mm wide) on either side of the flow channel that sensed the presence of the bubbles (either passing over a single pair of electrodes) or the TOF between any two electrode pairs. Tangible response to flow rates as low as 20 nL/min was demonstrated by examining the signal during the time a single bubble crossed a single pair of electrodes. Otherwise this was largely a concept demonstration: to utilize the latter principle, bubbles of highly reproducible size must be introduced, a difficult task. In general, bubble based TOF flow sensing suffers from compressibility and solubility of gas bubbles. Bubble size changes

as temperature/fluid composition/pressure drop changes. In addition, bubble generation itself is dependent on pressure, flow rate, and the fluid.

For these reasons, there have been efforts to use non-bubble markers for TOF measurement. Miller and Small(20) and Togawa et al. (75) independently invented the thermal pulse TOF flow sensor. In the Miller and Small version, one thermistor generates a heat pulse and a downstream thermistor detects its arrival. Poghossian et al. (76) electrochemically generated H^+ - or OH^- -upstream and a solid-state pH sensor downstream. None of these approaches, however, could go below the μL/min limit.

4.1.4 Fluorescence photobleaching

Photobleaching of a fluorescent dye is well known. Imagine a fluorophore flowing through a conduit crossing an intense laser beam. The amount of dye that will be bleached at steady state is related to the photon dosage a given volume of the dye solution receives. At constant laser flux, this then depends on the residence time of the solution through the beam and thus on the solution flow rate. Sugarman and Prud'homme(77) were the first to suggest this as a means of measuring flow rate. Wang(78) subsequently utilized the same principle to measure low flow rates in microfluidic chips. More recently Patrone et al. (55) have theoretically and experimentally investigated such systems in exemplary detail for flowmetry at low nL/min. Their device, connected to the end of the flow system of interest, uses fiber optic illumination (488 nm) of a microfluidic channel bearing fluorescein, the transmitted light is monitored by fiber optic 2 to monitor the actual laser flux. Fiber optic 3, placed immediately downstream of the excitation fiber, monitors the 520 nm emission; the observed fluorescence intensity asymptotically increases with increasing flow rate.

4.1.5 Diaphragm distension sensing

A recent paper by Sharma et al. (79) extends flow measurement amazingly to the 1 pL/min scale. The flow from a system of interest terminates in an otherwise enclosed cavity atop a piezo resistive pressure sensor, the deflection of the deformable diaphragm in the cavity is monitored. Once the maximum distension is reached, the pressure is vented by appropriate valving. Time will tell the utility of such flowmetry in nanoanalytical systems and the degree to which thermostating will be necessary to avoid fluid thermal expansion effects, or the longevity of ultrathin silicon diaphragms in contact with real liquids. This and many other flowmetry approaches above also have another common (albeit mostly minor) limitation; they can only be used at the exit end of a flow system.

4.1.6 Time of flight vs. time of sight

In TOF flowmetry, there are two principal variants: (1) The marker (e.g.) a gas bubble, is generated ahead of two detectors, crossing the first detector starts the TOF clock and crossing the second detector stops it; (2) Some transducer generates the marker (e.g., H_2/O_2 bubbles or a thermal pulse, simultaneously starting a clock. The clock stops when the marker reaches the single downstream sensor. Implicit in this scenario is that the marker size is insignificant: as literally referring to the TOF of an airplane between two airports, one doesn't quibble about whether it is the aircraft front or rear wheels touching the tarmac stops the clock. In reality, however, most often the passage of the marker (or even the marker meniscus) does not represent an instantaneous perturbation in the signal like a square wave. It could be a peak-shaped but gradually tailing thermal pulse signal or a gradual approach to a plateau as an interface passes through the detection window. Consider also a situation where there are multiple markers in sequence. For the detector, this would be like a multi-car train passing through its field of vision. Such an arrangement can in principle provide a very large dynamic range over

which flow rates can be measured: in traditional TOF flowmetry, the system always has a relatively limited optimum measurement range, at higher flow rates, the TOF is too small, leading to poor flow rate resolution and at low flow rates, it takes too long to acquire a single reading leading to poor time resolution. Sticking to the train analogy for a multi-segment marker system (where the detector can distinguish between the contiguous segments), there is a great deal of latitude on what is measured in a train comprising cars of very different lengths. For slow flow rates one can simply look at the passage of an interface. At higher flow rates this may be the TOS for a given train car crossing the field of vision and at still higher flow rates, the TOS for the entire train. For very slow flow rates of present interest, the TOS may do more than just rely on the passage of a segmental interface that typically involves the gradual transition of the detector signal from one stable value to another, it may advantageously zoom in on that transition zone and the TOS value of interest may simply go from any arbitrarily chosen signal voltage to another in the signal transition zone.

4.1.7 Meeting the requirements of multi-marker time of sight flowmetry

In principle, a bubble TOF flow meter can be operated in the interface-passage TOS mode using arbitrarily chosen signal values as start and stop points. This is not entirely free from problems as the meniscal geometry may change if the fluid composition changes. In any case, the entire bubble length cannot be used as a TOS measurand unless that length is highly reproducible. This is difficult if a new marker is introduced for each measurement. Even if a reproducible means, e.g., a loop injector or equivalent, is used to introduce a fixed size marker, it will be difficult to accommodate the introduction of a contiguous segmentally reproducible multi-segment marker. We solve this by recirculating (following Schnell(69)) the same marker train via repeatedly reversing the flow in the observation loop soon as the marker of interest has provided the desired

reading. While functionally the same, our system uses a single 2-position 4-port valve, rather than four independent on/off valves. A gas bubble is impractical as a long-lasting marker. We propose the use of multiple immiscible liquid segments. Specifically, we use fluorocarbon (FC) segments of high resistivity (ρ), and low dielectric constant (k) that are optically transparent. The FC segments then bracket a very different liquid, a low ρ, high k liquid, e.g. an aqueous salt solution or even a liquid metal like mercury which is also optically reflective. An illustrative multi-segment marker train is shown in Figure 4-1.

Figure 4- 1 Illustrative multi-segment marker consisting of fluorocarbon segments (gray) and immiscible conductive segments (red) consisting of a salt solution or a liquid metal. Note deliberately differing segment lengths. The terminal FC segments are not used for measurement.

The terminal FC segments are considered “guards”. Despite the extremely low solubility of FC’s in any non-FC solvent, if any FC is removed by dissolution in the measured liquid, they will be removed from these terminal segments and not from any inner segments they protect and prevent a dimensional change of the protected segments. Finally, to protect from the intrusion of the measured liquid stream past the guard segments, the silica observation tube is fluorosilylated; the high affinity of the FC-coated wall for the FC segments essentially eliminate the possibility of an intermediary wall film of any other liquid.

We thus report here a simple, robust, inexpensive, stand-alone nano flow sensor for measuring liquid flow rates down to ~1 nL/min. In this initial exposition we present the general configuration and demonstrative performance data for the 1.5 -15 nL/min flow range.

4.2 Experimental section

4.2.1 Chemicals

Milli-Q water was used to prepare aqueous solutions. 50 mM ammonium acetate (www.alfa.com), hereinafter AA, was used as the conductive aqueous segment. Aqueous ammonium acetate at a lower concentration (0.5 mM) was used as the illustrative test fluid (TF) the flow of which was measured. All solutions were filtered through 0.45 μm Whatman poly(ether sulfone) membrane filters (www.fishersci.com). The fluorocarbon chosen was Fluorinert® FC-40 (www.3m.com), hereinafter denoted as FC, because of its high boiling point (158-173 °C). Trichloro(1H, 1H, 2H, 2H-perfluorooctyl)silane (TCPFOS) (www.sial.com) was used for fluorosilylation.

4.2.2 Capillary observation tubes. Rendering a silica capillary wall fluorophilic

PTFE capillaries of i.d. up to 300 μm (www.zeus.com), custom extruded cyclic olefin polymer capillaries(80) of 28 μm i.d. and 360 μm o.d., silica capillaries of various inner diameters and 360 μm in o.d., were used as the observation tubes. All of the data reported here, however, pertain to an 11 μm i.d., 35 cm long polyimide-coated fused silica capillary (www.molex.com).

To make a fluorophillic wall, the capillary was successively washed by 0.1 M ethanolic KOH, water, 0.1 M HCl and water, spending ca. 15 min at each step and finally dried by blowing filtered dry N_2 through it and TCPFOS was aspirated into it and left to react overnight. After the spent/excess reagent was forced out with N_2, the capillary was rinsed with FC. A comparison of the air-fluorocarbon interface between untreated and TCPFOS-treated fused silica capillaries indicates that the contact angle for FC markedly decreases upon TCPFOS treatment. (Figure 4-2 and Figure 4-3 for changes in the FC – air and FC – water interfaces). Without fluorosilylation, in a hydrophilic capillary, over time the aqueous liquid slips past the FC segment (Figure 4-4).

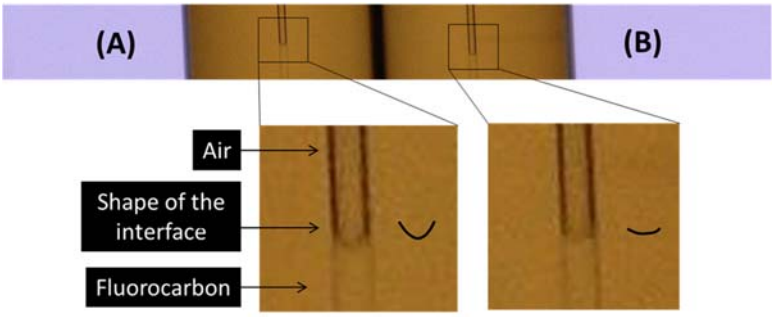

Figure 4- 2 A comparison of air-fluorocarbon interface between (A) trichloro(1H, 1H, 2H, 2H-perfluorooctyl)silane (TCPFOS)-treated fused silica capillary (B) untreated silica capillary. The interface shown in (A) has a larger curvature than in (B), indicating a successful fluorophilic surface treatment.

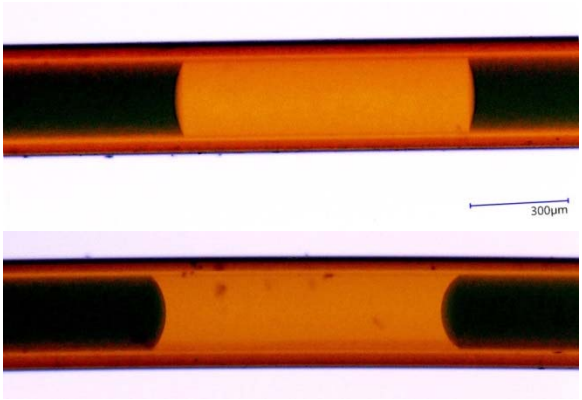

Figure 4- 3 Same as Figure 4-2 but larger bore 180 μm capillaries and aqueous phase dyed with methylene blue for ready visualization. The center segment is fluorocarbon FC-40 in both panels. The top is normal (untreated) fused silica capillary; the bottom capillary has been fluorosilylated. Note the dramatic change in the direction of curvature of both phases.

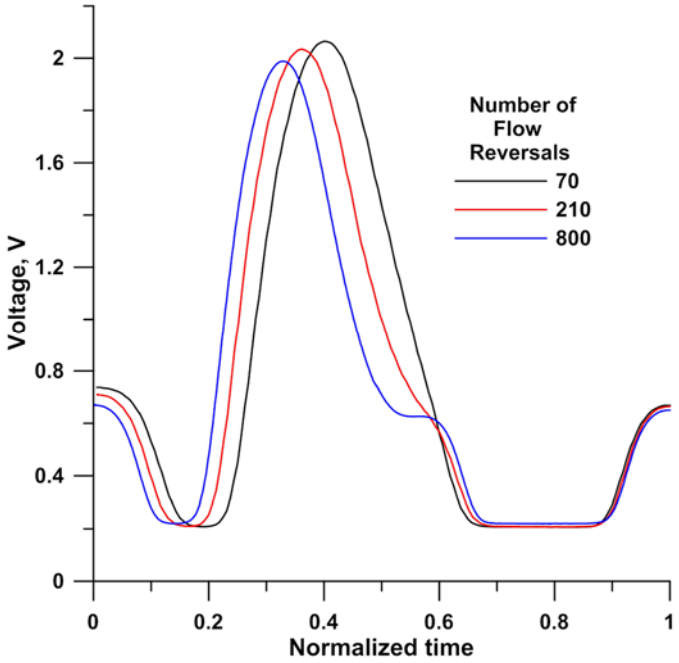

Figure 4- 4 Aqueous liquid slip past FC segments in a hydrophilic 11 μm i.d. untreated fused silica capillary. A three-segment marker FC (2 mm)-(Hg, 2mm)-FC (2 mm) was put in a hydrophilic capillary and driven back and forth with 0.5 mM ammonium acetate as the test fluid. The figure depicts the admittance detector output during the passage of the marker after the specified number of flow direction changes. The initial marker passage looks close to the black trace, which was obtained after 70 flow reversals. Over a period of time, some ammonium acetate accumulates on one side of the mercury segment, developing a "knee" as shown in the red trace (after 210 flow reversals). This becomes more pronounced in the blue trace (after 800 flow reversals). Why the accumulation occurs on only one but not both sides of the Hg segment is not understood.

4.2.3 Generation of multi-segment flow markers

The procedure for setting up the minimum configuration of a multisegment marker that includes a provision for simultaneously monitoring the flow by a reference method is as follows. For the reference measurement, we monitored the movement of a separate segment by a high magnification digital video microscopy (VHX-5000, www.Keyence.com). Regardless, observation inside a polyimide coated capillary, ~10 μm in i.d. with a wall more than 17× as great in thickness, is not trivial. It was simply

impossible to observe an FC-aqueous liquid interface, regardless of attempts to dye the aqueous phase with a colored or fluorescent dye. Of all the markers we tested, mercury was the easiest to follow. As illustrated in Figure 4-5, the reference and measurement segments, separated by 1 cm, respectively comprised a ~2 mm mercury segment in the middle of the test fluid and an FC/AA/FC (~5/2/5 mm in length) train as the multisegment marker.

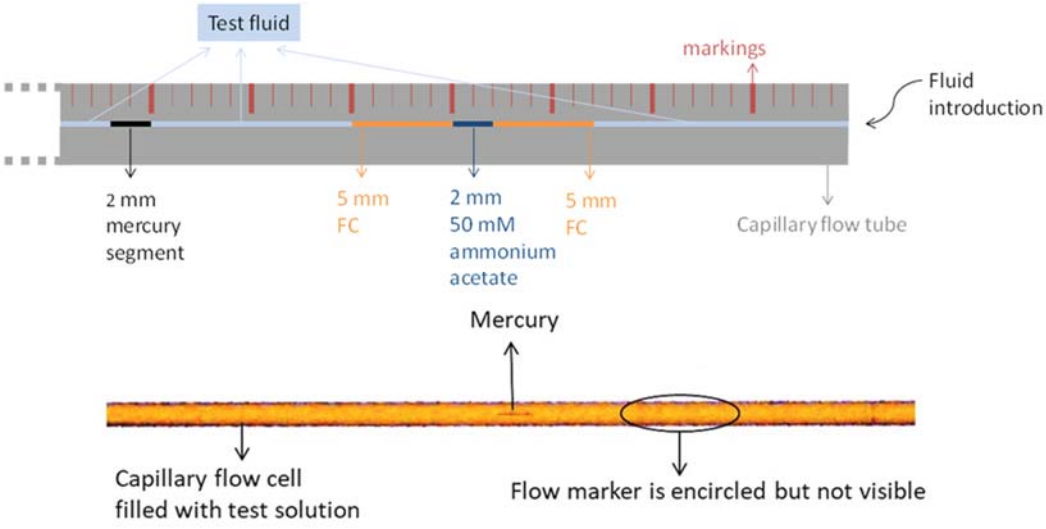

Figure 4- 5 Top: Schematic of the capillary observation tube at the fluid introduction end. Bottom: The microscopic view of the capillary flow cell with mercury segment and flow marker introduced. In an 11 µm i.d. capillary, the fluorocarbon - aqueous solution interfaces were not visible. Ink markings were removed following marker introduction.

To help at least approximately achieve the desired marker lengths, a 10 cm length of the capillary was marked every mm with a fine-tip marker. All liquids were introduced into the capillary using dedicated 1 mL syringes using appropriate Luer adapters to threaded unions. The flow cell was first filled with the test fluid. Then, 2 mm Hg, 1 cm TF, 5 mm FC, 2 mm AA and 5 mm FC were injected in sequence. In all cases, the amount of the liquid initially introduced is longer than eventually intended. Mild back

pressure is applied to expel the excess and the next liquid syringe is attached towards the end of this process. Finally, the mercury and segmental flow marker were pushed to the middle part of the flow cell by more test solution. Note that the aside from serving as the microscopic flow marker, the Hg segment served an important purpose, it allowed following the visualization of the introduction process of FC-AA-FC marker train, as the FC-AA interface was not easily discernible. Note that once assembled and calibrated, the sensor itself does not require mercury.

4.2.4 Interface detectors

Both optical and admittance approaches were used. A simple red LED-photodiode based transmittance detector with a pinhole aperture successfully detected the interface in 300 μm i.d. tubes (Figure 4-6).

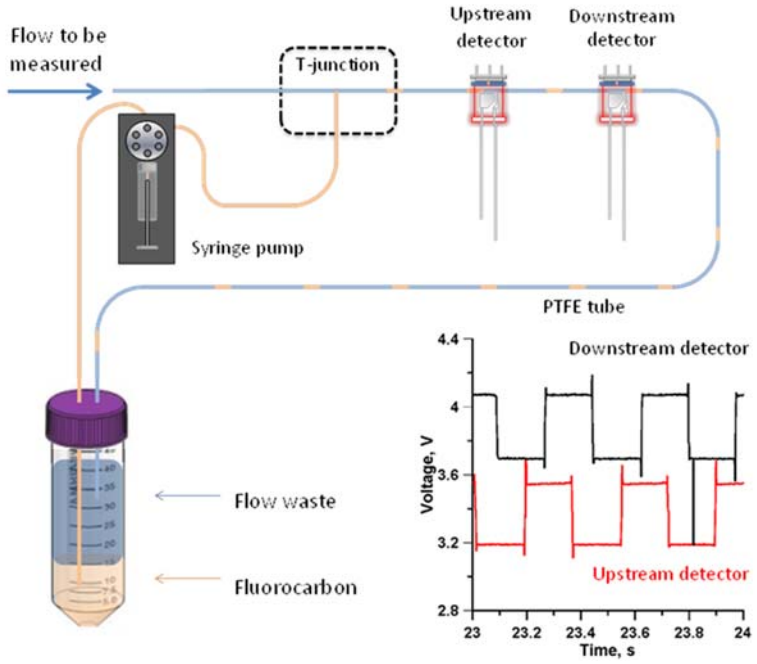

Figure 4- 6 Experimental setup for first experiments utilizing FCs as ILMs.

The FC-AA interface was observable in a similar detector on a 28 μm i.d. tube if the AA phase was doped with a dye to decrease its light transmission further (Figure 4-7). However, this approach could not be further downscaled to narrower bore capillaries.

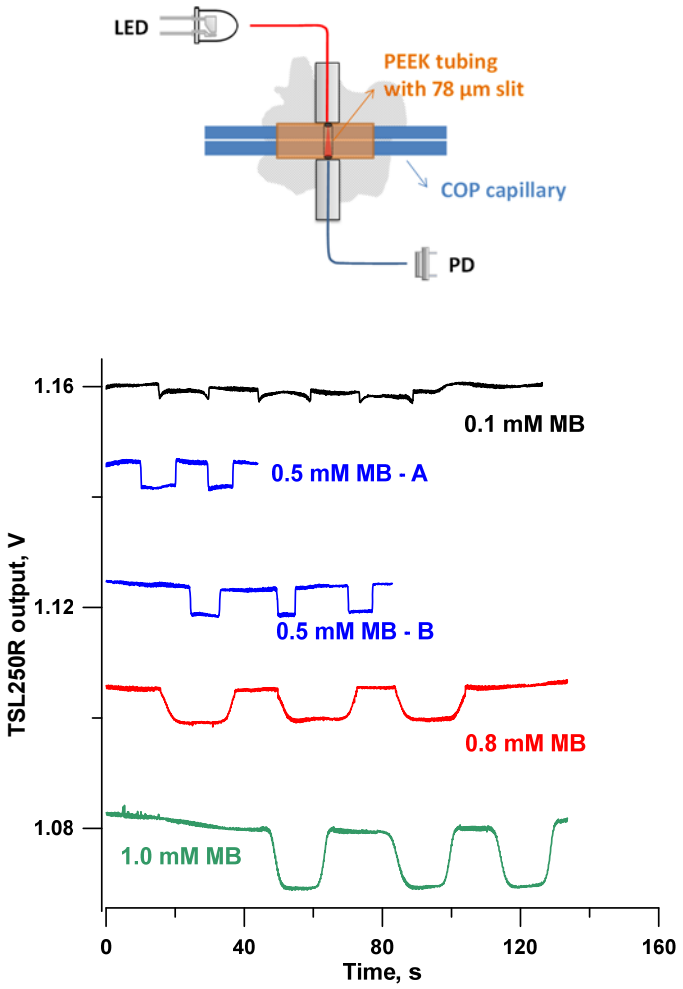

Figure 4- 7 Top: Transmittance-based interface detector for 28 μm i.d. 360 μm o.d. cyclic olefin polymer (COP) capillary. A PEEK sleeve that snug-fits the COP capillary is taken. Two opposite sides on its outside are filed flat. A 300 μm entrance hole allows light entrance from an LED. The opposite side is very carefully filed with the thin edge of a micro-file until light is observed. Microscopic measurement indicates a slit width of 78 μm. A lens-end, red-filter equipped photodiode with an integrated transimpedance amplifier (TSL257R, www.ams.com) reads the transmitted light. Bottom: response from multisegment trains containing aqueous methylene blue (MB) segments flanked by FC segments. Baseline values were offset for clarity.

The circuitry for admittance detection (more commonly and erroneously termed contactless conductivity detection (81)) has been previously described. (82) In the present version, square wave excitation (15 V) at a fixed frequency of 6.6 kHz (optimized for the present application) from an LMC555 timer was used and an ultralow bias current (3 fA) transimpedance amplifier (LMP7721, located next to the pick-up electrode) was used before RMS→DC conversion (AD 536), see Figure 4-8.

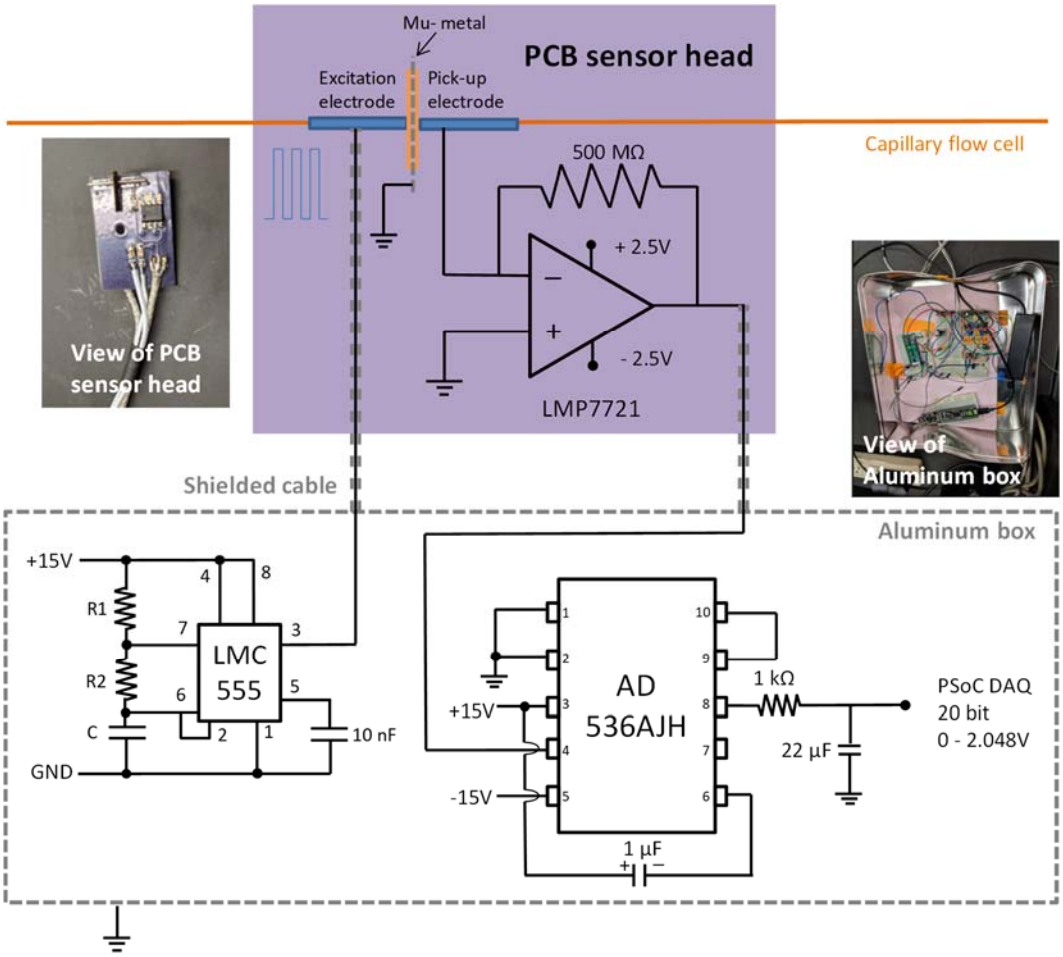

Figure 4- 8 Schematic of contactless admittance detector circuitry. Inset left: A picture of the sensor head. Inset right: A picture of the shielded aluminum box.

The sensor head comprises a 2.5×3.5 cm custom printed circuit board, containing the transimpedance amplifier (LMP7721; www.ti.com). On one short edge of the board are soldered two tubular stainless steel electrodes (380 µm ID; 685 µm OD; 6 mm in length), separated by a grounded isolation shield (mu metal, 6×6x 0.13 mm, insulated with adhesive-backed polyimide tape on either side). The amplifier was located immediately adjacent to the pick-up electrode on the sensor head to minimize noise. A 350 µm hole was drilled through the shield. The electrodes and the shield were aligned to insert the capillary flow cell and fixed in place and enclosed in a custom grounded enclosure. Excitation voltage, power and output signal were brought in and out of the board with shielded cables to a secondary grounded aluminum enclosure containing all the other circuit components. An LMC555 timer (www.ti.com) was used to generate rectangular wave excitation (15 V, 6.6 kHz, R_1 = 2.2 kΩ, R_2= 10 kΩ, C= 10 nF) The LMP7721 output was fed to an RMS-to-DC converter (AD536AJH, www.analogdevices.com) in the grounded aluminum box. The power supply for LMP7721 (± 2.5 V) was regulated down from the ± 15 V supply by LM317 and NTE957 voltage regulators, respectively. The signal output from the AD536 is via low-pass filter with a time constant of 22 ms. This is sampled by an analog-to-digital (ADC) converter in a programmable system on a chip (PSoC5LP, CY8CKIT-059. www.cypress.com).

4.2.5 Reference measurements

On either side of the admittance (or LED) detector based flow sensor, was the video microscopic flow measurement arrangement and the lowest flow rate (full scale 1500 nL/min) commercially available thermal mass flow sensor (MFS-1, www.elveflow.com). The measurement calibration of the microscope was verified with a

NIST-traceable graduated stage micrometer (10.0 μm reported by microscope as 9.99±0.05 μm, n=6). Flow rate was extracted from each Hg segment passage. Photoshop (www.adobe.com) was used to separate each video (30 frames/s, 600x800 pixels, actual field of view 13×17.5 mm) into time-stamped frames. For each microscopic reference measurement, two frames at least several s apart (depending on the flow rate), were randomly selected from a single Hg segment passage. The TOF was calculated from the time interval. The two frames were merged into a single image (Figure 4-9) and the distance coordinates computed by software (GrapherTM, www.goldensoftware.com), itself calibrated by the microscope-reported Hg segment length. The traversed distance was taken as the average of the distances respectively traveled by the leading edge and the trailing edge (the difference between these two numbers were statistically insignificant). The above process is tedious and subject to human judgment/error.

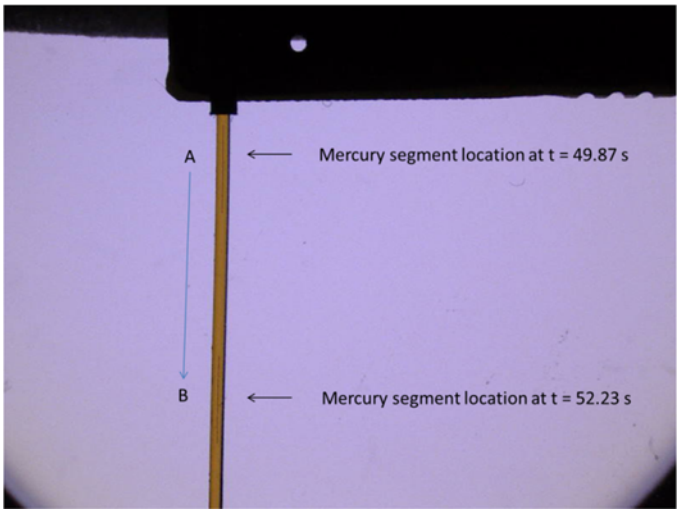

Figure 4- 9 Two frames of a video recording the downward motion of mercury segment was randomly selected and fused into a single picture. Mercury segment moved from location A to B during the time from t = 49.87 to t = 52.23 s.

Microscopic examination of several cross-sectional segments cut adjacent to our nominally 10 μm i.d. observation capillary provided a mean ± s.d. of 10.5 ± 0.1 μm (6 cross-sections, 18 measurements) for the capillary bore. The flow rates cited in this paper are based on this; the absolute accuracy is therefore also subject to the uncertainty from this source.

Readout electronics and a LabVIEW™ interface were developed in-house for the Elveflow sensor. The manufacturer's calibration equation was V_{out} = 1.4717 × F (μL/min) + 2.5. Our in-house calibration in the 0-1 μL/min range (gravimetrically measured, 10 min collection period) was in very good agreement (Figure 4-10).

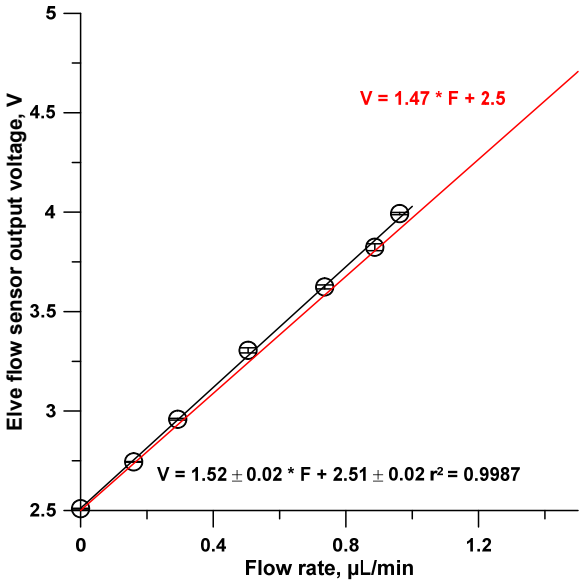

Figure 4- 10 Good agreement was observed between the manufacturer suggested calibration equation (Red trace) and observed response (Black trace) for the MFS1 flow sensor (www.elveflow.com) signal output relationship with the gravimetrically measured flow rate. The voltage output standard deviation is shown as the error bar at each flow rate. The calibration flow was generated pneumatically by a nitrogen pressurized reservoir controlled by a digital pressure regulator. Flow rates were measured by collecting the output into a tared 1.5 mL microcentrifuge tube for a minimum of 10 min. A 400 μm hole was drilled on the cap of the microcentrifuge tube to permit snug passage of the delivery capillary (o.d. 360 μm). To minimize evaporation loss, the tube was half-filled with water providing a water vapor saturated space.

4.2.6 Test arrangement

The test flow was pneumatically pumped by pressurized ultra-high purity grade N_2 via a high resolution digital pressure controller (P/N MM1PBNKKZP100PSG, www.proportionair.com, 6-100 psig,) from a custom-machined 25 mL capacity thick-wall Plexiglas reservoir (Figure 4-11). The generated flow entered an electrically actuated 2-position 4-port valve (Cheminert 03W-0030H, www.vici.com) configured to reverse the flow direction in the capillary observation tube with each valve actuation which took place after each complete crossing of the conductive marker past the sensor head.

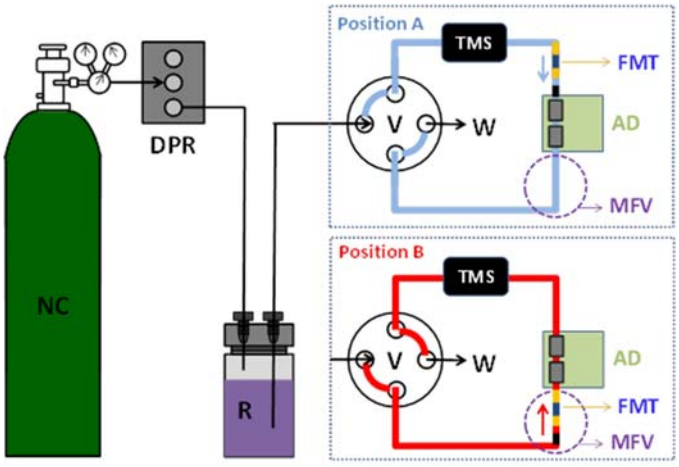

Figure 4- 11 Test setup: NC, N_2 cylinder; DPR, digital pressure regulator; R, pressurized reservoir (left port, pressure inlet; right port, liquid outlet) ; V four-port valve and its two positions; TMS Thermal mass flow sensor; FMT, flow marker train; AD, admittance detector; MFV, microscopic field of vision, W, waste. Arrows indicated flow directions in blue/red positions.

4.3 Results and discussion

4.3.1 A fluorocarbon marker

We focused first on a flow marker better than those thus far explored. Thermal and electrochemical pulses rapidly lose demarcation with time/distance due to diffusion/dissipation while gas bubbles dissolve (especially if the system is under

pressure) and change size with pressure and temperature. Gas bubble based TOF sensors cannot be realized at the high-pressure end of a chromatography system. Immiscible liquid markers (ILMs) seemed attractive and FCs suggested themselves as ideal ILMs because of the extremely low solubility FCs display in other liquids and vice-versa. FC-40 solubility in water and water solubility in FC-40 are <5 and <7 ppm w/w,(83) which are apparently the respective limits of detection of the methods used. The exact actual solubilities may be a lot lower. The inner conductive salt solution segment will rapidly saturate with FC and will not further change. The guard FC segment lengths are not measurands. Over prolonged use some loss may occur through solubilization. However, the majority of the tube is filled with the test fluid TF. Loss into the contiguous TF will occur very slowly both because of the extremely low FC solubility and the exponential decay of the FC concentration in the TF away from the FC interface. Convective mixing is hindered in small capillaries; FC levels in the TF build only via diffusion.

4.3.2 Initial experiments

We tested the feasibility of using FC ILMs and optically detecting them first in the macroscale. FC segments were introduced into TF flow (generated by a syringe pump at 5-500 μL/min) through a miniature tee at fixed intervals by a second syringe pump. Although FC-40 is non-toxic and does not pose a disposal issue, it is expensive and was recycled (Figure 4-6). Ideally, one would expect that being delivered by a precision syringe dispenser, the individual FC segment volumes will be highly constant. Surprisingly, this was not the case. If dispense volume was too small, depending on the TF flow rate, the FC did not leave the delivery tip at all. At high dispense volumes and at high TF flow rates, a single dispense resulted in multiple FC segments. Even at intermediate optimum dispense volumes, depending on the TF flow rate, the

reproducibility of individual FC segment lengths generated was poor: at a TF flow rate of 300 μL/min, an average 80 nL dispense had a relative standard deviation (RSD) exceeding 44% (n = 21). Even though the slug length varied so greatly, the TOF of the front edge, back edge and the center (average of the two) of each slug showed good reproducibilities: 1.78, 1.42, and 1.49 % RSD, respectively. Some of the residual imprecision came from the unoptimized signal pulse edge detection algorithm. The calibration data shown in Figure 4-12 indicate that this would make for a very acceptable TOF-based flow sensor in the 1 – 500 μL/min flow range.

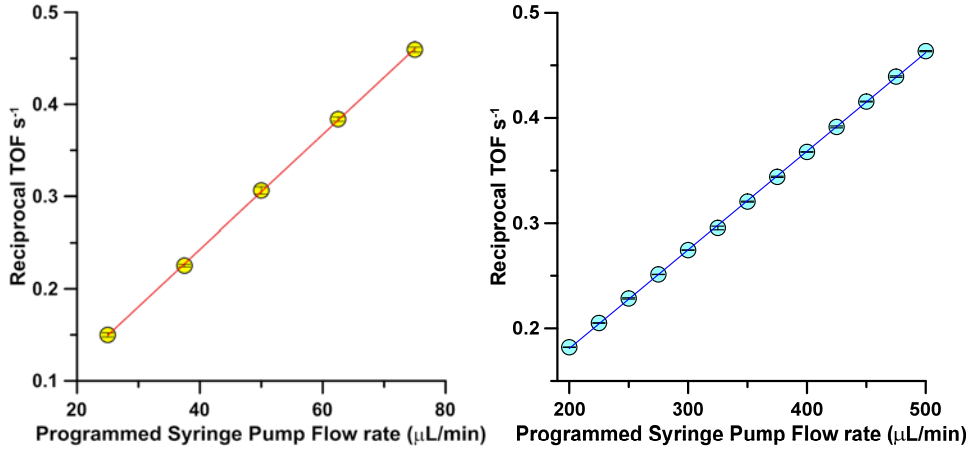

Figure 4- 12 Calibration data for the system of Figure 4-6. Tubes of different diameters were used to generate the two different plots. Flow rates down to 1 μL/min was measured using the same setup using an even smaller tube with good time resolution. Moving the second detector at fixed different distances from the first was also shown as a viable means to have high flow rate resolution without losing data update rate

However, the cost and complexity of the arrangement is significant given that other alternatives exist. This experiment confirmed the applicability of TOF flowmetry using FC markers but it required the TOF of a given interface is measured. It equally confirmed the poor precision/accuracy that would result if the TOS of an entire segment is the measurand, due to the poor reproducibility of individual segment lengths. To

accommodate TOS measurements, we had to reuse the same marker segments and therefore adopted the flow switching arrangement in Figure 4-11, designed to automatically reverse the flow when the marker of interest passed through.

To measure smaller flow rates using the same principle, we decreased the observation tube dimension by an order of magnitude to 28 μm i.d., using 10 μL syringes for FC delivery and a custom zero dead volume capillary tee. Even with the smallest optical slit we could make to reduce spatial stray light (see Figure 4-7), the fluorocarbon water-interface was not discernible. The detector could see the interface if the transmission through the aqueous phase was reduced by incorporating a dye (Figure 4-7). The large dye concentrations suggested the need for other approaches if the observation tube bore was to be further reduced.

Using a mercury segment flanked by FCs, we explored a reflective interface detection approach. Such a detector is very simple and inexpensive to construct as it requires no special optical aperture or slit arrangement. The initial trial clearly showed that a Hg-FC interface is easily detected even in the 11 μm i.d. capillary (Figure 4-13).

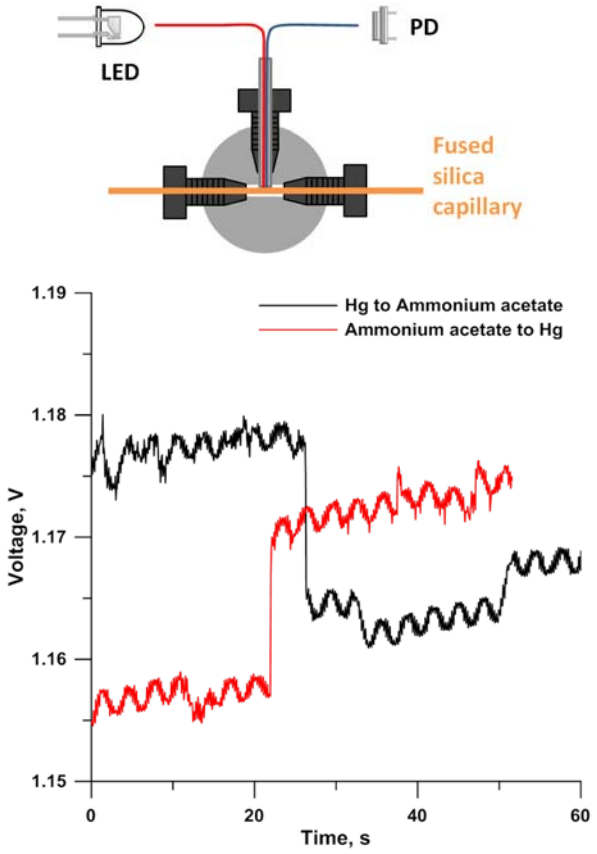

Figure 4- 13 Top: Reflectance based interface sensor. The reflection detector cell was constructed on a 1/16" PEEK tee. Fused silica capillary (10.5 µm i.d., 360 µm o.d.) was placed through the straight arm. Illuminating and sensing fiber optics (PMMA; 250 µm o.d.) conducting light from LED and to PD were fixed in the perpendicular arm on the same side, housed in a 1/16" o.d. 0.75 mm i.d. stainless steel sheath tube. Bottom: The reflectance signal goes from high to low when the Hg segment transitions into AA (black trace) and goes from low to high when the AA segment transitions into the Hg (red trace). No shielding was used in this initial trial experiment and the signal picked some low frequency (~0.3 Hz) periodic noise from some source as well as some abrupt baseline shifts. Regardless, it was clear that the arrangement is capable of detecting the interface passage.

Further contrast between light reflected by a metallic surface from light scattered by glass or Fresnel reflection would be possible by using a polarizing filter. However, aware of the current pariah status of mercury, we looked at potential alternatives. We

experimented with Galinstan, a Gallium-Indium-Tin alloy liquid at room temperature. It is well known that gallium and its alloys stain and adhere to glass, unfortunately a fluorosilylated capillary showed a different problem: the FC easily slipped past a Galinstan segment, often breaking it up (see Figure 4-14).

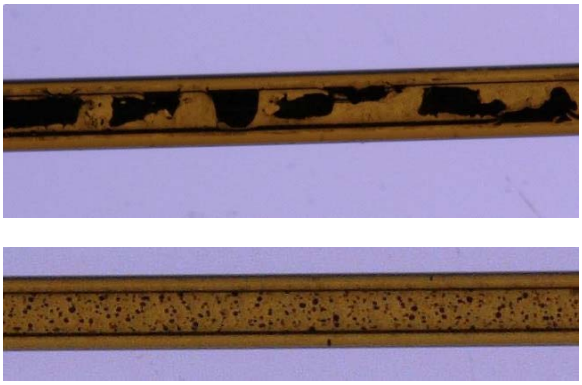

Figure 4- 14 Galinstan (a Ga-In-Sn alloy) is a liquid at room temperature. Top: A segment of liquid Galinstan that initially fully fills a fluorosilylated silica capillary breaks up into myriad pieces when pushed with a fluorocarbon because the fluorocarbon attaches to the wall and in a small capillary likes to fill it entirely. Bottom: With an untreated capillary, the Galinstan itself apparently finds active sites on the capillary wall and adheres to them. These photographs were taken with a 180 μm capillary for clarity.

We had prior experience in constructing simple on-tube admittance detectors and had demonstrated that they can pick up small changes in interior fluid composition even in capillaries as small as 2 μm in i.d.(84) This option was therefore pursued and all remaining results were based on the admittance detector. It is worthwhile to note that capacitance to voltage converters (e.g., AD7746, www.analogdevices.com), available inexpensively as complete evaluation boards, can also sense small changes in fluid composition within a tube. (85)

4.3.3 Admittance detector behavior for interface sensing

Consider two tubular electrodes in contact with the fluid, measuring conductivity in a conventional manner. We start with the gap between the electrodes filled with a

conductive fluid segment (the segment is longer than the gap, the electrodes are both in contact with the conductive segment) the output conductivity is high. An FC segment is pushing the conductive segment forward with a sharp interface. The moment that either electrode loses contact with the conductive segment, the conductivity will go to zero. One may thus expect to see an abrupt, digital-like transition as the interface passes through. In reality, the interface is curved and if the conductive fluid wets the electrode material preferentially, the conductive film on the entrance electrode will only be slowly removed by the FC front. During the last part of this transition then, effectively the electrode contact area will slowly decrease, making for a gradual and not abrupt change. In an admittance detector the field is capacitively coupled to the solution. Others have previously observed both experimentally and in simulation that the applied field extends beyond the electrode gap. (86) With two immiscible liquids when one has a much greater affinity for the tube surface and wets it, it will make for a lingering departure when the other liquid pushes it.

Consider an untreated hydrophilic capillary and the electrode gap (ca. 500 μm) is initially filled with a conductive aqueous liquid. This is being pushed by a 5 mm long FC segment, in the first case both the electrode pairs are 2 mm long. It does not matter which electrode side the FC segment enters from, referring to Figure 4-15, the black trace that depicts this situation indicates that the response is symmetric around the minimum. The two halves are identical, within limits of the electrodes being identical. Now let us make one of the electrodes 6 mm long (red/blue traces). The overall transition width is greater when the electrode length is increased, without increasing the gap. Also now there is a flow direction dependence. When the FC segment enters from the short electrode side (blue trace), the initial half of the response (the descent) is virtually the same as when both electrodes are short (black trace). If the exit electrode is short (red

trace), the second half of the response (the ascent) follows the black trace. Entrance/departure through the longer electrode makes for a longer descent/ascent, respectively.

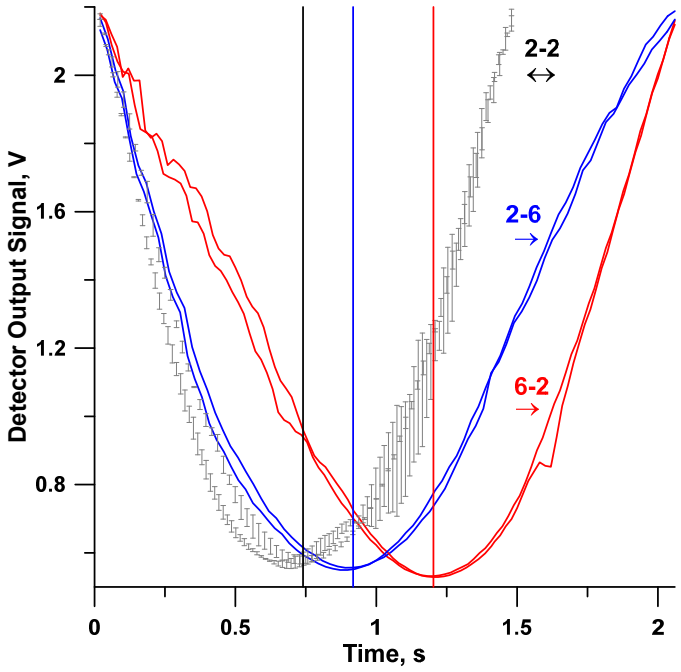

Figure 4- 15 A 5 mm FC segment is displacing an aqueous conductive segment initially in the electrode gap (~0.5 mm) of an admittance detector around a hydrophilic capillary. Black trace: error bars representing ± 1 standard deviation of the detector output for four separate runs (two each for flow from electrode A to B, both 2 mm long, and B to A). The perpendicular in each case is the line drawn through the minimum. The red and blue traces are both from a system where electrodes A (2 mm) and B (6 mm) are unequal in length. In the blue trace, the flow is from A to B and in the red trace the flow is from B to A.

The admittance detection approach was readily able to register the passage of an FC/AA interface even in a 5 μm i.d. capillary (Figure 4-16). This may be of future benefit to measure even lower flow rates, not presently pursued.

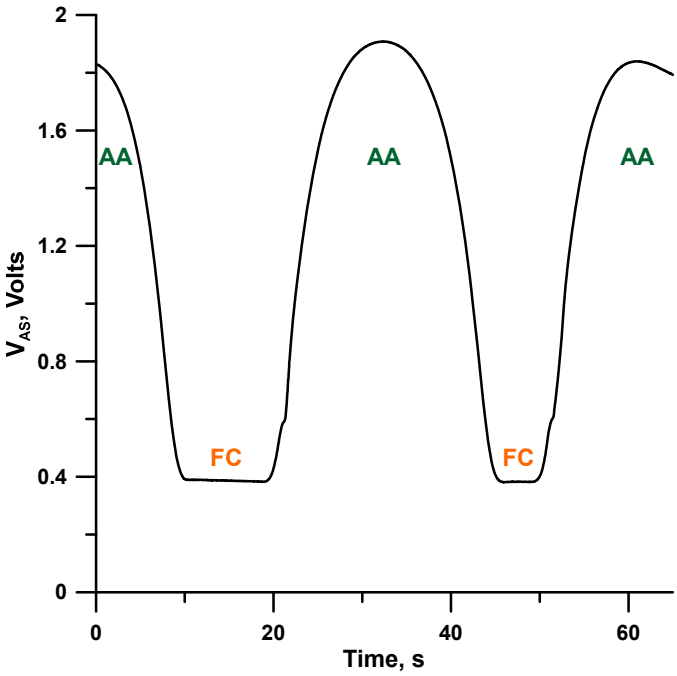

Figure 4- 16 Admittance detector traces for a FC (4 mm) – 50 mM ammonium acetate (4 mm) – FC (2 mm) segment in a 5 μm i.d. 360 μm o.d. fluorosilylated capillary. The test fluid in this case was also 50 mm ammonium acetate. Electrodes were 6 mm long.

4.3.4 Response behavior

The response behavior of the admittance sensor at low flow rates (approaching 1 nL/min) appears in Figure 4-17. Note that the lowest output values (baseline output) with the FC segments completely filling the gap are at ~0.2 V, close to but not at zero output voltage. The stability of the baseline is thus a true indication of the detector stability. However, such sensors respond nonlinearly with the solution conductance. Exponential behavior at the low conductance end has been discussed. (87) At high gain (presently used transimpedance gain 0.5 V/nA) and at higher conductivities, the detector approaches a plateau signal in an asymptotic fashion – the difference between the steady-state output from 0.5 mM or 50 mM NH4OAc (or for that matter a metallic

conductor like Hg) segment filling the detector is not proportional to their actual conductivities.

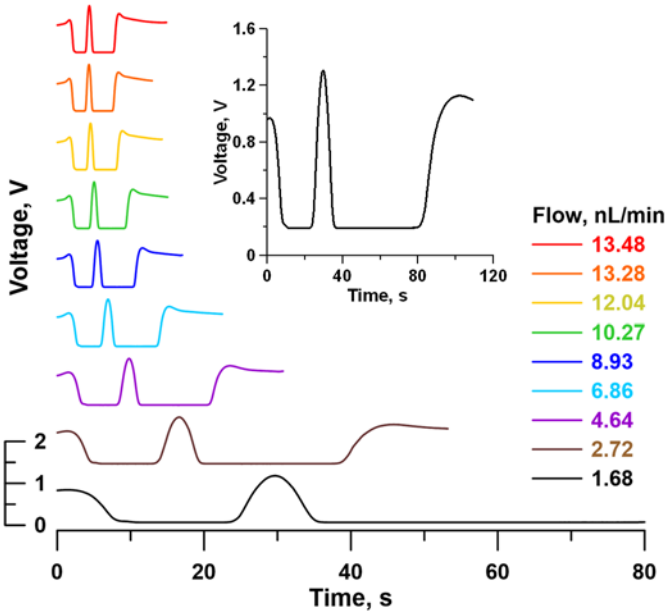

Figure 4- 17 The response of the admittance sensor to flow of the test fluid (0.5 mM ammonium acetate) from 1.68 to 13.48 nL/min. The electrodes are both 6 mm. The 10.5 μm i.d. capillary is fluorosilylated. The multisegment marker consists of a 50 mM ammonium acetate (~2 mm) "conductive" segment flanked by a ~5 and ~10 mm FC segment. The ordinate scale is shown for the lowest trace. The same scaling applies to all the traces but the baselines have been offset for clarity. The inset shows a replicate of the detector trace for the lowest flow rate.

4.3.5 Data analysis and strategies for interpretation

There are myriad possible approaches to relate the observed or derived parameters from the detector output to the microscopically observed flow rate. One of the more obvious parameters is the half width of the response peak elicited by the conductive segment. In reality, the measurand need not be the half-width, it can be the interval between any two chosen reference voltages on the ascending and descending parts of the response. There is no special significance to measuring the width at any specific

relative peak height, it is important to note that if the conductive segment is long enough, the response can be flat-topped (see Figure 4-18).

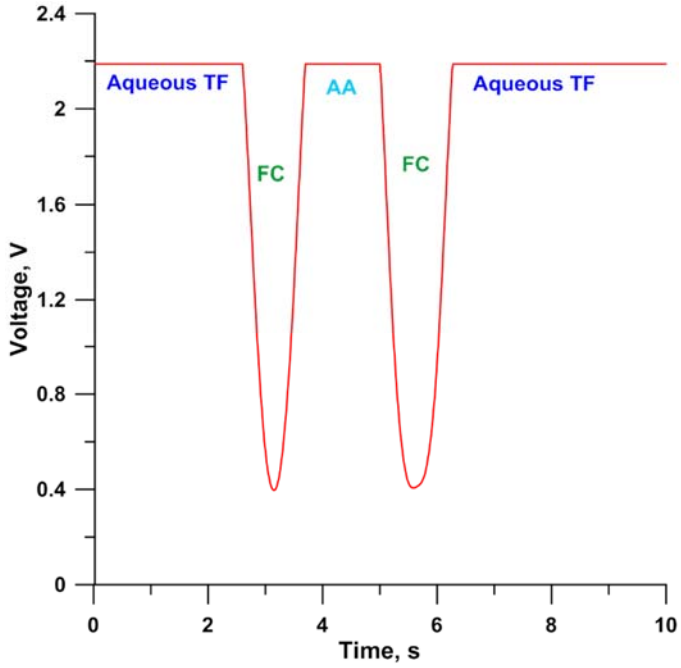

Figure 4- 18 The signal of elicited by a 50 mM ammonium acetate marker flanked by a 5 and 6 mm long FC segment. The test fluid in this case was also 50 mm ammonium acetate. Electrodes were 6 mm long.

Figure 4-19 shows the results for the width of the peaks in Figure 4-17 at 0.8 V (close to half-height, baseline and apex respectively being 0.2 and 1.3 V); it also shows data for the time for the signal to rise from 0.4 to 1.2 V as the measurand. Both approaches show comparable parameters of linearity and measurement uncertainty, but the latter takes less time and flow can be reversed without the entire marker having to pass through. Measurement can then be made on the descending signal.

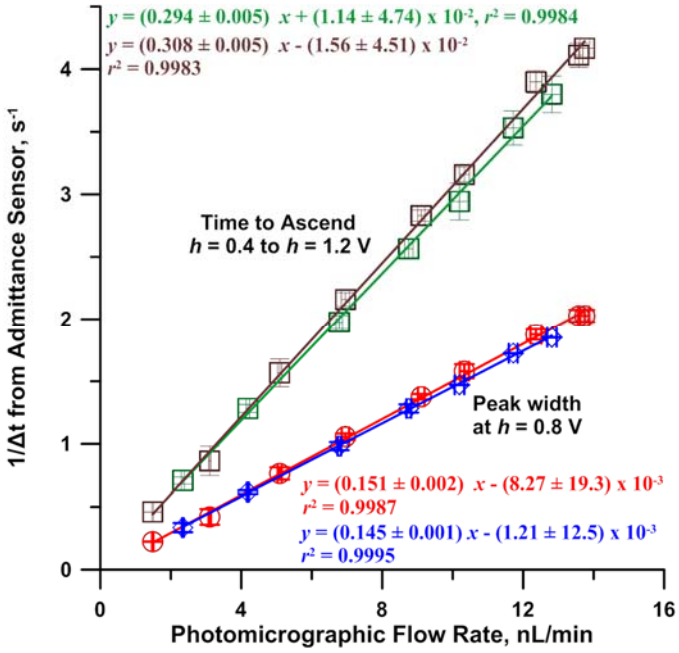

Figure 4- 19 Red and blue traces: peak width approximately at half-height, the two sets respectively depict up and down flows in a vertical sensor. Brown and green traces: similar data based on signal to rise from 0.4 - 1.2 V. Both x- and y- error bars indicate ±1 SD (n≥3). Lowest flow rate: 1.48 nL/min

We also studied the relationship of Δt between several randomly chosen signal values and the flow rate. While a linear relationship such as that in Figure 4-19 holds when these voltage points are relatively far apart, ln (Δt) - ln (flow rate) shows a more generally applicable linear relationship (Figure 4-20).

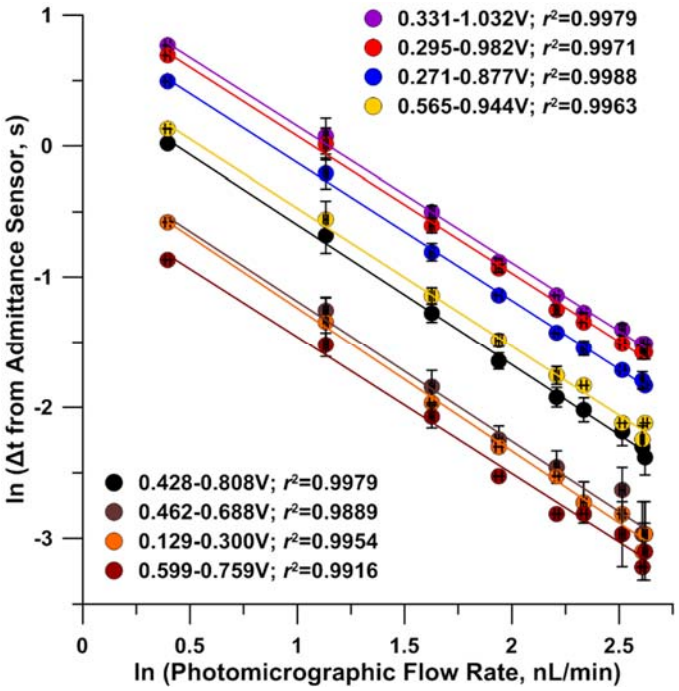

Figure 4- 20 A linear relationship exists between the logarithm of the (photomicrographically measured) flow rate and the logarithm of the time interval between several randomly chosen pair of signal voltages (indicated in the inset, along with the linear correlation coefficient, r^2).

Two other methods and associated calibration plots relating the flow rate to (a) the maximum, minimum and the amplitude of the derivative of the admittance sensor output (dV/dt) and (b) regional temporal slope of the sensor signal based on a moving window and their relative merits are discussed. Figure 4-21 depicts the several modes of data interpretation/calibration we attempted.

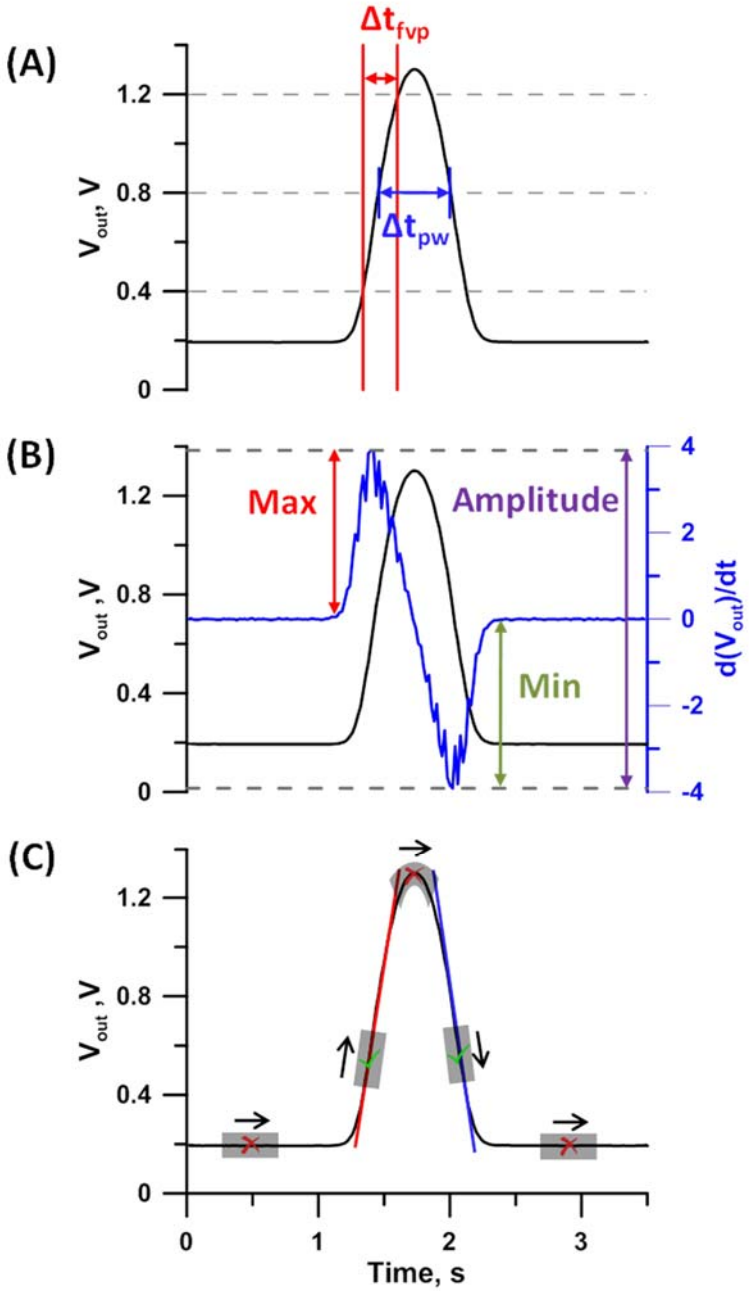

Figure 4- 21 Different modes of data interpretation.

4.3.5.1 Time interval approaches

This approach, summarized in panel A of Figure 4-21, was used in the illustration in Figure 4-19. The measurement of peak width (Δt_{pw}) at 0.8 V was used therein (red and blue traces), others at arbitrarily chosen points in the admittance response produce similar results. The second approach, also depicted in panel A above, is to measure the time interval on either the ascending or descending part of the admittance response between two arbitrarily chosen fixed voltage points (Δt_{fvp}) as illustrated by the brown and green traces in Figure 4-19 and for a multitude of arbitrarily chosen fixed voltage points in Figure 4-20.

4.3.5.2 Derivative-based approaches

Taking the derivative of the sensor output can eliminate effects of signal drift,(20) but it does increase noise. Either the maximum or the minimum dV/dt value (or the difference between the two (referred to as the amplitude here) all exhibited a linear relationship with the flow rate (Figure 4-22, 4-23, and 4-24). In addition, the precision of any of the three measurands has no obvious dependence on the flow rate, meaning that the attainable flow rate resolution is not flow rate dependent. No significant differences in performance are observable in choosing the maximum vs. the minimum as the measurand, either edge can be used equally well. This is convenient as they will alternately appear as flow direction is switched. Using amplitude requires both the maximum and the minimum and thus double the time but amplitude as a measurand is automatically feasible with data immediately before after flow switching. Derivative-based measurands require more time than measuring Δt_{fvp} but may provide a greater measurement range if we limit ourselves to a single marker segment.

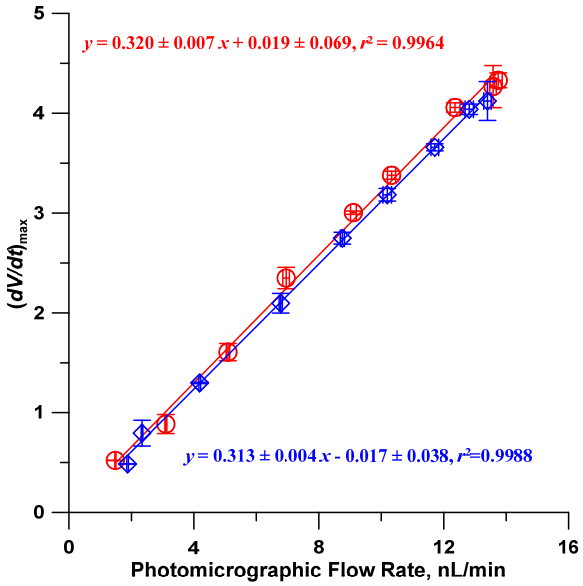

Figure 4- 22 Maximum value of admittance signal derivative as a function of microscopically measured flow rate value. Statistically, there is no dependence of the slope on the direction of movement and the intercepts are not distinguishable from zero. x- and y- error bars both indicate ± 1 standard deviation.

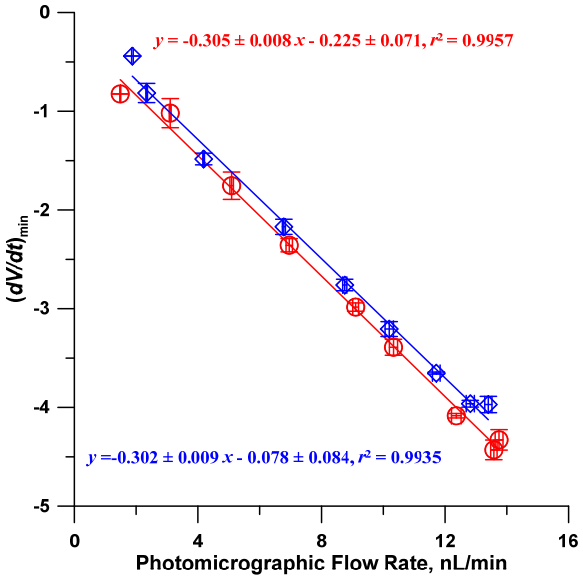

Figure 4- 23 Minimum value of admittance signal derivative as a function of microscopically measured flow rate value. Statistically, there is no dependence of the slope on the direction of movement. x- and y- error bars both indicate ± 1 standard deviation.

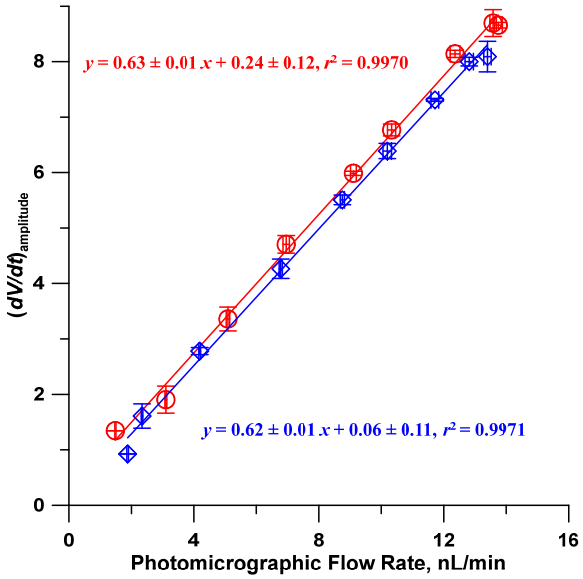

Figure 4- 24 The amplitude of the admittance signal derivative as a function of microscopically measured flow rate value. Statistically, there is no dependence of the slope on the direction of movement and the intercepts are not distinguishable from zero. x- and y- error bars both indicate ± 1 standard deviation.

4.3.5.3 Regional slopes in a moving window

This approach takes advantage of the fact except for the initial and the end part of either the ascending or descending portion of an interface crossing event; the majority middle section is well described by a straight line whose slope is linearly related to the flow rate. To take advantage of this, the following algorithm can be executed in real-time: The admittance detector output voltages are examined by a linear regression, taking n (presently, data were collected at 50 Hz for this experiment and n = 10 was used) successive data points at a time and then moving over by 1 datum and repeating the process. The slope given by the data set will qualify to produces an acceptable flow rate provided it meets all of the following criteria: (1) linear r^2 >0.9990; (2) root mean square error (RMSE) of prediction less than some arbitrarily chosen value (presently taken to be 5 mV), (3) the slope is above some minimum value which excludes the baseline (in reality

the baseline typically fails one or both of the first two tests because of the presence of noise and the lack of a consistent slope). Figure 4-25 and 4-26 show the results.

In Figure 4-21C, only the part of the data on the response curve that fall on the red or blue superimposed straight lines are qualified by the algorithm. This approach does very well at the low flow rate end. As flow rate increases, the interface moves through quicker, the number of data points belonging to the linear region decreases, as do the qualifying sub-sets. The number of qualifying sub-sets at flow rates of 1.5, 3.1, 5.1, 6.9, 9.1, and >10.3 nL/min and a data rate of 50 Hz were 61, 29, 8, 4, 4 and 0, respectively. The applicable range will doubtless increase at a greater data rate, although some penalty may have to be paid because of the increased noise. Under the present conditions that were chosen, the upper flow rate limit was then ~9 nL/min by this approach. There was no significant performance difference operating between the ascending and descending sides of the signal.

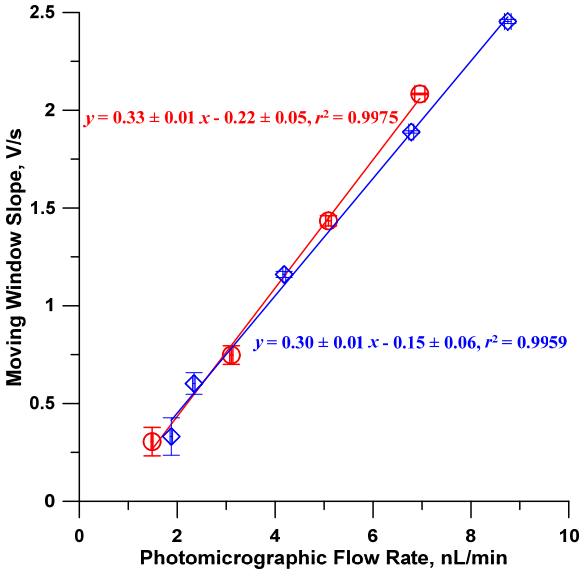

Figure 4- 25 Moving window (n=10 @50 Hz data rate) slope (ascending part of response) as a function of the flowrate. x- and y- error bars both indicate ± 1 standard deviation.

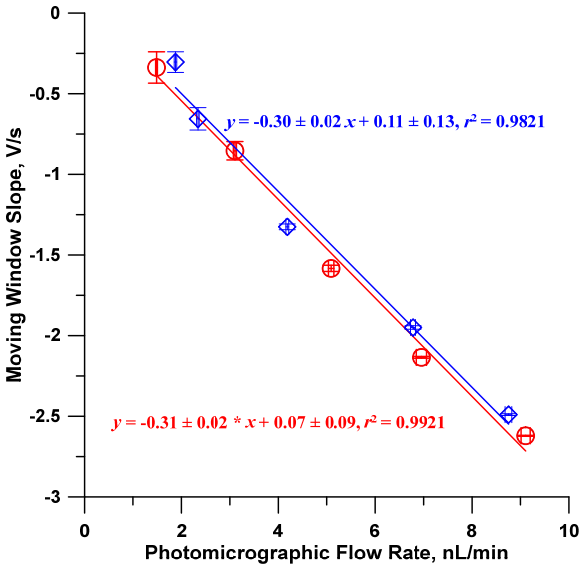

Figure 4- 26 Moving window (n=10 @50 Hz data rate) slope (descending part of response) as a function of the flow rate. Statistically, there is no dependence of the slope on the direction of movement and the intercepts are not distinguishable from zero. x- and y- error bars both indicate ± 1 standard deviation.

Table 4-1 summarizes the performance parameters of the above approaches

Table 4- 1 Performance Comparison of Different Parameters as Measurands

Measurand	% RSD	Sensitivity[b]	Resolution, nL/min	Minimum Update Interval,[c] s	Measurement range, nL/min
$\Delta t_{pw,0.8V}$	2.0-13%	0.308	0.3-0.8	3	1.5-13.7
Δt_{fvp}	1.6-15%	0.151	0.3-0.8	6	1.5-13.7
dV/dt maximum	0.6-11%	0.320	0.1-1.3	3	1.5-13.7
dV/dt minimum	0.6-15%	-0.305	0.1-1.0	3	1.5-13.7
dV/dt amplitude	0.6-13%	0.625	0.1-0.8	6	1.5-13.7
Moving Window, Ascending Slope	0.1-24%[a]	0.328	0.02-0.4	0.1	1.5-9.1
Moving Window, Descending Slope	0.1-29%[a]	-0.306	0.02-0.7	0.1	1.5-9.1

[a] Because of decreasing slope, uncertainty increases with decreasing flow rate in successive measurements. A change in criterion, e.g., a tighter specification on r^2 or the relative uncertainty of the slope, can reduce this.

[b] Units: measurand units /(nL/min)

[c] Based on a flow rate of 3 nL/min and highest practical frequency of flow switching. However, every time flow is switched, an additional 1-2 s may be needed for stabilization.

4.3.6 Response time

We wanted to determine how fast the sensor will respond to changes in flow. The time to perceive such a change depends on the method of interpretation and when in the measurement cycle the change occurs. The favored arrangement at low flow rates is repeated back and forth scanning of the interface. Figure 4-27 shows that any flow change during such an event can be observed in a sub-second time scale.

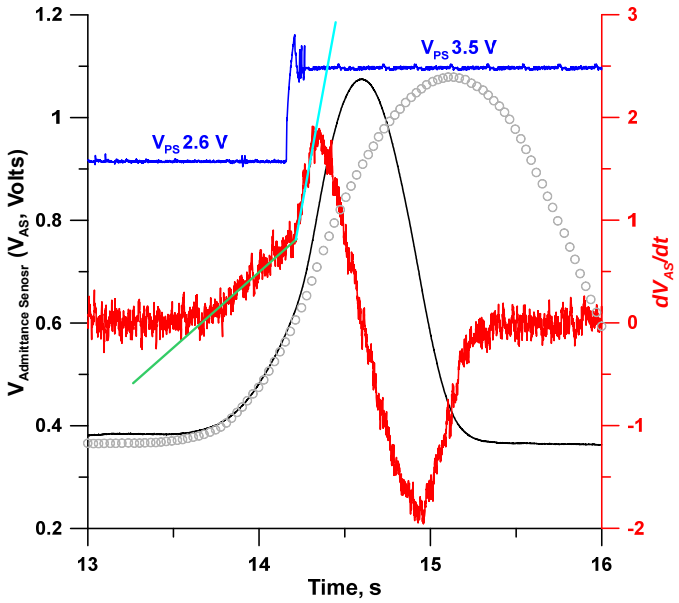

Figure 4- 27 Sensor response speed based on data rate of 1 kHz. During the passage of the marker interface, the pneumatic pressure on the delivery reservoir was abruptly changed (t = 14.16 s). Based on the pressure sensor output (V_{PS}, blue trace), the pressure changed in ~40 ms and stabilized in ~120 ms. The solid black line depicts the admittance signal. The hollow symbols depict an experiment where V_{PS} remained constant at 2.6 V. The red trace is the derivative of the admittance signal (20 points moving average applied). Note that the slope observably changes within 100 ms of V_{PS} change.

The change in the slope is more readily apparent in a second derivative plot (Figure 4-28). Repeat experiments that involve stepping up or down in flow indicate no difference in the lag period if the flow is increased or decreased. The difference of the lag

time on flow direction, 76 ± 46 vs. 49 ± 21 ms was not statistically significant either and small differences in electrode lengths on each side may play a role (see Table 4-2).

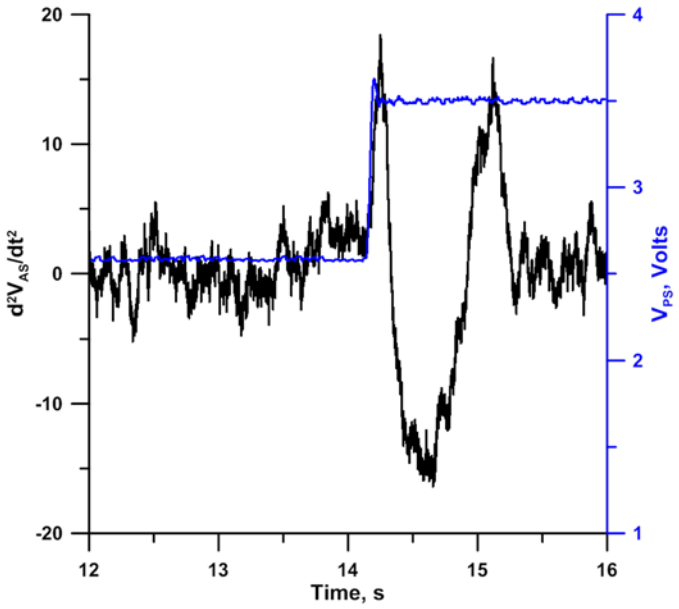

Figure 4- 28 The second derivative of V_{AS} as a function of time. Blue Trace: Pressure sensor output, V_{PS}, right ordinate, showing that it changed from 2.6 to 3.5 V at 14.15 s. The second derivative of the admittance sensor output in the black trace shows the slope transition ca. 100 ms later

Table 4- 2 Lag times for Detection of Flow Change

	Control Signal Step Time, s	Time Slope Change is Detectable, s	Time Lag for Detection of Flow Change, s	Average Lag Time, s	Standard Deviation, s	
Flow Direction Down, Pressure Control Signal stepped from 2.7 to 3.7 V, Flow Increasing						
Trial 1	14.162	14.205	0.043			
Trial 2	41.366	41.401	0.035	0.051	0.022	
Trial 3	67.577	67.653	0.076			
Flow Direction Down, Pressure Control Signal stepped from 3.7 to 2.7 V, Flow Decreasing						
Trial 1	10.147	10.180	0.034			
Trial 2	48.805	48.837	0.032	0.048	0.026	
Trial 3	69.550	69.627	0.077			
Flow Direction Up, Pressure Control Signal stepped from 2.7 to 3.7 V, Flow Increasing						
Trial 1	12.715	12.759	0.043			
Trial 2	32.744	32.871	0.127	0.076	0.044	
Trial 3	51.644	51.703	0.059			
Flow Direction Up, Pressure Control Signal stepped from 3.7 to 2.7 V, Flow Decreasing						
Trial 1	49.943	49.982	0.039			
Trial 2	71.624	71.671	0.047	0.076	0.058	
Trial 3	91.805	91.948	0.142			
			Average, s	**(all data)**		**0.063**
			Standard Deviation, s			**0.037**

The overall lag time to detect a change in flow was around 65 ms.

The direction of the flow marker motion or the decrease/increase in the flow rate had no influence on the response time.

4.3.7 Effect of temperature

Compared to thermal expansion coefficient of liquids (for example, water around 25 °C is ~2.5 x 10^{-4}/°C), that for fused silica is far smaller (~5 x 10^{-7}/°C). Calibration shift because of a change in i.d. due to a 10 °C change will be negligible. In fact, the change in the volume of water for that degree of temperature change will be 0.25%, barely detectable in the present system. Our purpose in studying the effect of temperature was more to ascertain if some other fundamental behavior changes or the electronics is

affected that ultimately affects sensor output. As Figure 4-29 indicates, there does not appear to be any such effect. Figures 4-30 and 4-31 use a different set of measurands and also indicate the same.

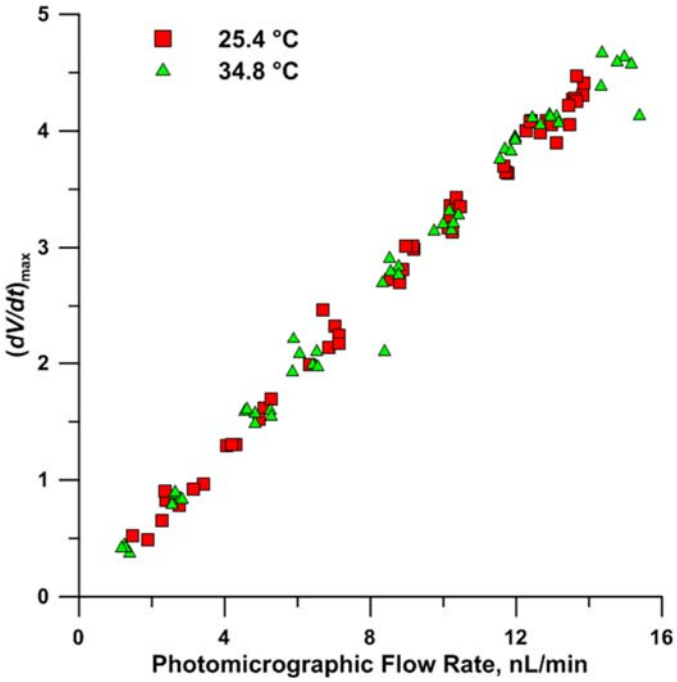

Figure 4- 29 A 10 degrees change in temperature has no discernible systematic effect on the system behavior as judged by the admittance signal first derivative maximum. The flow rate range is 1.25-15 nL/min.

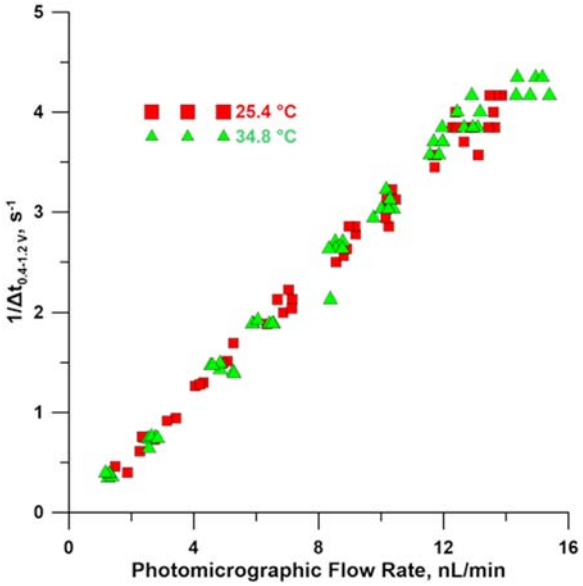

Figure 4- 30 A 10 degrees change in temperature has no discernible systematic effect on the system behavior as judged by the time interval for the admittance signal to go from 0.4 to 1.2 Volts on the ascending part of the curve. The flow rate range is 1.25-15 nL/min.

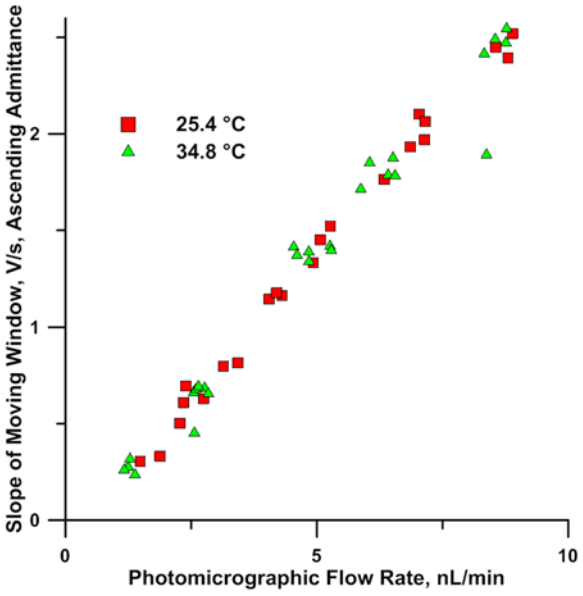

Figure 4- 31 A 10 degrees change in temperature has no discernible systematic effect on the system behavior as judged by the ascending moving window slope. The flow rate range is 1.25-8.0 nL/min.

4.4 Conclusions

We provide a relatively simple, inexpensive and robust sensor for measuring flow rates in the low nL/min range. It appears to be easily extendable to even lower flow rates. In this paper, we have focused on the TOS of a small ILM segment or the (partial) passage of an interface between two liquids through the vision horizon of the detector to measure low flow rates. Extension to a much larger flow rate range using TOS measurement that range from of passages of interfaces to that of a given segment multiple marker segments is rather obvious; experimental demonstration will be provided in a forthcoming paper. The limiting factor in the absolute accuracy of the method remains in the measurement and the uniformity of the diameter/cross-section of the relevant region observation conduit.

Appendix A

PSoC and LabVIEW program for hydrocephalus flow monitor

A.1 PSoC program for hydrocephalus flow monitor

A.1.1 Introduction

Programmable System-on-Chip (PSoC®) is a family of microcontroller integrated circuits by Cypress Semiconductor. These chips integrate a CPU core, memory, programmable and reconfigurable analog and digital peripherals, providing customizable functions for a wide range of embedded applications at a low cost. It combines programmable and reconfigurable analog and digital blocks, delivering a complete system solution for a wide range of embedded applications at a low cost.

A.1.2 Top design

The top design schematic of the project is shown in Figure A-1.

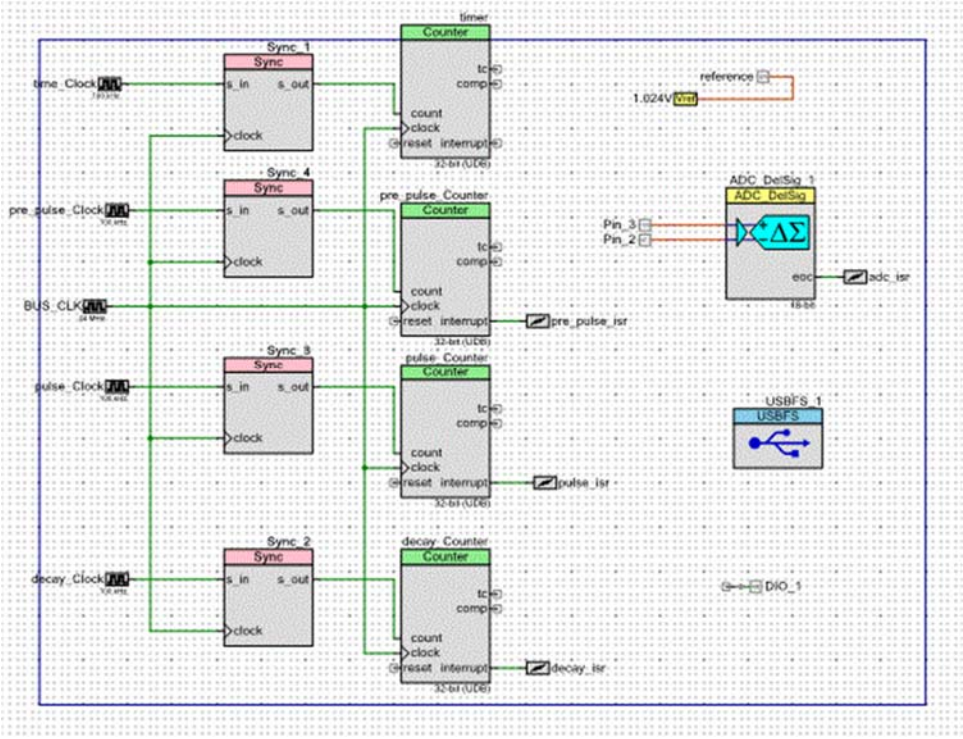

Figure A- 1 The top design schematic of the project.

The quantities of on-chip components and their key configurations are given below,

5×Clocks (Time_Clock, 100 kHz; Pre_Pulse Clock, 100 kHz; BUS_CLK, 24 MHz; Pulse_Clock, 100 kHz; Decay Clock, 100 kHz)

4×Syncs

4×Counters (Timer; Pre_Pulse_Counter; Pulse_Counter; Decay_Counter; all 32 bits)

1×Voltage Reference (Vref = 1.024V)

1×Delta Sigma Analog to Digital Converter (ADC_DelSig_1, Resolution 18 bits; Input range: ±2.048V; Input Mode: Differential)

1×full speed USB (USBFS_1)

4×Analog pins (2 for analog input, 1 for voltage reference output)

1×DIO pin (DIO_1)

BUS_CLK is the main clock source. The other four internal clock signals are synchronized with BUS_CLK by sync components. These four clocks are paired with four counters to control timing.

The first pair (sync_1 and timer shown in Figure S4) drives the conversion of signals from analog to digital in ADC_DelSig_1, logging time for each voltage data points. The other three pairs keep track of the timing during one measurement loop (5s of sensing, 5 s of heating and 20 s of sensing). When the signal “Measurement start” from LabVIEW is received by PSoC, Pre_pulse_counter starts counting. DIO outputs LOW (sensing mode). After 5 s, Pre_pulse_counter stops, resets, triggers the subsequent pulse_counter starts counting. DIO outputs HIGH (heating mode). After 5 s, pulse_counter stops, resets, triggers the subsequent delay_counter starts counting. DIO

outputs LOW (sensing mode). After 20 s, the pre_pulse counter is triggered again to initiate other another measurement loop. This result in automated measurements every 30 s until the “measurement end” signal received. If required, one-time trigger initialized by user could be achieved with mild modification to current program.

A.1.3 Main C file

```
#include <device.h>
#include <stdio.h>

#define IN_EP       (0x01u)
#define OUT_EP      (0x02u)

#if defined (__GNUC__)
    asm (".global _printf_float");
#endif

union int_thing1 {
    uint8 usb_in[4];
    int32 usb_in32;
};

union int_thing1 usb_in;

union int_thing {
    uint8 usb_data[4];
    int32 number;
};

union int_thing number;

union int_thing2 {
        uint8 sar_adc_out[2];
        int sar_adc_in;
};

union int_thing2 adc_out;

int32 output;
uint8 aout_1;
uint8 dout_1;
int dio_pin;
int dio_read;
int clk_div;
uint8 results[64];
```

```
int adc_Loop = 0;
int i;
int registerClear;

int trigger;

CY_ISR(adc_irq)
{
   adc_isr_ClearPending();
   if(adc_Loop < 8)
   {
      number.number = timer_ReadCounter();
      for(i = 0; i < 4; i++)
      {
         results[i+8*adc_Loop] = number.usb_data[i];
      }
      number.number = ADC_DelSig_1_GetResult32();
      for(i = 0; i < 4; i++)
      {
         results[i+8*adc_Loop+4] = number.usb_data[i];
      }

      adc_Loop++;

      if(adc_Loop == 8)
      {
         results[63] = 0b01111111;
         results[55] = 0b01111111;
         results[47] = 0b01111111;
         results[39] = 0b01111111;
         results[31] = 0b01111111;
         results[23] = 0b01111111;
         results[15] = 0b01111111;
         results[7] = 0b01111111;
         adc_Loop = 0;
         USBFS_1_LoadInEP(IN_EP, results, 64);

      }

   }

}

CY_ISR(pre_pulse_irq)
{

   registerClear = pre_pulse_Counter_ReadStatusRegister();
   if(trigger == 1)
   {
```

```
        DIO_1_Write(1);
        pre_pulse_Clock_Stop();
        pre_pulse_Counter_WriteCounter(0);
        pulse_Clock_Start();
    }
}

CY_ISR(pulse_irq)
{

    registerClear = pulse_Counter_ReadStatusRegister();
    if(trigger == 1)
    {

        DIO_1_Write(0);
        pulse_Clock_Stop();
        pulse_Counter_WriteCounter(0);
        decay_Clock_Start();
    }
}

CY_ISR(decay_irq)
{

    registerClear = decay_Counter_ReadStatusRegister();
    if(trigger == 1)
    {
        decay_Clock_Stop();
        decay_Counter_WriteCounter(0);
        timer_WriteCounter(0);
        pre_pulse_Clock_Start();

    }
}


void USB_check(){
    if(USBFS_1_GetEPState(OUT_EP) == USBFS_1_OUT_BUFFER_FULL)
        {
            USBFS_1_ReadOutEP(OUT_EP, usb_in.usb_in, 4);

            if(usb_in.usb_in32 == 1000)
            {
                ADC_DelSig_1_StartConvert();
                timer_WriteCounter(0);
                time_Clock_Start();
            }


            if(usb_in.usb_in32 == 2000)
```

```
        {
            timer_WriteCounter(0);
            DIO_1_Write(0);
            pre_pulse_Clock_Start();
            trigger = 1;
        }

        if(usb_in.usb_in32 == 3000)
        {
            trigger = 0;
            pre_pulse_Clock_Stop();
            pulse_Clock_Stop();
            decay_Clock_Stop();
            DIO_1_Write(0);
        }

    }
}


void main()
{
    CyGlobalIntEnable;

    USBFS_1_Start(0u, USBFS_1_5V_OPERATION);

        while(!USBFS_1_GetConfiguration());

    USBFS_1_EnableOutEP(OUT_EP);
    adc_isr_StartEx(adc_irq);
    pre_pulse_isr_StartEx(pre_pulse_irq);
    pulse_isr_StartEx(pulse_irq);
    decay_isr_StartEx(decay_irq);
    timer_Start();
    timer_WriteCounter(0);
    pre_pulse_Clock_Start();
    pre_pulse_Counter_Start();
    pulse_Counter_Start();
    decay_Counter_Start();
    ADC_DelSig_1_Start();


    while(1)
    {
        if (USBFS_1_IsConfigurationChanged())
            USBFS_1_EnableOutEP(OUT_EP);
        USB_check();
    }
}
```

A.2 LabVIEW program for hydrocephalus flow monitor

A LabVIEW program was developed for instrument control, data acquisition, data manipulating and signal processing. The front panel and block diagram, of hydrocephalus flow meter VI, are shown in figure A-2 and A-3, respectively.

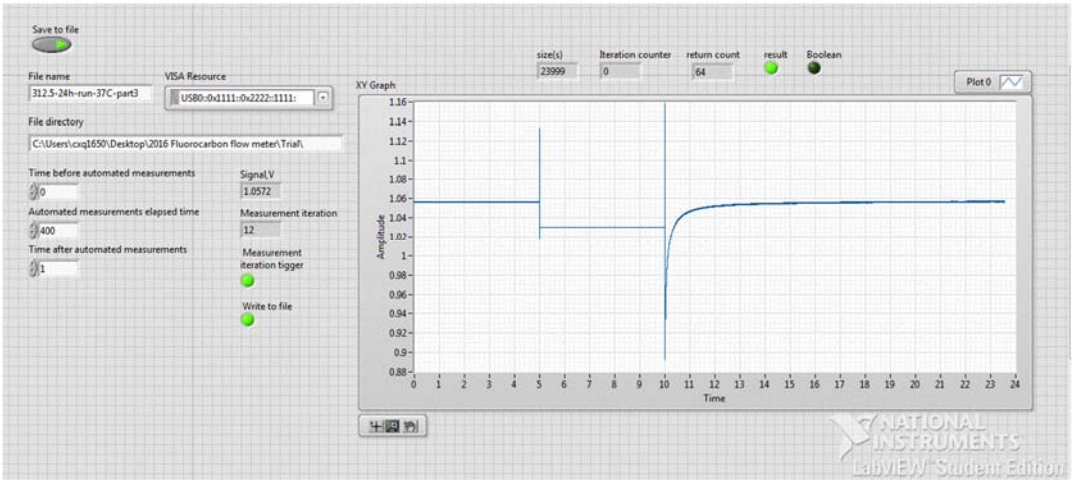

Figure A- 2 The front panel of hydrocephalus flow meter VI

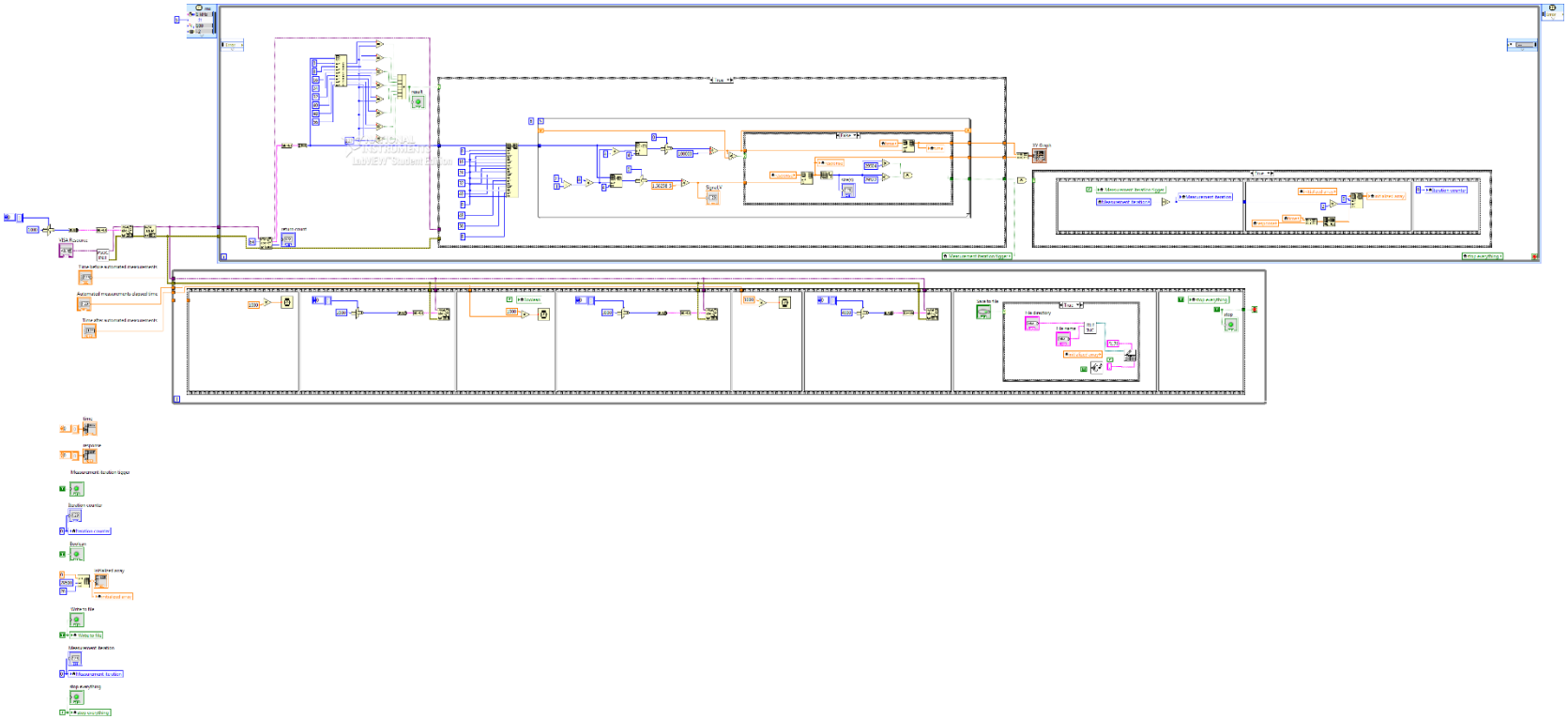

Figure A- 3 The block diagram of hydrocephalus flow meter VI

There are four case structures in the LabVIEW program. Their complete diagram (including the hidden cases that are not showing in Figure A-3) and their function are shown and discussed below.

The case structure shown in figure A-4 is governed by a Boolean control which is determined by the upstream program. If there is no data missing during transfer (true case), binary data from PSoC will be converted to time and voltage (Figure A-4a). Otherwise (false case), the USB pocket will be discarded (Figure A-4b).

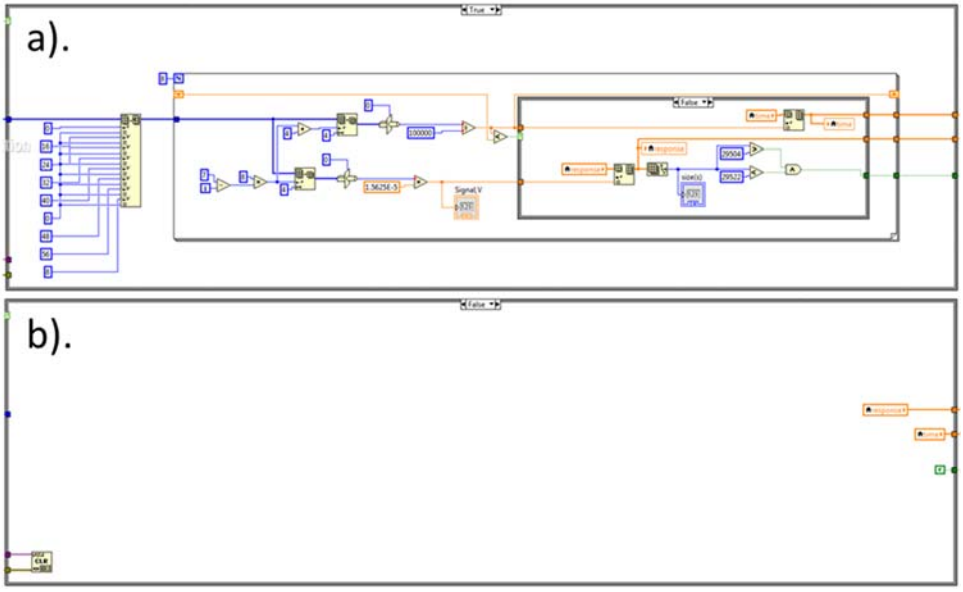

Figure A- 4 Case structure discards pockets with data missing. a). true case; b). false case

The purpose of the case structure shown in Figure A-5 is to re-organize the data. In the case structure, the data of different measurement cycles which were in concatenation would be separated and listed in different columns. This facilitates the following data analysis. The strategy to identify the start of a new measurement cycle is to monitor the timestamp for each V_{fs} (the voltage outputs of hydrocephalus flow sensor) since the timestamp is re-zeroed at the beginning of each measurement circle. When the

newly logged time is larger than its previous logged time (false case) which indicates the continuing of a measurement cycle, data will be saved to the next row but into the same column (Figure A-5b). Otherwise (true case), data will be saved into the next column (Measurement iteration +1). Meanwhile, front panel XY graph would be wiped out, preparing for plotting the next measurement (Figure A-5a).

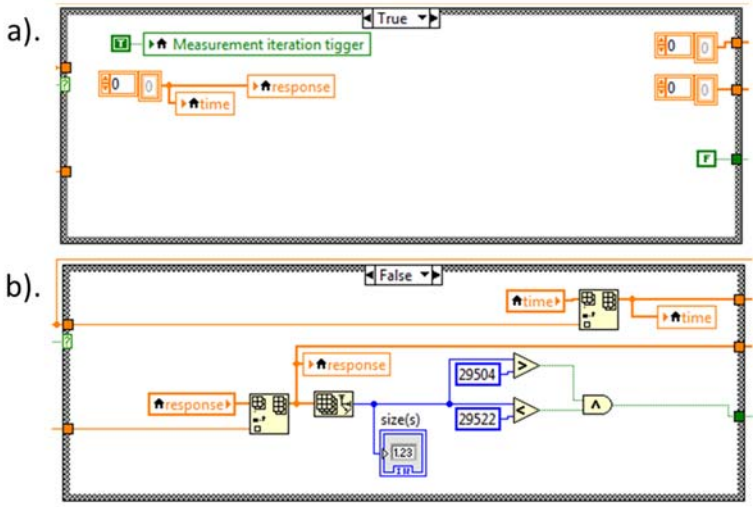

Figure A- 5 The case structure assigns different measurement cycles to different columns. a). true case; b). false case

The case structure shown in Figure A-6 is used along with a Boolean variable which guarantees data only be saved once into the array.

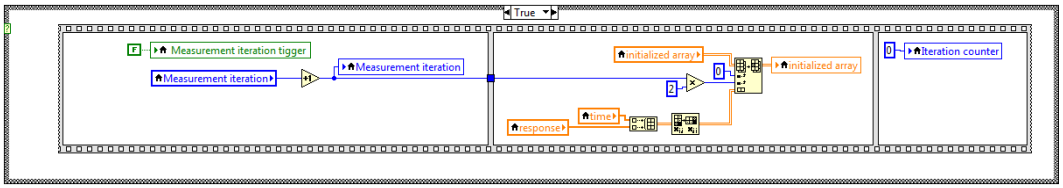

Figure A- 6 The case structure guarantees single data saving. The figure only shows the true case, the false case is not shown since it is empty in content.

The case structure shown in Figure A-7 is controlled by user input. If true, data stored in an array will be written into an excel file. The false case is empty in content.

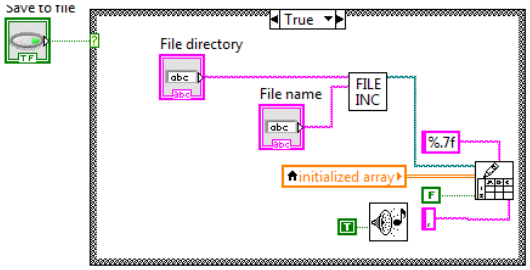

Figure A- 7 The case structure writes data into a spreadsheet.

Appendix B

Attenuation coefficients of tubular conduits for liquid phase absorbance measurement.

Shot noise-limited Optimum pathlength.

B.1 Introduction

Cell path lengths in used in liquid phase absorbance measurement have increased dramatically over past decades, especially since Liquid Core Waveguides (LCWs) were introduced. Stone(88) pioneered tetrachloroethylene-filled quartz tubes for low-loss optical communication and later reported intense Raman emission from benzene-filled fused silica capillaries (FSCs) (89) and coined the term “Liquid Core Optical Fiber” (LCOF). A decade later, having already explored multi-reflection/multi-pass approaches, Fuwa and his students began studying absorbance measurements in long capillaries. They looked at tubing material, dimensions, exterior reflectivity, coil radius of a coiled tube etc. They improved the limit of detection (LOD), e.g., in determining phosphorous as molybdenum blue by using 1-m straight glass capillaries with a reflective external Al coating. (90) This transmitted 10,000x greater light relative to a stainless steel tube of the same i.d. (ϕ). The effective path lengths of such cells increased with decreasing absorptivity of the medium, later understood as the multipath effect. (91) Light transmission greatly improved with CS_2 (refractive index (RI) at 589 nm, hereinafter n_{589}, 1.62; RI for liquids do not vary markedly with wavelength) in a borosilicate glass (n_{589} 1.47) tube. This condition ($RI_{liquid}>RI_{conduit}$) leads to total internal reflection (TIR) at the liquid-wall interface and optical fiber-like behavior. (92) Glass LCOFs, CS_2-filled, were used in lengths up to 50 m. The authors recognized that even when TIR did not occur at the liquid-wall interface, it could take place at the outer wall-air interface, albeit attenuated by the wall itself. For LCOF behavior (a term eventually adopted by Fuwa et al. (93)), the wall needs to be: (a) transparent, and (b) have a lower RI than the fill-liquid at the measurement wavelength. While CS_2-filled glass-tubes meet these criteria at longer visible wavelengths, CS_2 is not relevant. Most measurements are made in water and hydro-organic media. Among common liquids, water and methanol have the lowest RI

values (n_{589} 1.33). This is a demanding condition for an LCW conduit. It must not only be inert and transparent, but it also must have an RI less than that of water at the operating wavelength.

B.1.1 The advent of Teflon® AF

Teflon AF (amorphous fluoropolymer, hereinafter TAF), introduced in the 1990's, first fulfilled these conditions. (94) Almost transparent between 170-2000 nm, it exhibits an RI of <~1.29 over most of this range. (95) A liquid-filled TAF tube, where TIR takes place at the liquid-wall interface, is designated a *Type I* LCOF. The molecular structure of TAF has a large amount of interstitial free space, whence the low RI. This also leads to high gas permeability, notably to CO_2. (96) Good gas permeability and optical transmission together make possible TAF tube-based chromogenic gas sensors,(97, 98) and postcolumn gaseous reagent introduction devices,(99, 100) where the gas-permeable tube is also the absorbance measurement cell. (101) TAF tubes enable on-line preparation of carbonic acid eluents,(102) or conversion of hydroxide to carbonate. (103) Good CO_2 permeability is also problematic: ambient CO_2 can decrease the pH of alkaline eluents and hydroxide to carbonate transition affects UV absorption. (104, 105) Coating an impermeable FSC on the inside or outside with TAF solves this. Dress and Franke(106-108) coated TAF inside glass tubes before TAF tubes became commercially available (silicon and glass channels have since been TAF-coated(109)). They introduced the presently preferred term LCW. (110) In HPLC, LCW cells permit smaller bores and/or longer paths than a conventional cell with the same light throughput. (111) From a 10 mm path, 100 nL (~100 µm ϕ) to a 25 mm path 2400 nL (175 µm ϕ) FS cells coated inside with TAF(112) are available for UHPLC applications,(113) some are up to 50 mm in length.(114)

Hydrophobic compounds can strongly adsorb on TAF. (115) An externally TAF-coated FS tube avoids TAF-analyte contact. Here, light proceeds through the thin FS wall (very low absorption loss) and undergoes TIR at the FS-TAF interface, a surface not in contact with the liquid. This is referred to as a *Type II* LCW. Such LCW cells (0.55 mm ϕ, 10-500 cm long commercially available(116, 117)) have been much used in oceanography. (118) Microfabricated antiresonant reflecting optical waveguides (ARROWs) rely on alternating high- and low-RI layers. (119) These can be attractive in very small volume microsensing applications but attenuation coefficients are generally much higher than the data reported here, albeit, ARROW attenuation would decrease with larger dimensions.

B.1.2 Type II LCW cells with TIR at glass/air interface

A core-illuminated fluid-filled glass tube surrounded by air was long known to behave as a waveguide. (120) Schwab and McCreery used them for Raman spectroscopy. (121) Tsunoda et al. (122, 123) first used them in absorption spectroscopy. Exterior contamination increases Type II LCW losses. Commercially available HPLC cells (60-85 mm path length) provide protection with an enclosure. (124, 125) Light input/collection approaches can be to/from the entire conduit face (the wall plus the liquid core) or the liquid core only. However, input through the entire face is avoided as wall conduction increases stray light. Approaches to etch hemicylindrical channels (and fluid I/O ports) on FS wafers and then bonding two halves together may facilitate future mass fabrication and integration to a capillary column. (126)

B.1.3 Light transmission in various tubes

How well is light conducted through a tube when LCW behavior is expected? TAF-based LCW cells have excellent light throughput, but TAF is literally more expensive than gold. Performance data of alternatives are lacking. Is Type I LCW better than Type

II? Is a TAF-coating on an FSC better than no-coating (reflection at FS-air interface) at all? How well does an externally mirrored quartz tube transmit light? Many polymer tubes have a highly reflective inside wall from the melt-extrusion process. Ruzicka, a pioneer in flow analysis, has used PEEK tubes of significant path length as absorption cells for many years. He most recently used a green PEEK tube (13 cm x 0.75 mm ϕ) maintained straight (Figure B-1) for trace nutrient measurements. (127, 128) He credits Klein of FIAlab Instruments(129) for their concept and design. Cells with up to 50 cm path length were once commercially marketed. Water-filled microporous PTFE or polypropylene (PP) tubes also show less attenuation than standard PTFE tubes of the same diameter, the basis of several chromogenic gas sensors. (130-132) How well do these tubes transmit light?

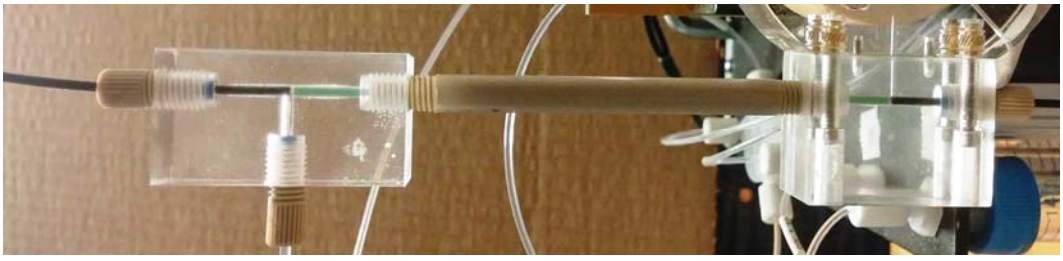

Figure B- 1 “Garth Klein cell” similar to that used by Ruzicka et al. (122, 123). The active length (consisting of the Green PEEK tubing) of the cell shown is 10 cm. A small portion of the black jacket of the 600 µm core FS optical fiber is removed such that the fiber just protrudes into the PEEK tubing which in turn is held in a linear configuration by a rigid outer snug-fit 6.3 mm o.d. PEEK casing. The perpendicular arm of each tee provides for liquid I/O. In the present case, the right end is integrated into a Lab-on-Valve (LOV) platform. Photo Credit: Graham Marshall.

B.2 Principles

B.2.1 Is there an optimum length for the best SNR?

According to Bouguer-Lambert-Beer’s law(133) (names chronologically cited(134)), absorbance increases with path length. The objective of using a long cell is a better limit of detection (LOD) via a higher signal to noise ratio (SNR). Past an initial

length for the input light intensity to become radially uniform,(126) for any uniform bore cell, light intensity will decrease exponentially with length, at least from solvent absorption, often the dominant loss in low UV and the NIR. Unfortunately, names of some commercial cells, e.g., *LightPipe, Light-guiding*, *Max-Light*, *Total Reflection* etc. leave the impression that such cells behave like optical fibers with negligible attenuation. While absorbance increases with pathlength, if there is a finite attenuation with length (whether due to the solvent or the cell characteristics) noise will increase due to decreased light throughput. In non-chromatographic situations where cell volume or band dispersion are not relevant, is there an optimum pathlength for the best SNR? Surprisingly, this has never been explicitly considered.

If the attenuation coefficient of the cell in the presence of the solvent background is α_b, I_0 is the light intensity entering the cell, and I is the light intensity that reaches the detector after traveling pathlength L,

$$I = I_0 e^{-\alpha_b L} \quad (1)$$

Adding to this background an analyte of extinction α_a (the total extinction coefficient being $\alpha_a + \alpha_b$), the new value of the transmitted light intensity in the present of the analyte, I_a is:

$$I_a = I_0 e^{-(\alpha_a+\alpha_b)L} = I e^{-\alpha_a L} \quad (2)$$

The net change in the transmitted light intensity is the signal I_s

$$I_s = I - I_a = I - I e^{-\alpha_a L} = I(1 - e^{-\alpha_a L}) \quad (3)$$

It can be readily derived that I_s has a maximum with L, this maximum L_{max} being given by (see B.2.2 for derivation of eq4):

$$L_{max} = \frac{1}{\alpha_a} \ln\left(1 + \frac{\alpha_a}{\alpha_b}\right) \quad (4)$$

Near the LOD, with the approximation that α_a/α_b is small and first term approximation of the Taylor Series expansion, ln(1+x) ≈ x (see B.2.3 for justification and details),

$$L_{max,\ signal} = 1/\alpha_b \quad (5)$$

One is, however, more interested in where the maximum SNR occurs, rather than the maximum signal. In the commonly encountered shot-noise limit (see B.2.4 for a detailed discussion), the noise *N* is proportional to the square root of the light intensity:

$$N = k\sqrt{I} \quad (6)$$

k being a constant of proportionality. The noise is therefore given by eq 7 and the SNR by eq 8:

$$N = k\sqrt{I_0 e^{-\alpha_b L}} \quad (7)$$

$$SNR = I_s/N = I(1 - e^{-\alpha_a L})/[k\ (I_0 e^{-\alpha_b L})^{0.5}] \quad (8)$$

As in going from eq 3 to eqs 4 and 5, this leads to an expression for the SNR optimum occurring at $L_{max,SNR}$ (See B.2.5 for the derivation of eq 9):

$$L_{max,SNR} = \frac{1}{\alpha_a}\ln\left(1 + 2\frac{\alpha_a}{\alpha_b}\right) \simeq 2/\alpha_b \quad (9)$$

Note that SNR_{max} is related to $\sqrt{I_0}$, but the path length at which this occurs is independent of I_0.

In practice, when noise is measured at different detector photocurrents, or conditions where neither the detection nor the recording system is resolution/bit noise limited, the lower slope bound in a log (photocurrent) - log (noise) plot is indeed observed to be 0.5, as prescribed by the shot-noise limit. The upper slope bound is observed to be 0.9 (Figure B-2). If noise can be generically expressed as I^n (where $n<1$), the general expression for $L_{max,\ SNR}$ is readily derived (see B.2.6):

$$L_{max,SNR} = \frac{1}{\alpha_a}\ln\left(1 + \frac{\alpha_a}{(1-n)\alpha_b}\right) \quad (10)$$

which can be approximated to $\frac{1}{(1-n)\alpha_b}$ provided $\frac{\alpha_a}{(1-n)\alpha_b}$ <<1.

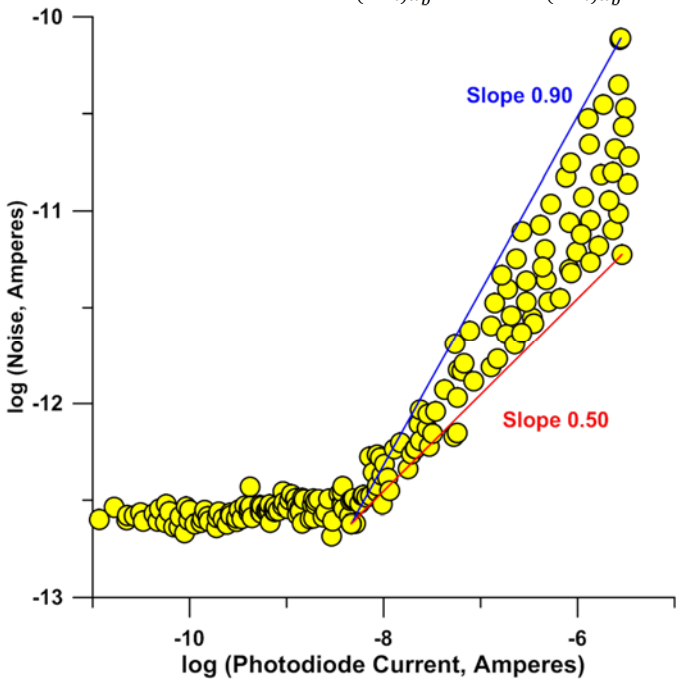

Figure B- 2 Photocurrent and associated noise measurements obtained with a current-stabilized red LED (660 nm) driven at low currents (1-10 mA) as light source coupled to a green 0.75 mm i.d. water-filled PEEK tubing as described in the foregoing section. The data were both from a Keithley 2450 SourceMeter™ or a Stanford Research SR570 Current Amplifier. Below about a photocurrent level of ~10 nA, the noise reaches a constant level of several hundred fA, due presumably to the measurement/acquisition system limitations. Above this threshold and up to a photocurrent level of ~2 μA, the slope of the log N vs. log i plot data falls between 0.5 and 0.9.

Repeating the experiment with the photocurrent in the 5 nA to 0.5 μA range corresponding to actual blank photocurrent measurements for the actual SNR measurements with MB as analyte and conducted over a short period to avoid significant temperature changes of the light source, the data, obtained solely with the Keithley 2450, corresponded to a slope of 0.62±0.06, not statistically distinguishable from the shot-noise limit slope of 0.50 at the 95% confidence level.

B.2.2 Derivation of eq 4. existence of a maximum in the intensity difference signal

Eq 3 can be written in the expanded form as

$$I_s = I_0 (\exp(-\alpha_b L) - \exp(-(\alpha_a + \alpha_b)L) \quad \text{(S1)}$$

$$dI_s/dL = I_0 [-\alpha_b \exp(-\alpha_b L) + (\alpha_a + \alpha_b)\exp(-(\alpha_a + \alpha_b)L)] \quad \text{(S2)}$$

$$dI_s/dL = I_0 [-\alpha_b(\exp(-\alpha_b L) + \alpha_b \exp(-(\alpha_a + \alpha_b)L) + \alpha_a \exp(-(\alpha_a + \alpha_b)L)] \quad \text{(S3)}$$

$dI_s/dL = I_0 [\alpha_b\{\exp(-(\alpha_a + \alpha_b)L - \exp(-\alpha_b L)\} + \alpha_a \exp(-(\alpha_a + \alpha_b)L)]$ (S4)

$dI_s/dL = I_0 [\alpha_b \exp(-\alpha_b L)(\exp(-\alpha_a L) - 1) + \alpha_a \exp(-(\alpha_a + \alpha_b)L)]$ (S5)

For a maximum of Is to exist as a function of *L*, the above derivative must be zero. Since I_0 cannot be zero, the expression inside the square brackets must be zero, hence

$\alpha_b \exp(-\alpha_b L)(\exp(-\alpha_a L) - 1) + \alpha_a(\exp(-\alpha_a L) * \exp(-\alpha_b L)) = 0$ (S6)

Dividing throughout by $\exp(-\alpha_b L)$,

$\alpha_b(\exp(-\alpha_a L) - 1) + \alpha_a(\exp(-\alpha_a L) = 0$ (S7)

$-\alpha_b + (\alpha_a + \alpha_b)\exp(-\alpha_a L) = 0$ (S8)

$\exp(-\alpha_a L) = \alpha_b/(\alpha_a + \alpha_b)$ (S9)

$L_{max\ Is} = \frac{1}{\alpha_a} \ln(\frac{\alpha_a + \alpha_b}{\alpha_b}) = \frac{1}{\alpha_a} \ln(1 + \frac{\alpha_a}{\alpha_b})$ (S10)

B.2.3 Justification of approximation leading to Eq 5: why $\alpha a/\alpha b$ is small compared to unity near the LOD

Presently attainable noise levels for state-of-the-art liquid phase UV-VIS absorbance measurement is 10^{-6} to 10^{-5} absorbance units under realistic measurement requirements conditions (spectral bandwidth 2-10 nm, time resolution 1-20 Hz). Similar noise levels have been demonstrated for a long time now for a variety of simple LED-photodiode based detectors. (135) The above is specified based on a 1 cm path length equivalent, thus the corresponding extinction coefficient α, converting from base 10 to natural logarithms, is 2.3 x 10^{-6} to 2.3 x 10^{-5} cm^{-1}. In the worst case, one may assume then that in a 1 cm path the LOD, in terms of the solution extinction coefficient represented by the analyte (α_a) will be *no greater than* 10^{-4} cm^{-1} in a 1-cm cell. In other words, for a 1 cm cell, near the LOD, the maximum value of $\alpha_a L$ is 2.3 x 10^{-5}.

The objective of increasing *L* is to reduce the detection limit. For example, if L is increased to 10 cm, the minimum detectable value of α_a will be 10^{-5}. Indeed, this is the best possible outcome, that the $\alpha_a L$ product will remain constant. In reality, because of poorer light throughput and stray light effects, typically $\alpha_{a,\,LOD} L$ will decrease with increasing L ($\alpha_{a,\,LOD}$ being the smallest detectable α_a in a cell of length *L*). In comparison the best case α_b values that we see in this work is for pure water-filled LWCCs at mid-visible wavelengths to be ~8 x 10^{-4} cm^{-1}. The α_a/α_b ratio even for a 1 cm cell near the LOD will therefore be no greater than (2.3 x 10^{-5})/(8 x 10^{-4}) = 0.029 and will decrease further, at least proportionally, if *L* is increased to improve the LOD. The approximation that α_a/α_b is small compared to 1 is therefore valid near the LOD.

B.2.4 Shot noise. Is it realistic to assume present detectors are shot noise-limited?

Walter H. Schottky first pointed out in 1918 that “Shot noise” (Schroteffekt in original German) is fundamental to photometry and is encountered whenever Poisson statistics govern the counting of objects, including photons, electrons etc.(136) The phonetic similarity of the original author’s name with “Shot noise/Schrotteffekt” had led in the literature to some interesting speculations as to the origin of the term, this is the subject of a recent paper. (137) The Schott noise equation in its full form is given as

$$i_{noise} = \sqrt{2eI\Delta f} \qquad \text{(S11)}$$

where i_{noise} is the standard deviation of the measured current *I* and *e* is the electronic charge and Δf is the frequency bandwidth over which the measurement is made; a cogent derivation of this was recently presented. (138) As most measurements are made with a fixed bandwidth, commonly the shot noise equation is simply stated in the form that the uncertainty of the counting statistics is directly proportional to the square

root of the count itself. This is the same statement that eq 1 embodies in the main text. The reader interested in more detail on noise sources in photometric measurements in general and shot noise is referred to the excellent book by McCreery.(139) Similar considerations, with a focus on charge-coupled devices (CCDs) as detectors, are available in a freely web-accessible article. (140) In another readily accessible article Pereplitsa(141) shows how Johnson Noise and Shot Noise are related to the fundamental constants: Boltzmann's Constant and the electronic charge, respectively.

It is true that under low absorbance conditions and a large light throughput, the source flicker noise can become the dominant noise, if uncompensated for.(142) However, numerous ways have been developed to compensate for source flicker noise and drift, and many such approaches, often involving dual detectors(143-146) result in performance that is shot noise limited or very nearly so. With array detectors, it is common to use detector elements, at one wavelength or binned over a wavelength range where the analyte does not absorb, as the reference to compensate for source flicker. Jones and Malcolm-Lawes(147) eliminated source flicker altogether by using a radioactive β-source exciting a solid UV scintillator as a UV source, only to be limited by shot noise. Particularly in the context of HPLC, for a long time, the detectors have been (or at least, have been considered to be) shot noise-limited. In his classic work, Baumann(148) explicitly assumed so. He considered other noise sources to be technical imperfections that can be compensated. In his own treatment of the topic, Poppe(149) quantitatively considered detector and source instabilities but in the end concluded, *..the calculations and data given by Baumann for a number of sources indeed justify the conclusion that, for cell volumes around 10 µl, present low-noise u.v.-visible detectors operate quite near to the optimum.* In these pre-LCW days, Poppe observed that a path length of 1 cm was already higher than the optimum and observed that the then recent

HPLC detectors from many manufacturers were utilizing path lengths shorter than 1 cm. He went on to state that: *The surprising result is that, at a specified cell volume, longer cells result in worse detection limits. The larger absorbance values obtained in a long cell for the same concentration are more than counterbalanced by the increased noise level in the measurement of the smaller amount of light which can be transmitted by the narrow cell.* Indeed, longer path detectors for HPLC did not come into vogue until LCW cells, with their better light throughput, came into being.

In many, if not most, well-designed liquid phase absorbance measurements, the performance is shot-noise limited or very nearly so. Unorthodox signal processing techniques have been developed with array detectors. (150, 151) Some have become incorporated into commercial detectors to attain shot noise-limited performance. As Kraiczek et al. (106) have so succinctly noted, *a shot-noise limited detector is not necessarily a good detector*. It is tantamount to the admission that the source is not bright enough. We refer the reader to the excellent discussion of the situation in that paper. But the overall scenario has a single underlying cause. For a variable wavelength detector in the UV-Vis, since the time of Baumann's assessment in the late 1970's, the only affordable and practical light source has remained the Deuterium lamp. The performance of such a lamp has surely improved some in the last half a century but not enough to make a significant difference to decrease shot noise sufficiently (especially when one considers the square root dependence on light intensity) to have altered the *status quo* regarding detectors being shot-noise limited.

In so far as the current focus, an optimum optical pathlength, there is presently no guidance on how long a pathlength is too long regardless of what noise source is dominant. If we compute a maximum pathlength assuming shot noise limitations, even if

some other noise source proves to be dominant in a particular situation, an optimum length for that case will necessarily be smaller than the shot noise-based optimum.

B.2.5 Derivation of eq 9

The following derivation is credited to an anonymous reviewer.

Restating eq S1

$$I_s = I_0(e^{-\alpha_b L} - e^{-(\alpha_a + \alpha_b)L}) \quad \text{(S1)}$$

and recalling the expression for *N*

$$N = k(I_0\, e^{-\alpha_b L})^{0.5} = k\sqrt{I_0}e^{-0.5\alpha_b L} \quad (7)$$

Therefore

$$\text{SNR} = \frac{I_S}{N} = \frac{\sqrt{I_0}}{k}\left[e^{-0.5\alpha_b L} - e^{-(0.5\alpha_b + \alpha_a)L}\right] \quad \text{(S12)}$$

Taking the derivative with respect to *L*,

$$\frac{dSNR}{dL} = \frac{\sqrt{I_0}}{k}\left[-0.5\alpha_b e^{-0.5\alpha_b L} + (0.5\alpha_b + \alpha_a)e^{-(0.5\alpha_b + \alpha_a)L}\right] \quad \text{(S13)}$$

For the SNR to have a maximum the above derivative must be zero. Since $\frac{\sqrt{I_0}}{k}$ cannot be zero, the term within the square brackets must be zero to meet this condition, whence

$$0.5\alpha_b e^{-0.5\alpha_b L} = (0.5\alpha_b + \alpha_a)e^{-(0.5\alpha_b + \alpha_a)L} \quad \text{(S14)}$$

Dividing throughout by $0.5\alpha_b$,

$$e^{-0.5\alpha_b L} = (1 + 2\frac{\alpha_a}{\alpha_b})e^{-(0.5\alpha_b + \alpha_a)L} \quad \text{(S15)}$$

Transposing,

$$e^{\alpha_a L} = 1 + 2\frac{\alpha_a}{\alpha_b} \quad \text{(S16)}$$

Recognizing that this value of *L* corresponds to the maximum SNR, we denote this as $L_{max,\ SNR}$ whence

$L_{max,SNR} = \frac{1}{\alpha_a}\ln(1 + 2\frac{\alpha_a}{\alpha_b})$ (9)

B.2.6 The case for a generic noise expression where N = I^n

We consider here the generic situation where the noise is related to some power of the light intensity incident on the detector, the shot-noise limit being included one of the possible cases (n = 0.5)

$N = k(I_0\, e^{-\alpha_b L})^n = kI_0^n e^{-n\alpha_b L}$ (7)

Therefore

$\text{SNR} = \frac{I_S}{N} = \frac{I_0^{(1-n)}}{k}\left[e^{-(1-n)\alpha_b L} - e^{-((1-n)\alpha_b+\alpha_a)L}\right]$ (S17)

Taking the derivative with respect to L,

$\frac{dSNR}{dL} = \frac{I_0^{(1-n)}}{k}\left[-(1-n)\alpha_b e^{-(1-n)\alpha_b L} + ((1-n)\alpha_b + \alpha_a)e^{-((1-n)\alpha_b+\alpha_a)L}\right]$ (S18)

For the SNR to have a maximum the above derivative must be zero. Since $\frac{I_0^{(1-n)}}{k}$ cannot be zero, the term within the square brackets must be zero to meet this condition, whence

$(1-n)\alpha_b e^{-(1-n)\alpha_b L} = ((1-n)\alpha_b + \alpha_a)e^{-((1-n)\alpha_b+\alpha_a)L}$ (S19)

Dividing throughout by $(1-n)\alpha_b$,

$e^{-(1-n)\alpha_b L} = (1 + \frac{\alpha_a}{(1-n)\alpha_b})e^{-((1-n)\alpha_b+\alpha_a)L}$ (S20)

Dividing throughout by the term on the left,

$1 = (1 + \frac{\alpha_a}{(1-n)\alpha_b})e^{-\alpha_a L}$

Transposing,

$e^{\alpha_a L} = 1 + \frac{\alpha_a}{(1-n)\alpha_b}$ (S21)

Recognizing that this value of L corresponds to the maximum SNR, we denote this as $L_{max,\ SNR}$ whence

$$L_{max,SNR} = \frac{1}{\alpha_a}\ln(1+\frac{\alpha_a}{(1-n)\alpha_b}) \quad (10)$$

B.3 Experimental Section

B.3.1 A variable pathlength cell

Inter-device differences in coupling losses at light I/O termini and device uniformity limit the utility of attenuation measurement as a function of length if different fixed pathlengths cells are used. Having a single long cell with a fixed light input and a light pickup fiber that can be moved to different distances within the cell, effectively making a variable path length (VPL) cell, solves this problem. (117) Uniformity along cell length is still implicitly assumed. Both static and flow-through VPL cells where the pathlength may be varied precisely from a few microns to several mm are now commercially available. (152) The VPL arrangement (Figure B-3) was therefore used to measure the overall attenuation coefficients α_b in water-filled tubes.

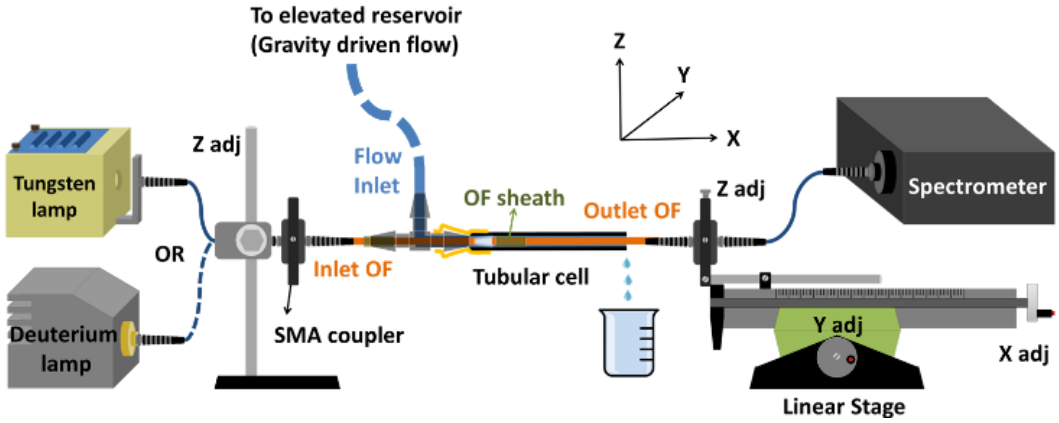

Figure B- 3 Experimental arrangement

Light from a deuterium or a tungsten lamp is coupled to the inlet optical fiber (OF, fused silica, www.molex.com) to deliver light to the cell. The transmitted light was picked up by the outlet OF coupled in turn to another OF leading to a diode array detector (P/N

G7117A, www.Agilent.com) or a Peltier-cooled back-thinned CCD array spectrometer (Exemplar Pro, www.bwtek.com). The alignment was carried out with the adjustable mounts shown. At the light pickup/fluid exit end, the fiber was movable by a micro-positioner stage. To begin, the pick-up OF was inserted until it touched the input fiber and adjusted to relieve tension/bowing while maintaining the OF's in contact. The path length was adjusted by backing out the pick-up OF in measured increments. The set up was covered and experiments were conducted in the dark to avoid dust and light intrusion.

Water was variously from (1) an unbranded deionized water system (2) an Aries Filterworks System and (3) a Milli-Q system, (4) a Barnstead Nanopure System, all with ≥18 MΩ•cm specific resistivity. These are respectively referred to as water supplies 1-4 (WS1-WS4). Several HPLC- and LC-MS grade bottled water samples were studied. The spectral extremes are respectively represented by LC1/2 and LCMS1/2. A linear plot of ln I (I being transmitted light intensity) vs. path length (L) provides the attenuation coefficient α. Only data with a linear r^2 >0.99 were used. This generally excluded data from initial few cm that represented the transition zone. (126) The exact length of this transition zone depends on the i.d. of the tube and the o.d. of the OF core, etc. Throughout this paper the cited path length is measured from a point after uniform attenuation is achieved: for example, in Figure B-4, length counting will begin at ca. 2 cm. The various tubes investigated are shown in Table B-1. All tubes (details in the Table B-2) were in a linear configuration except as stated otherwise.

Noise and SNR vs. length were measured in the VPL configuration in a 0.75 mm i.d. Polyetheretherketone (PEEK) tubing with a 660 nm light-emitting diode (LED) powered at constant current. Further details are listed in the B.3.2. Methylene blue (MB, 100 nM) in 10% (v/v) methanol was chosen as the analyte for measuring the signal and the same matrix, 10% (v/v) methanol, was used for solvent attenuation measurements.

The small amount of methanol in the solvent prevented wall adsorption and memory effects.

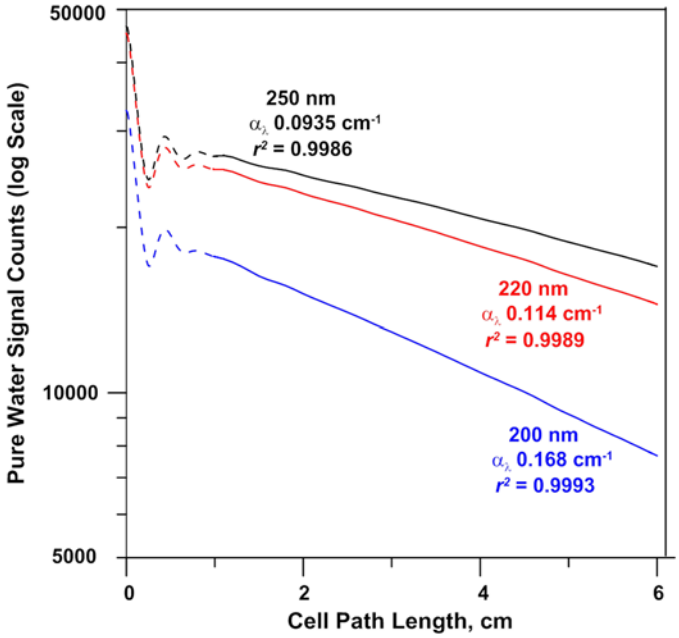

Figure B- 4 Decrease in intensity of the output light as a function of path length in a VPL air-surrounded FS LCW cell (Cell F in Table 1) at three different wavelengths: 250 nm (black), 220 nm (red) and 200 nm (blue) with an HPLC grade water sample flowing through the cell. The data for 0-10 mm path length is plotted as dashed (light intensity has not become spatially uniform) and data for longer path lengths as solid lines. The cited linear r^2 values (>10 mm path) pertain to a ln (transmitted light intensity) - path length relationship where α_λ (extinction coefficient in cm^{-1}) is the slope.

Table B- 1 Tubes Studied in attenuation experiments[a]

Designation	Description	ID, µm	Wall, µm	Optical fiber Core (Total) µm[b]
A	Teflon® AF	750	115	710
B	PTFE	780	400	710
C	PTFE	1600	15100	710
D	Porous PTFE	2000	400	1650
E	Porous polypropylene	1800	400	1500
F	Fused Silica	535	50	400 (440)
G	Quartz	1000	100	770
H	Quartz	2000	200	1650
I	Galinstan-mirrored Quartz	1000	100	770
J	Aluminum-mirrored Quartz	1000	100	770
K	Borosilicate	780	100	710
L	Borosilicate	1020	2800	770
M	Borosilicate	2200	1400	1650
N	PEEK, Natural	970	300	770
O	PEEK, Green	770	400	710

[a] Suppliers listed in Supporting Information
[b] Total outer diameter shown in parentheses if fiber was used with jacket and buffer, otherwise the latter was removed.
[c] Metallization is on exterior surface of tube, see B.3.3 for details

Table B- 2 Tubes studied in attenuation experiments

A	Teflon® Af[b]	750	115	710
B	PTFE[c]	780	400	710
C	PTFE[d]	1600	15100	710
D	Porous PTFE[e]	2000	400	1650
E	Porous polypropylene[f]	1800	400	1500
F	Fused Silica[g]	535	50	400 (440)
G	Quartz[h]	1000	100	770
H	Quartz[h]	2000	200	1650
I	Quartz (GS)[i,j]	1000	100	770
J	Quartz (Al)[k,l]	1000	100	770
K	Borosilicate[m]	780	100	710
L	Borosilicate[m]	1020	2800	770
M	Borosilicate[m]	2200	1400	1650
N	PEEK, Natural[n]	970	300	770
O	PEEK, Green[n]	770	400	710

[a] Total outer diameter is shown in parentheses if fiber was used with jacket and buffer, otherwise the latter was removed.
[b] www.biogeneral.com, courtesy Dr. Ilia Koev.
[c] Poly(tetrafluoroethylene), www.zeus.com.
[d] 1.6 mm (1/16 in.) hole drilled concentrically through a solid 3810 μm (1.5 in.) o.d. virgin PTFE rod.
[e] Gore-Tex TA002, WL Gore and Associates, Elkton, MD. [f]www.mmm.com (Membrana Division).
[g] www.polymico.com (custom size).
[h] www.vitrocom.com CV1012 and CV2024.
[i] Tube G coated outside with Galinstan (www.rotometals.com) and then covered with a clear polymer coat.
[j] As with footnote i above except tube H was coated with Galinstan; this is designated as I(2 mm).
[k] Tube G coated outside with sputtered aluminum and then covered with a clear polymer coat.
[l] Tube H coated outside with sputtered aluminum and then covered with a clear polymer coat. This is designated as J(2 mm).
[m] www.wilmad-labglass.com
[n] www.upchurch.com.

One tested device involved insertion of tube **B** inside tube **C**. This was carried out by thermally stretching one end of a segment of tube **B**, which could be then inserted fully through 10 cm long tube **C**. Then the end of tube **B** is pulled through until the originally unstretched portion fully occupies **C**. Excess **B** is then cut off from each end and the assembly thermally annealed. The pull-insertion marginally decreases the inner diameter of **B** to 750 μm.

B.3.2 Noise and SNR measurements as a function of length

The absorbance cell was constructed using green PEEK tubing (0.75 mm i.d., 1.6 mm o.d., www.upchurch.com) and was contained inside a steel jacket tube that just accommodated the polymer tube, to maintain it in a straight configuration. Tees, ¼-28 PEEK, were attached to either end (similar to that shown in Figure 1). A nominally 0.75 mm diameter acrylic fiber optic went through the tees and into the polymer tubing. Liquid flowed through the perpendicular ports. The inlet/outlet fiber optics were epoxied to a photodiode and 660 nm LED respectively. The LED had a hole drilled down to the emitter into which the fiber optic was inserted before affixing with epoxy. The LED was powered by a constant current source (1-10 mA) and the photodiode current was monitored using a Keithley 2450 with an integration time of 4 power line cycles (15 Hz acquisition). Some experiments utilized a Stanford Research SR570 Current Amplifier as the detector. Fiber optics exterior to the absorbance cell were shielded using black PTFE tubing while the silicon photodiode (Siemens BPW34, peak response at 880 nm) was maintained in a shielded metal box. The LED coupled fiber was withdrawn the specified distance and the newly exposed fiber was wrapped in metal foil. Measurements were made in a dark room. Although this is not critical, methylene blue (MB) was chosen as the analyte because of the excellent match of its absorption spectrum with the LED emission spectrum. To prevent adsorption of the dye on the walls of the conduit, the dye solution was prepared in 10% v/v methanol and the blank attenuation was also measured for the same solvent. The MB solution was 100 nM in concentration. The solvent blank or MB was delivered through the conduit by gravity using a selector valve.

B.3.3 Metallization of the exterior surface of tube

B.3.3.1 Galinstan coating

Quartz tube surfaces were pre-cleaned by methanol and completely dried. A small segment of a snug-fit PTFE tubes was inserted into each tube on both ends to prevent Galinstan ingress to the tube interior, they also facilitated handling. A pipette tip was used to transfer and spread Galinstan on the tubes. Excess Galinstan was removed from bottom end while holding the tube vertically. Then, acrylic coating (Rust-Oleum®) was sprayed evenly on each tube.

B.3.3.2 Aluminum coating

Aluminum films were produced in a magnetron sputtering system (MagSput™ series, www.torr.com) operated in d.c. mode. The purity of the aluminum target was 99.999% (www.acialloys.com). The precleaned and dried quartz tubes (with PTFE tubes inserted at each end as above) were evenly placed on a rotating substrate stage, which is 10 cm from the target. High-purity argon was fed into the chamber at a flow rate of 180 sccm. The deposition was carried out at 300 - 382 V and i = 120 to 345 mA at room temperature. The in-situ film thickness monitor indicated a maximum deposition rate of 3 Å/min. The tubes were rotated 180° when the film thickness reached 200 Å on one side. The sputtering process was then carried out on the other side. A thin layer of clear acrylic spray coat was immediately applied afterwards.

B.3.4 Attenuation in liquid waveguide capillary cells (LWCCs)

LWCCs are widely used commercially available type II LCWs (www.wpiinc.com). They are 0.55 mm i.d. FS tubes, TAF-coated on the exterior, coupled to suitable tees and 500 μm core SMA-terminated optical fibers. The data for first generation LWCCs were digitized from manufacturers archived graphical information. The numerical data for

second generation LWCCs were provided by the manufacturer (courtesy A. Dickson and M. Belz, World Precision Instruments). The attenuation coefficient α was computed as the slope of the ln *I* vs. *L* plots.

B.4 Results and discussion

B.4.1 Verification of an optimum pathlength in the transmittance signal and SNR

For 10% v/v methanol, $\alpha_{b,660\ nm}$ in the green PEEK tubing was measured to be 0.2210±0.0025 cm^{-1}. With 100 nM MB in the tube, the attenuation was 0.2321±0.0030, providing an effective α_a value of 0.0111±0.0039 cm^{-1}. This corresponds to a molar absorptivity of 47,800 $M^{-1}cm^{-1}$ for MB in comparison to a literature value of 71500 $M^{-1}cm^{-1}$ at this wavelength. A lower value is expected because of the spectral bandwidth of the LED. The photocurrent measured for the blank-filled tube ranged from 500-5 nA respectively for pathlengths of 0 to 20 cm and the corresponding log (noise) - log (photocurrent) plot had a slope of 0.62±0.06 (r^2 = 0.85). The 95% confidence limits encompass the theoretical shot noise limit of 0.50. Figure B-5 shows the intensity difference signal I_s (eq 3) as well as the SNR (dominated by the uncertainty in the measured noise) as a function of path length. Eqs 5 and 9 respectively suggest that the transmittance signal optimum and the SNR optimum should occur at pathlengths of $1/\alpha_b$ and $2/\alpha_b$, respectively. Given that α_b was 0.221, these values are 4.5 and 9 cm, respectively, precisely what is seen in Figure B-5.

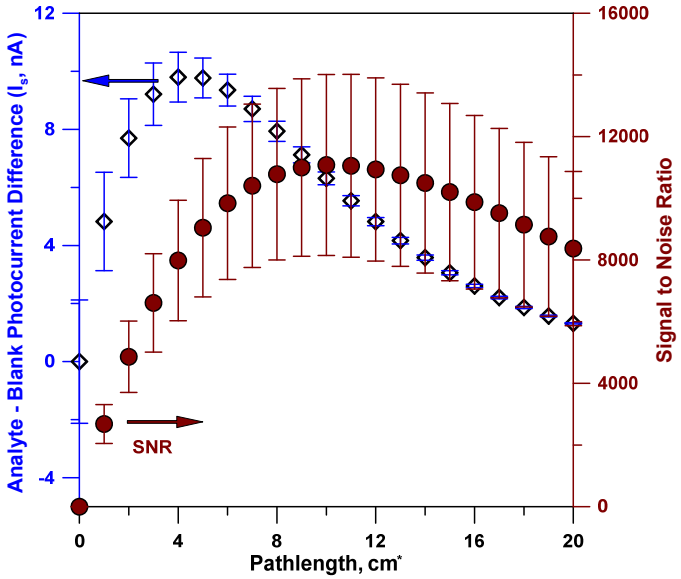

Figure B- 5 Behavior of the intensity signal I_S (hollow diamonds) and the SNR. 100 nM methylene blue in Green PEEK tubing (**O**, Table B-1), 660 nm LED. The SNR uncertainty comes from the large uncertainty bounds in the best-fit noise data.

B.4.2 VPL cells

A type II LCW-based VPL cell was first described by Tsunoda et al. (122) Except for slope spectroscopy,(152) and some isolated exceptions,(153) VPL cells have not seen much analytical use. To create a large dynamic range, multiple independent detectors of different pathlengths have been deemed more practical. (154) Very short path VPL cells with stepped interchangeable windows for preparative HPLC were patented but not commercialized. (155) The VPL approach was first used to measure the water extinction spectrum. (156) Note that for an LCW-based cell, the observed attenuation is not only from solvent extinction but also loss in the LCW. The latter is rarely negligible, except for the best LCWs at $\lambda >\sim 700$ nm.

B.4.3 Light attenuation by water

Eq 9 makes it clear that the important parameter governing the optimum length is the background attenuation coefficient. Most liquid phase assays are conducted in an aqueous medium. Hence the α_b observed for pure water sets the upper boundary for L_{max}. In practice, the actual value of L_{max} would be lower in the presence of a finite reagent blank in any reagent-based assay. One important exception is LCW-based measurements in seawater. Over a significant region in the visible where absorption due to seawater is relatively low, observed α_b for seawater is less than that for pure water because of the higher RI and increased light transmission through the LCW, permitting higher L_{max} values.

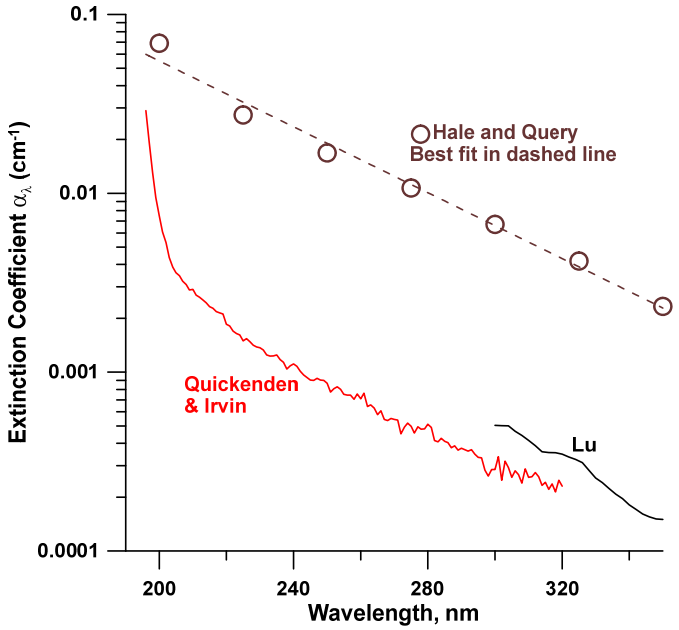

Figure B- 6 Absolute extinction coefficients reported for water in the UV (200-350 nm). Hale and Query (1973) values are based on consideration of literature data then available; others are later measurements. Note that the overall losses will include scattering, this would add another 1.3x10^{-4} cm^{-1} at 320 nm to 2.6 x 10^{-4} cm^{-1} at 200 nm, increasing exponentially with decreasing wavelength (as estimated from Buiteveld et al. (157)).

Spectral properties of “pure water” samples in the low UV wavelengths are often acutely dependent on the details of the purification system used and the extent of dissolved gases present. See Figure B-6.

An extensive compilation and discussion of water absorption data appear in a dedicated website,(158) which recommends the use of values proposed by Hale and Query(159) in 1973, based on a critical analysis of data then available. Although these values are at discrete wavelengths 25 nm apart, the relationship between log α_λ and λ for their recommendations is reasonably linear, permitting interpolation via the best linear fit (Figure B-6, Figure B-7). Note that these values represent extinction by water, waveguide losses will add to this. As any impurity present in water is likely to increase the attenuation coefficients, the lowest values reported are likely to be the true values. However, this does not address the practical question as to what value of α_b an average user, who has taken reasonable (but not extraordinary) steps to use pure water, should utilize. We studied several samples from in-house water purification systems (all resistivities 18.2 MΩ.cm) and bottled HPLC- and LC/MS-grade water, all in cell F (Figure B-7). The α_b values differ by up to 10x at the lower wavelengths. Degassing of the as-produced water did provide a perceptible decrease in absorption at the lower wavelengths (note logarithmic ordinate) for at least one of the higher absorbing samples. Some of the above data are shown in Figure B-8 with ± 1 SD error bars. None of the bottled water samples (aspirated immediately from just-opened bottles) showed lower absorption than the better in-house pure water samples. WS2, WS4D and the better bottled samples (LC1, LCMS1) converge to the same values at $\lambda \geq 280$ nm while WS1 remains substantially higher at all wavelengths. The WS1 water lacked a final particulate filter and presence of particulate matter samples (LC1, LCMS1) converge to the same values at $\lambda \geq 280$ nm while WS1 remains substantially higher at all wavelengths. The

WS1 water lacked a final particulate filter and presence of particulate matter may be responsible for the difference. At $\lambda \leq 240$ nm, WS2, WS3, LC1, and LCMS1 provided lower extinction values than Hale-Query recommendations. The ability to remove UV-absorbing impurities has presumably improved in the last half a century. At $\lambda \leq 240$ nm, LCMS1 showed perceptibly lower absorption than the HPLC grade solvent from the same manufacturer (see Figure B-9) but not above 240 nm.

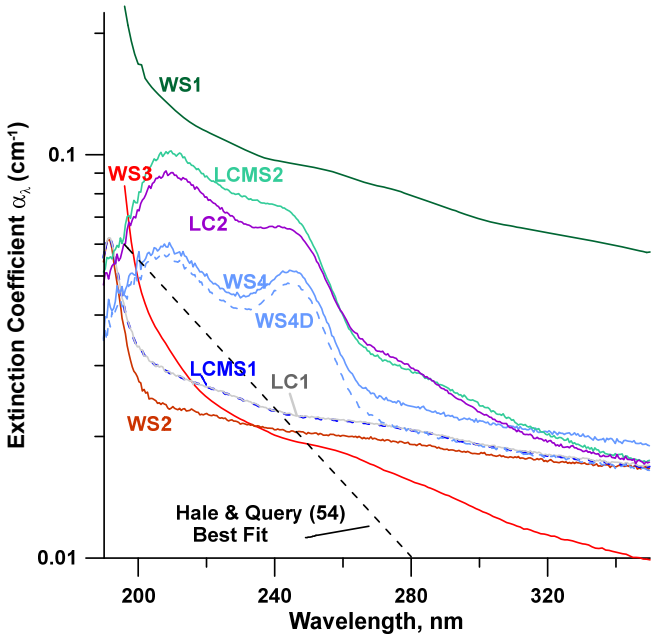

Figure B- 7 Attenuation coefficients for water in the 200-350 nm range. Observed values of α_b in tube F (Table B-1): WS1-4: Water from four different pure water systems. WS4D (dashed line) WS4 after vacuum degassing. LC1 (gray solid line) and LCMS1 (blue dashes): HPLC-grade and LC/MS-grade water from manufacturer 1 were essentially indistinguishable at λ>240 nm (but not at lower wavelengths, see Figure B-8). The relevant portion of the Hale-Query fit (Figure B-6) is also shown.

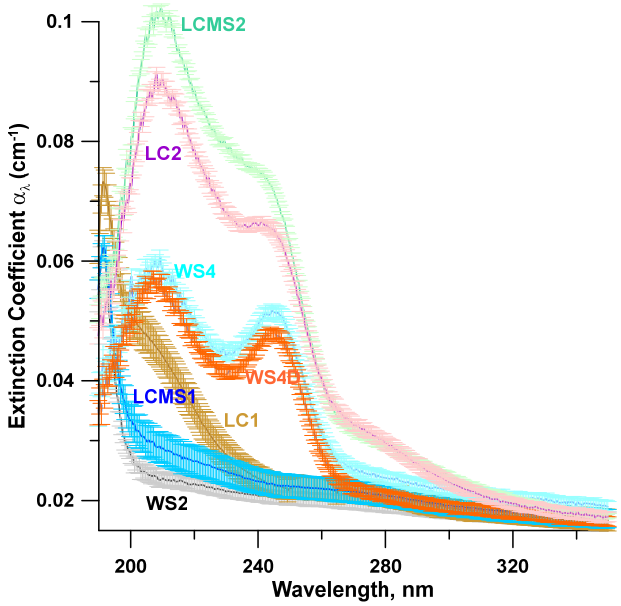

Figure B- 8 Selected traces from Figure B-5, showing ±1 SD error bars. Tube F. Note linear ordinate.

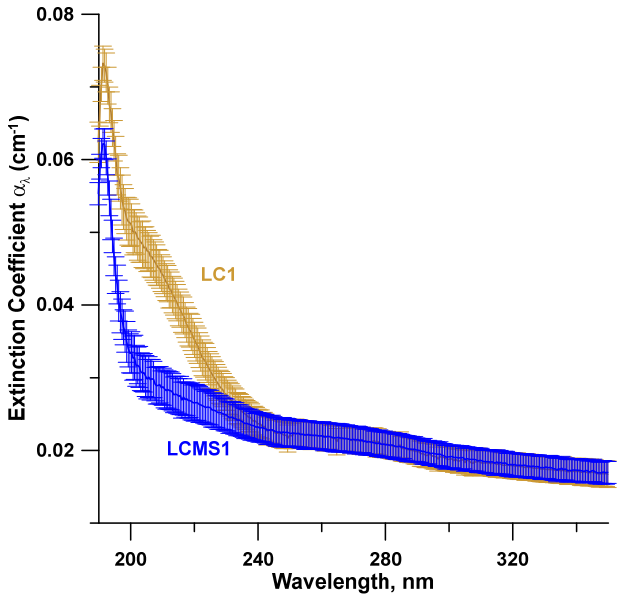

Figure B- 9 Difference between HPLC Grade (LC1) and LC/MS-Grade (LCMS1) water from the same vendor in UV absorption characteristics. Tube **F**. ±1 SD error bars are indicated. Note linear ordinate.

We conclude: (a) the observed losses in a water-filled LCW can be much higher than reported absorption coefficients for water, (b) water samples vary a lot in their observed losses, especially at $\lambda<280$ nm, and (c) bottled HPLC- or LC/MS-grade water may not provide any lower losses in the UV than freshly purified water from a good in-house system. If forced to make a recommendation for attenuation data to be picked for "pure water", we would suggest the WS2/LCMS1 data, which are close to each other and easily accessible without extraordinary effort. Importantly, while attenuation by different water samples may vary, as long as the same water is used in the different tubes, relative light losses in different conduits still provide a meaningful comparison. Water extinction data in the literature at longer wavelengths agree well, especially above 500 nm (See B.4.3.1 and Figure B-10).

B.4.3.1 Water absorption in the 300-750 nm range

Lu's data also completely coincide with results from Pope and Fry(160) obtained with an ICAM. Improvements in cavity reflectivity have now allowed ICAM measurements down to λ = 250 nm by Mason et al. (161) Mason et al., Lu, and Pope and Fry all report the absorption coefficients corrected for scattering. Buiteveld et al. (157) reported scattering and absorption coefficients separately based on their own measurements and a thorough review of the literature. For practical purposes, it is the total attenuation that is of importance. The Buiteveld data overlap that of Lu(162) at $\lambda > 500$ nm. The relevant data for λ = 300-750 nm are shown in Figure B-9.

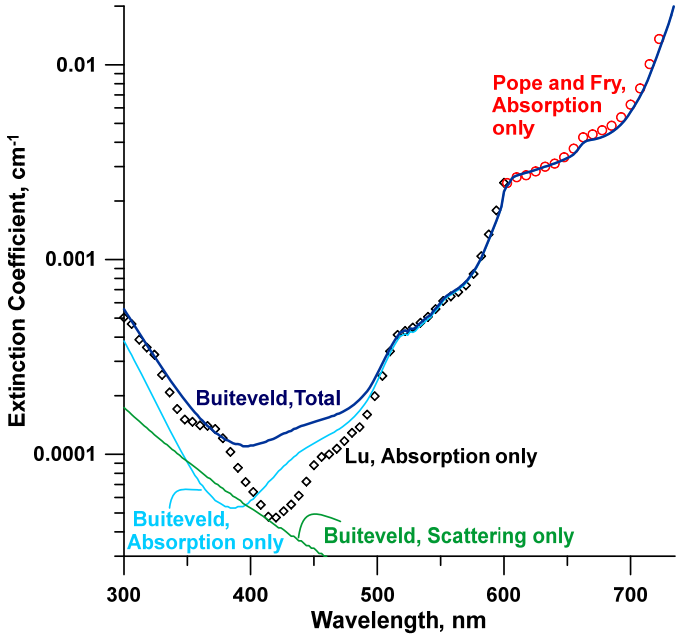

Figure B- 10 Reported water extinction data in the near UV-visible. The data of Lu and Pope /Fry are obtained by the same approach (ICAM) in the same lab. Lu's data so completely overlap Pope/Fry in the region they overlap; the two are not separately shown. Both their data represent extinction due to absorption only. Note that Buiteveld gives absorption and scattering losses separately; in practice, it is the total that matters.

B.4.4 Liquid waveguide capillary cells

Possibly the most used LCWs are the LWCC's. The 1st generation LWCCs were available in 2-500 cm length. The 2nd generation devices are available in 50-500 cm path. (163) Devices 2 mm in i.d. are available in 10-100 cm lengths. The attenuation data for two generations of water-filled LWCCs appear in Figure B-11. The difference in the water extinction data from Buiteveld et al. (157) and Mason et al. (161) reflect the large dependence on water quality. The fact that at < 300 nm the transmittance is identical between the two LWCCs generations suggest water quality in the two data sets were the same. The Gen II devices represent a real improvement in transmission at $\lambda \geq 300$ nm, especially in the 350-600 nm range. Further, LWCC-II attenuation coefficients are

virtually the same as Buiteveld's data (as well as others discussed in the SI) at $\lambda \geq 600$ nm, essentially perfect transmission. For understandable reasons, impurities generally affect the low wavelength end much more than the high wavelength end. The WS3 water-filled tube F approached LWCC transmission at both the low and high λ ends, even though WS3 was *not* the lowest attenuation water at the low wavelength end (Figure B-7). Logic dictates that the higher attenuation in the WS3 trace in the intermediate wavelengths relative to the LWCCs is due to waveguide losses.

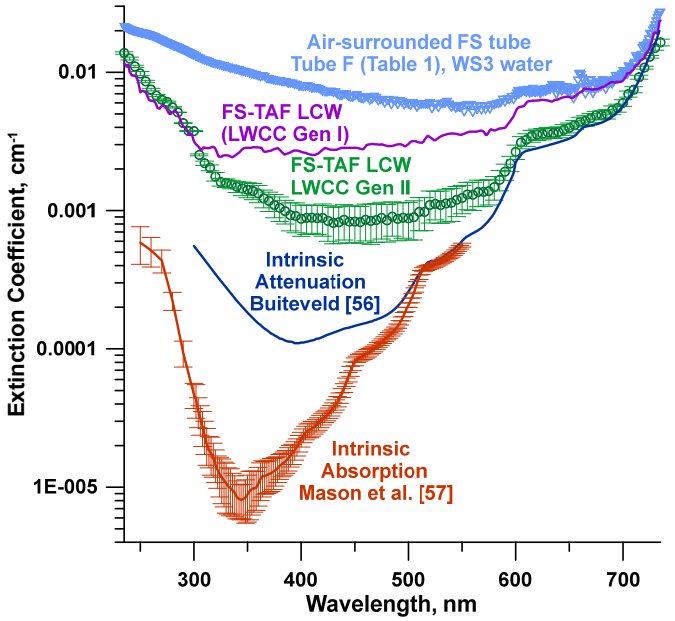

Figure B- 11 Attenuation (235-735 nm) in two generations of LWCCs compared to the data of Buiteveld et al. (157) which includes both scattering and absorption coefficients (separately shown in Figure B-10) and the recent data of Mason et al. (161) (absorption only). Also shown are data for WS3 water-filled tube **F**. Error bars indicate ±1 SD throughout.

B.4.5 Teflon® tubes

While Teflon AF tubes are benchmarks for low attenuation liquid core light conduits, the relative transmission of standard PTFE tubes, commonly used in a variety of flow systems, have never been described. PTFE is a well-known diffuse reflector,(164)

even in the deep UV. (165) It is often the material of choice for an integrating sphere. (166) Just as the reflectivity of a metal film is dependent on its thickness, so is the diffuse reflectance of PTFE. To reduce transmission loss, the thickness needs to be ≥1 cm or more. (167) We have used PTFE pipes of 1.1 cm wall thickness as a diffuse reflecting cavity. (168) We therefore studied both standard PTFE tubing (0.8 mm ϕ, 1.6 mm OD, **B**) and a thick wall pipe (31.25 mm od containing a 1.6 mm ϕ drilled concentric passage, **C**), see Figure B-12.

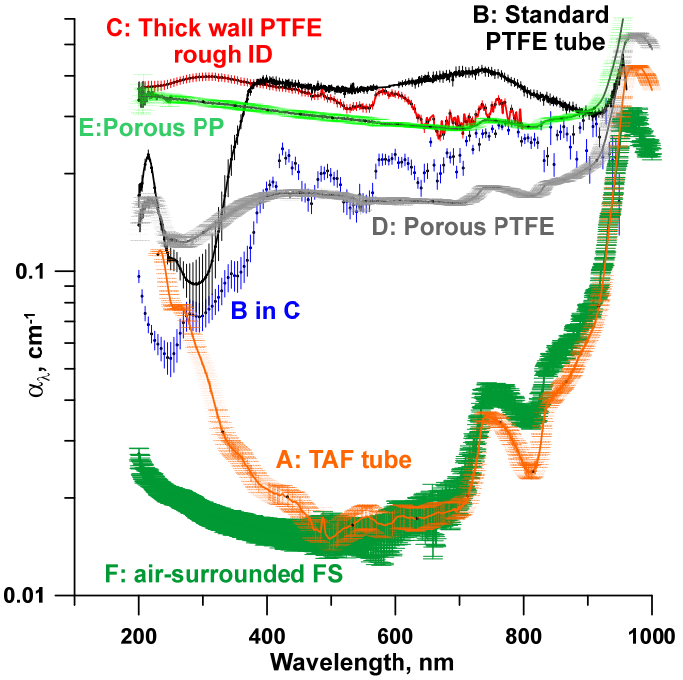

Figure B- 12 Attenuation coefficients for various WS2 water-filled Teflon tubes (including PTFE, TAF, porous PTFE) in comparison with air-surrounded FS and porous polypropylene. See Table B-1 for details.

Over most of the wavelength range a standard PTFE tube has very poor transmission ($\alpha \simeq 0.4$ cm^{-1}, connoting that >98% of light is lost in 10 cm), except in a region in the near-UV where maximum transmission is reached at 290 nm ($\alpha \simeq 0.09$ cm^{-1}, ~60% light is lost in 10 cm). In the 260-310 nm range ($\alpha \simeq 0.1$ cm^{-1}), such tubes may be

useful as cells of modest length. Introducing a much thicker wall (as in **C)** improves the long wavelength transmission marginally but the rough surface of the drilled passage ruins the short wavelength transmission Lining **C** inside with **B** provides a smooth i.d. thick-walled tube and shows better transmission than any of the foregoing, especially in the UV, reaching α = 0.055 cm^{-1} (~42% light lost in 10 cm) at 250 nm. The $\alpha \leq 0.08$ cm^{-1} (~55% light lost in 10 cm) window has a very useful span of 205-315 nm.

The light transmission in porous hydrophobic membranes (PTFE and PP) is of interest. (130-132) The transmission efficiency should depend on the RI of the base polymer, surface porosity, pore tortuosity, pore structure, membrane thickness (*t*) etc. The porous PTFE tube (**D**, n_{589} 1.356, *t* = 0.4 mm) has a pore size of 0.2 μm while the PP (**E**, n_{589} 1.49, *t* = 0.4 mm) tube has a pore size distribution, ranging from 0.22-0.66 μm. But there is a vast difference in light attenuation between the two membranes in the visible. Tube **E** has only somewhat greater transmission than a standard PTFE tube while α_b for tube **D** is much lower.

None of the above, however are a match for a TAF tube (**A**) where <20% of the light is lost in a 10 cm passage (α = 0.02 cm^{-1}) over much of the visible range (430-710 nm). In our experience, the exact attenuation in a TAF tube is highly variable (especially in the UV) and subject to any surface imperfection. Over a period of use, the light transmission efficiency often decreases. Contaminants can be irreversibly adsorbed(120) and/or adventitious particles can scratch the exposed surface (the latter may explain the transmission loss extending to the visible region). In addition, all fluorocarbons are hydrophobic. Any outgassing of dissolved gases leads to formation of microbubbles on the exposed surface and loss of transmission efficiency. Previously we had to plasma-treat PTFE to make the surface hydrophilic for use as a (diffuse) reflecting cavity in

contact with water. (168) These problems are absent in Type II LCWs (LWCCs), They also provide excellent transmission (Figure B-11).

B.4.6 Fused silica/quartz tubes

Figure B-11 indicates that an air-surrounded silica tube (e.g., tube **F**) is second only to Type II silica-TAF LWCCs in its transmissivity. It performs comparably to LWCCs at both ends of the spectrum but does appreciably worse in the 350-600 nm range. The transmissivity of **F** in the 700-800 nm range is high (Figure B-12): the absorption band of water around ~ 750 nm(169) can be clearly seen. A silica-air Type II LCW *should* have performance comparable to a silica-TAF LCW, in fact with a greater numerical aperture because RI difference at the reflection interface is greater. Why this is not observed may be due to the handling of such tubes under non-cleanroom conditions whereas TAF coated tubes are essentially coated during the extrusion process, immediately protecting the surface.

Predictably, taking a silica tube as such and surrounding it with a low RI liquid fluorocarbon, rather than air, *does no*t improve the transmission loss (Figure B-13). The transmission efficiency decreases with increasing RI of the surrounding fluid. However, if the exterior surface of a glass or silica tube is deliberately compromised, e.g., by abrasion, the transmission improves as the fluid RI approaches that of glass, closer index matching reduces the scattering loss (Figure B-14). In any case, long lengths of thin-walled fragile uncoated silica tubes are impractical. Increased wall thickness reduces fragility but precludes coiling and reduces the transmission efficiency as well (Figure B-15). The obligatory straight configuration may only permit a modest length but can still be of value. In some situations, the background attenuation α_b is sufficiently low, however, L_{max} (eq 9) cannot be practically reached by a straight tube in any case.

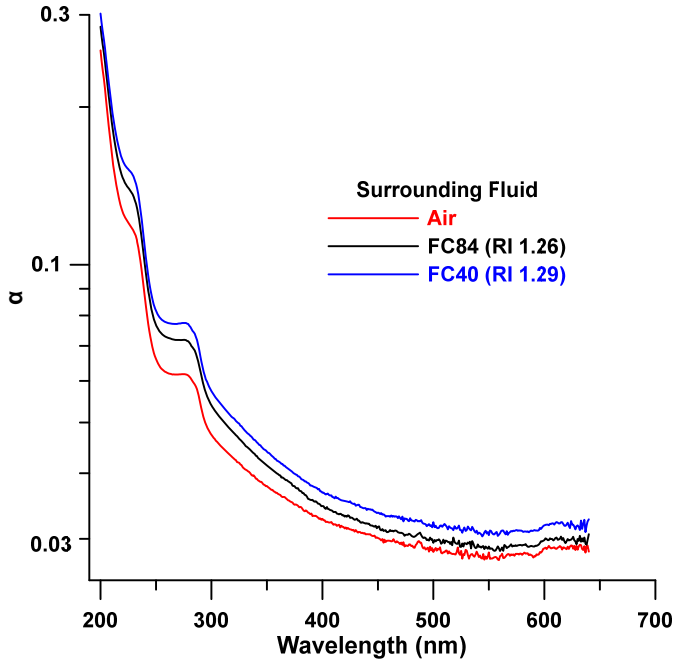

Figure B- 13 Light attenuation of water-filled fused silica tube (tube F) with different surrounding fluids on the outside.

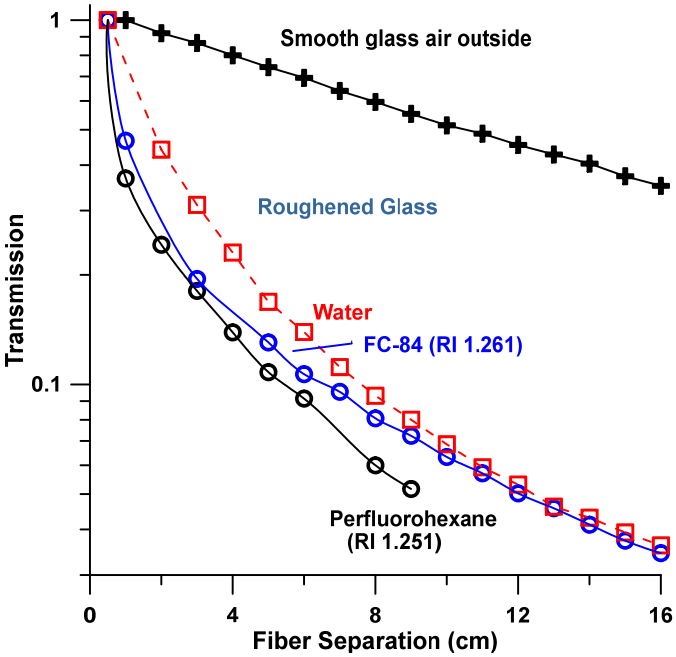

Figure B- 14 Transmission of 550 nm LED light through a borosilicate glass tube 1 mm i.d. and 0.5 mm wall thickness. This tube does not appear in Table 1. Top trace: water-

filled tube, outside fluid air. Other traces show light transmission through the same water-filled tube where the exterior surface has been deliberately been sanded to be rough and surrounded with different liquids as indicated.

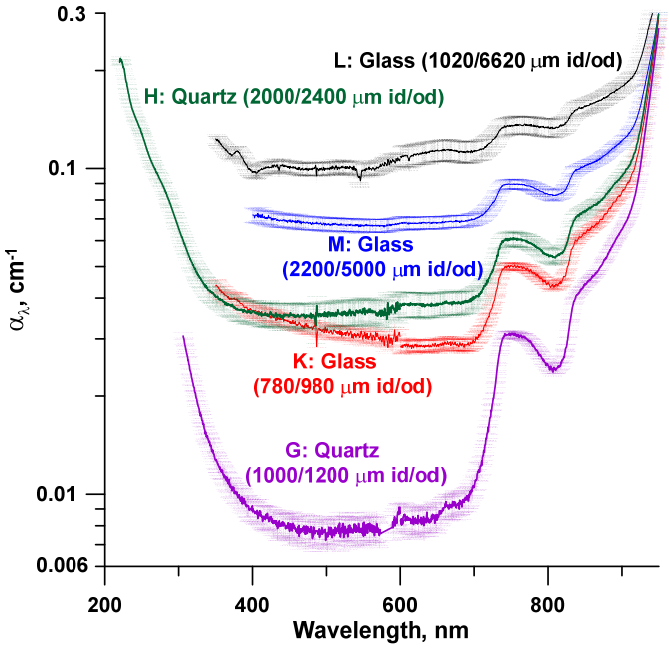

Figure B- 15 Attenuation by glass and quartz tubes (see Table B-1) of different diameters and wall thickness.

B.4.7 Externally mirrored quartz and internally reflective polymer tubes

Figure B-16 shows the behavior of two PEEK tubes and several externally mirrored quartz tubes. The mirrored tubes predictably have greater loss compared to the uncoated air-surrounded tubes where TIR occurs at the glass-air interface. However, they do not need to be protected from external light. That a very easy to create Galinstan coated tube provided better results than an aluminum mirror was surprising. It is possible that the deposited Al film thickness was inadequate. Neither PEEK tube performed better than the glass tubes, mirrored or not. Curiously, the green pigmented tube exhibited lower loss than the unpigmented “natural” tube. The difference, while not large, is likely due to the much thinner wall of the latter that makes it nearly translucent and allows

transmissive loss through the wall. In any case, the light throughput through a green PEEK tube was significantly better than a PTFE tube of similar dimensions. Compared to a glass tube, a PEEK tube can be bent but unlike a TAF tube, results in severe loss of transmission (Figure B-17). In any case, with an $\alpha_b \sim\geq 0.2$ cm^{-1} over 400-700 nm, L_{max} is small enough to be easily handled in a straight configuration. This will be even shorter in the presence of a finite reagent background absorbance.

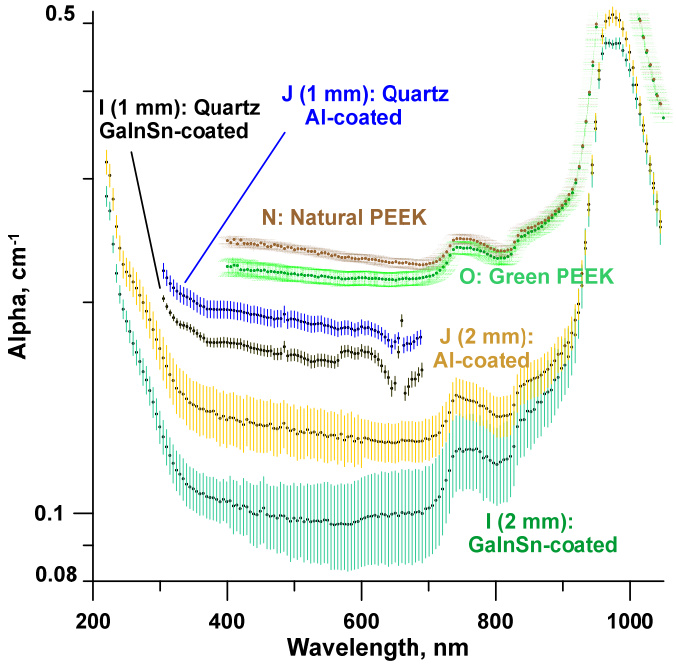

Figure B- 16 Light attenuation by (a) externally mirrored 1 and 2 mm ϕ quartz tubes (**I, J**) and (b) Green (**O**, 0.75 mm ϕ) and natural (without pigment, **N**, 1.0 mm ϕ) PEEK tubing.

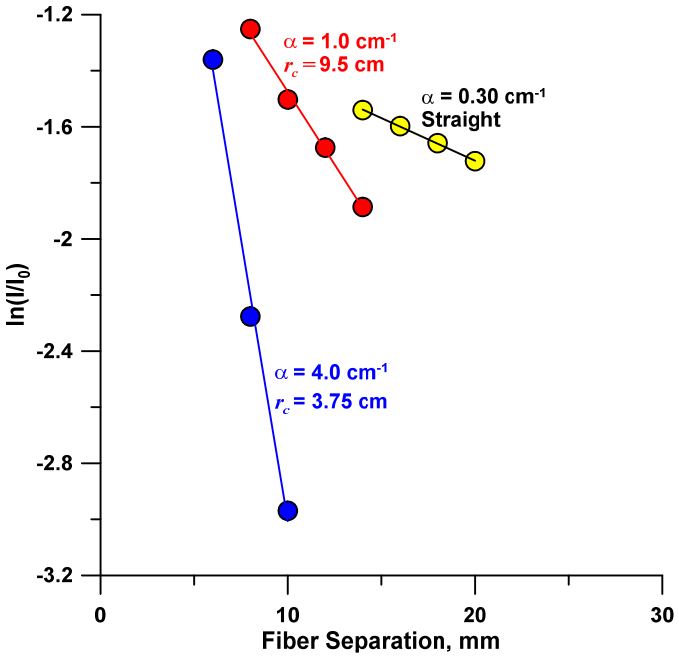

Figure B- 17 Attenuation of 660 nm light from a LED through a 0.75 mm i.d. green PEEK tube (tube **O**) as a function of distance and radius of curvature.

B.4.8 Practical cells and consequences of a finite optimum length

The present use of LCW cells is particularly important in HPLC,(113, 114, 124, 125) atmospheric measurements of gases (especially HONO) through chromogenic reactions,(170) and flow injection analysis, especially in oceanography. (171) Applications of long path cells for various measurements have been reviewed. (172) Except for an effort to find optimum cell dimensions in HPLC to find a compromise between resolution and absorbance LODs (both dependent on cell dimensions),(111) there is little guidance in choosing the length of LCW cells as to what pathlength may be too long. Worsfold et al. (171) noted that attainable LODs in LCW cells are likely to be worse than those just based on the increased absorbance. The attainment of a shot-noise limited performance or close to it is recognized in state-of-the-art HPLC detectors,(126) but elsewhere it is not appreciated that if other noise sources can be minimized, shot noise remains the ultimate

limit. Thus, in all measurements following Bouguer-Lambert's law, an optimum path length exists. Unlike in HPLC, where L_{max} suggested by eq 9 is longer than practical, this consideration is meaningful in long path cells used in flow analysis,(172) whether in atmospheric, oceanographic, or radionuclide(173) measurements. Wang et al(174) argued theoretically and experimentally that the observed absorbance measured in a long path LCW is not linear with the pathlength. Most subsequent experimental data indicate no significant departure from linearity, however. But this does not address whether cell path lengths used in certain experiments are longer than optimum.

An LWCC has low intrinsic attenuation. Often the reagent blank, and/or the matrix absorption, small as they may be, become the limiting factor. Implications for specific cases, such as the effect of the reagent blank for the widely used Griess-Saltzman reaction for determining NO_2(g), HONO(g) or NO_2^-(aq) (and NO_3^-(aq) after reduction) and oceanographic measurements in the presence of matrix absorption and scattering are discussed in the B.4.8.1.

B.4.8.1 Implications for specific cases

The reagent blank for the widely used Griess-Saltzman reaction for determining NO_2(g), HONO(g) or NO_2^-(aq) (and NO_3^-(aq) after reduction) is ~0.0005 absorbance units/cm with fresh, separated reagents. This translates to an α_b of 0.0015, and thence an L_{max} of ~1.5 m. A Long Optical Path Absorption Photometer (LOPAP) instrument has been often used to determine NO_2(g) or HONO(g). There are a significant number of LOPAP-related publications: taking examples at random, the path lengths used range from 1.4-2.4 m(175) and 2.5 m(176) to as long as 6 m.(177) It is also important to recognize that many of these instruments are not only intended for continuous monitoring, good time resolution is often desirable in such applications.

Another major application area of long path cells is in oceanographic measurements. Compared to measurements of pure or less saline water, light throughput through a 0.6 M NaCl solution is perceptibly greater through any of the tubes due to the increased RI (aside from increased numerical aperture, due to reduced Fresnel loss at the interface of the core liquid and the window or the Fiber optic) see Figure B-18). However, the exact extent of the effect on different commercial or laboratory-made LCW cells may differ significantly. (178) Opposing this increased light throughput is the increased absorption by seawater from various dissolved and suspended material. The absorption coefficients of relatively low absorbing mid-ocean Hawaiian waters range, for example, from 0.0016 at 350 nm to $6x10^{-5}$ cm^{-1} at 550 nm. (178) The best way to choose the length of a long path cell in any given oceanographic measurement application should first involve the measurement of attenuation in the sample medium at the appropriate wavelength, to which, as applicable, the attenuation due to the reagent blank needs to be added.

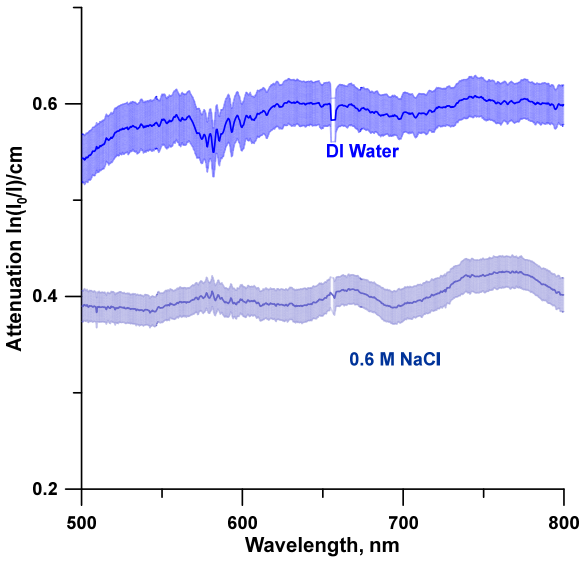

Figure B- 18 Attenuation coefficient of water and 0.6 M NaCl solution in a thick-walled PTFE tube (tube **B** in tube **C**).

B.5 Conclusions

It is widely recognized that the sensitivity of spectrophotometric/colorimetric measurements increase with increasing pathlength. However, it is not generally realized that in shot-noise limited situations and for a fixed measurement time, an optimum path length (L_{max}) exists in terms of SNR. Beyond this length, the SNR will start decreasing. This optimum path length is inversely proportional to the attenuation coefficient of light with path length. We have provided here the attenuation coefficients of a large variety of water-filled tubular conduits. Where the intrinsic attenuation coefficients are relatively high, e.g. with the PEEK tubes, this, rather than the reagent blank absorption is likely to control L_{max}. The SNR optimum occurs at $2/\alpha_b$ (eq S9), suggesting an L_{max} of ~10 cm for green PEEK tubes. It may not be coincidental that although such cells were once marketed in lengths up to 50 cm, in recent publications the length used was 13 cm.(127, 128)[40,41] The transmission is affected by surface conditions, if a surfactant like sodium dodecyl sulfate is used for a prolonged period, transmission increases (Ruzicka, J. personal communication, June, 2019). Finally, in a continuous flow system, increasing the flow cell length increases the residence time, tantamount to increasing the integration time, which should just as well be increased.

References

1. Qin C, Stamos B, Dasgupta PK. Inline Shunt Flow Monitor for Hydrocephalus. Anal Chem. 2017 08/01;89(15):8170-6.

2. Qin C, Olivencia-Yurvati AH, Williams Jr AG, Eskildsen D, Mallet RT, Dasgupta PK. Inline flow sensor for ventriculoperitoneal shunts: Experimental evaluation in swine. Med Eng Phys. 2019;67:66-72.

3. Schrander-Stumpel C, Fryns JP. Congenital hydrocephalus: nosology and guidelines for clinical approach and genetic counselling. Eur J Pediatr. 1998 May;157(5):355-62.

4. Nulsen FE, Spitz EB. Treatment of hydrocephalus by direct shunt from ventricle to jugular vain. Surg Forum. 1951:399-403.

5. Hanlo P, Cinalli G, Vandertop W, Faber J, Bogeskov L, Borgesen S, et al. Treatment of hydrocephalus determined by the European Orbis Sigma Valve II survey: a multicenter prospective 5-year shunt survival study in children and adults in whom a flow-regulating shunt was used. J Neurosurg. 2003 JUL;99(1):52-7.

6. Kohnen W, Kolbenschlag C, Teske-Keiser S, Jansen B. Development of a long-lasting ventricular catheter impregnated with a combination of antibiotics. Biomaterials. 2003 Nov;24(26):4865-9.

7. Drake JM, Kestle JR, Tuli S. CSF shunts 50 years on--past, present and future. Childs Nerv Syst. 2000 Nov;16(10-11):800-4.

8. Kestle J, Drake J, Milner R, Sainte-Rose C, Cinalli G, Boop F, et al. Long-term follow-up data from the Shunt Design Trial. Pediatr Neurosurg. 2000 Nov;33(5):230-6.

9. Harris C, Pearson K, Hadley K, Zhu S, Browd S, Hanak BW, et al. Fabrication of three-dimensional hydrogel scaffolds for modeling shunt failure by tissue obstruction in hydrocephalus. Fluids Barriers CNS. 2015 Nov 14;12:26,015-0023-9.

10. Khan AA, Jabbar A, Banerjee A, Hinchley G. Cerebrospinal shunt malfunction: recognition and emergency management. Br J Hosp Med (Lond). 2007 Dec;68(12):651-5.

11. Patel DM, Tubbs RS, Pate G, Johnston JM, Jr., Blount JP. Fast-sequence MRI studies for surveillance imaging in pediatric hydrocephalus. Journal of Neurosurgery-Pediatrics. 2014 APR;13(4):440-7.

12. Shellock FG, Wilson SF, Mauge CP. Magnetically programmable shunt valve: MRI at 3-Tesla. Magnetic Resonance Imaging. 2007 September 2007;25(7):1116-21.

13. Swoboda M, Hochman MG, Mattiucci ME, Fritz FJ, Madsen JR, inventors; United States patent US 9,138,568 B2. 2015 .

14. Patra DP, Bir SC, Maiti TK, Kalakoti P, Cuellar H, Guthikonda B, et al. Role of radiological parameters in predicting overall shunt outcome after ventriculoperitoneal shunt insertion in pediatric patients with obstructive hydrocephalus. Neurosurg Focus. 2016 NOV;41(5):E4.

15. Simon TD, Riva-Cambrin J, Srivastava R, Bratton SL, Dean JM, Kestle JR, et al. Hospital care for children with hydrocephalus in the United States: utilization, charges, comorbidities, and deaths. J Neurosurg Pediatr. 2008 Feb;1(2):131-7.

16. Narayanaswamy A, Nourani M, Tamil L, Bianco S. A wireless monitoring system for Hydrocephalus shunts. Conf Proc IEEE Eng Med Biol Soc. 2015 Aug;2015:829-32.

17. KADOWAKI C, HARA M, NUMOTO M, TAKEUCHI K, SAITO I. Csf Shunt Physics - Factors Influencing Inshunt Csf Flow. Childs Nervous System. 1995 APR;11(4):203-6.

18. Medtronic Neurosurgery PS Medical CSF-Flow Control Valves, instructions for use. 2008. Report No.: 13651-1G 21251.

19. Raj R, Lakshmanan S, Apigo D, Kanwal A, Liu S, Russell T, et al. Demonstration that a new flow sensor can operate in the clinical range for cerebrospinal fluid flow. Sens Actuators A Phys. 2015 Oct 1;234:223-31.

20. Miller TE, Small H. Thermal pulse time-of-flight liquid flow meter. Anal Chem. 1982 05/01;54(6):907-10.

21. Yu L, Kim BJ, Meng E. An implantable time of flight flow sensor. 2015 28th IEEE International Conference on Micro Electro Mechanical Systems (MEMS): ; 2015.

22. Pennell T, Yi JL, Kaufman BA, Krishnamurthy S. Noninvasive measurement of cerebrospinal fluid flow using an ultrasonic transit time flow sensor: a preliminary study. J Neurosurg Pediatr. 2016 Mar;17(3):270-7.

23. Enikov ET, Edes G, Skoch J, Anton R. Application of GMR sensors to liquid flow sensing. J Microelectromech Syst. 2015;24:914-20.

24. Bork T, Hogg A, Lempen M, MÃ¼ller D, Joss D, Bardyn T, et al. Development and in-vitro characterization of an implantable flow sensing transducer for hydrocephalus. Biomed Microdevices. 2010;12(4):607-18.

25. Clark TM, Malpas SC, McCormick D, Heppner P, Budgett DM. Implantable Multi-Modal Sensor to Improve Outcomes in Hydrocephalus Management. Ieee Sensors Journal. 2015 OCT;15(10):6027-35.

26. Madsen JR, Abazi GS, Fleming L, Proctor M, Grondin R, Magge S, et al. Evaluation of the ShuntCheck noninvasive thermal technique for shunt flow detection in hydrocephalic patients. Neurosurgery. 2011 Jan;68(1):198,205; discussion 205.

27. Marlin AE, Gaskill SJ. The use of transcutaneous thermal convection analysis to assess shunt function in the pediatric population. Neurosurgery. 2012 Jun;70(2 Suppl Operative):181-3.

28. P. Li, R. Bashirullah. A Wireless Power Interface for Rechargeable Battery Operated Medical Implants. IEEE Transactions on Circuits and Systems II: Express Briefs. 2007;54(10):912-6.

29. Olson DP, Phillips WC, Schmeling AL, inventors; October 11, 2016 .

30. Badstilbner KD, Speicher JR, Heilman MS, Bates RA, Greene CE, inventors; April 12, 2016 .

31. [Internet].; 2016 [].

32. Kelly G. Body temperature variability (Part 1): a review of the history of body temperature and its variability due to site selection, biological rhythms, fitness, and aging. Altern Med Rev. 2006 Dec;11(4):278-93.

33. Webb P. Temperatures of skin, subcutaneous tissue, muscle and core in resting men in cold, comfortable and hot conditions. Eur J Appl Physiol Occup Physiol. 1992;64(5):471-6.

34. [Internet].; 2016 [].

35. Ganz W, Donoso R, Marcus HS, Forrester JS, Swan HJC. A new technique for measurement of cardiac output by thermodilution in man. The American Journal of Cardiology. 1971 April 1971;27(4):392-6.

36. Sathanandam S, Kashyap P, Zurakowski D, Bird L, McGhee V, Towbin J, et al. Effect of solute temperature in the measurement of cardiac output in children using the thermodilution technique. Congenit Heart Dis. 2017 Mar;12(2):181-7.

37. Kadowaki C, Hara M, Numoto M, Takeuchi K, Saito I. CSF shunt physics: factors influencing inshunt CSF flow. Child's Nervous System. 1995 04/01;11(4):203-6.

38. Damkier HH, Brown PD, Praetorius J. Epithelial Pathways in Choroid Plexus Electrolyte Transport. Physiology. 2010 AUG;25(4):239-49.

39. Levin E, Muravchick S, Gold M. Density of Normal Human Cerebrospinal-Fluid and Tetracaine Solutions. Anesth Analg. 1981;60(11):814-7.

40. Lui ACP, Polis TZ, Cicutti NJ. Densities of cerebrospinal fluid and spinal anaesthetic solutions in surgical patients at body temperature. Canadian Journal of Anaesthesia. 1998 04/01;45(4):297.

41. McGuire G, Crossley D, Richards J, Wong D. Effects of varying levels of positive end-expiratory pressure on intracranial pressure and cerebral perfusion pressure. Crit Care Med. 1997 JUN;25(6):1059-62.

42. Videtta W, Villarejo F, Cohen M, Domeniconi G, Cruz R, Pinillos O, et al. Effects of positive end-expiratory pressure on intracranial pressure and cerebral perfusion pressure. Acta Neurochir Suppl. 2002;81:93-7.

43. Yang B, Zhang M, Kanyanee T, Stamos BN, Dasgupta PK. An Open Tubular Ion Chromatograph. Anal Chem. 2014 12/02;86(23):11554-61.

44. Zhou F, Lu Y, Ficarro SF, Webber JT, Marto JA. Nanoflow Low Pressure High Peak Capacity Single Dimension LC-MS/MS Platform for High-Throughput, In-Depth Analysis of Mammalian Proteomes. Analytical Chemistry. 2012;84(11):5133-9.

45. Haselberg R, De Jong GJ, Somsen GW. Low-Flow Sheathless Capillary Electrophoresis-Mass Spectrometry for Sensitive Glycoform Profiling of Intact Pharmaceutical Proteins. Analytical Chemistry. 2013;85:2289-96.

46. Yang Y, Chen H, Beckner MA, Xiang P, Lu JJ, Cao C, et al. Narrow, Open, Tubular Column for Ultrahigh-Efficiency Liquid-Chromatographic Separation under Elution Pressure of Less than 50 bar. Anal Chem. 2018 09/18;90(18):10676-80.

47. Sharma S, Plistil A, Barnett HE, Tolley HD, Farnsworth PB, Stearns SD, et al. Hand-Portable Gradient Capillary Liquid Chromatography Pumping System. Anal Chem. 2015 10/20;87(20):10457-61.

48. Deguchi K, Ito S, Yoshioka S, Ogata I, Takeda A. Nanoflow Gradient Generator for Capillary High-Performance Liquid Chromatography. Anal Chem. 2004 03/01;76(5):1524-8.

49. Darby SG, Moore MR, Friedlander TA, Schaffer DK, Reiserer RS, Wikswo JP, et al. A metering rotary nanopump for microfluidic systems. Lab on a chip. 2010 12/07;10(23):3218-26.

50. Shiue S, Peng H, Lin C, Wang S, Rau R, Cheng J. Continuous Intrathecal Infusion of Cannabinoid Receptor Agonists Attenuates Nerve Ligation–Induced Pain in Rats. Reg Anesth Pain Med. 2017 07/01;42(4):499.

51. Medtronic.com. https://www.medtronic.com/us-en/healthcare-professionals/products/neurological/intrathecal-baclofen-therapy-systems/synchromed-ii.html; . SynchroMed II Drug Infusion Pump.

52. Nazario CED, Silva MR, Franco MS, Lanças FM. Evolution in miniaturized column liquid chromatography instrumentation and applications: An overview. Journal of Chromatography A. 2015 20 November 2015;1421:18-37.

53. Šesták J, Moravcová D, Kahle V. Instrument platforms for nano liquid chromatography. Journal of Chromatography A. 2015 20 November 2015;1421:2-17.

54. Melvad C, Kruhne U, Frederiksen J. Design considerations and initial validation of a liquid microflow calibration setup using parallel operated syringe pumps. Measurement Science and Technology. 2010 JUL;21(7):074004.

55. Patrone PN, Cooksey G, Kearsley A. Dynamic Measurement of Nanoflows: Analysis and Theory of an Optofluidic Flowmeter. Phys Rev Applied. 2019 03/11;11(3):034025.

56. Kuo JTW, Yu L, Meng E. Micromachined Thermal Flow Sensors—A Review. Micromachines. 2012;3(3).

57. Nguyen NT. Micromachined flow sensors—a review. Flow Measurement and Instrumentation. 1997 March 1997;8(1):7-16.

58. Sensirion. https://www.scribd.com/document/257899459/Sensirion-Liquid-Flow-LG16-Datasheet-V1-5. . Liquid flow meter LG16-0025.

59. Etxebarria J, Berganzo J, Elizalde J, Llamazares G, Fernández LJ, Ezkerra A. Low cost polymeric on-chip flow sensor with nanoliter resolution. Sensors and Actuators B: Chemical. 2016 1 November 2016;235:188-96.

60. Dijkstra M, de Boer MJ, Berenschot JW, Lammerink TSJ, Wiegerink RJ, Elwenspoek M. Miniaturized thermal flow sensor with planar-integrated sensor structures on semicircular surface channels. Sensors and Actuators A: Physical. 2008 2 May 2008;143(1):1-6.

61. Wu S, Lin Q, Yuen Y, Tai Y. MEMS flow sensors for nano-fluidic applications. Sensors and Actuators A: Physical. 2001 20 March 2001;89(1):152-8.

62. Kuo JTW, Chang L, Li P, Hoang T, Meng E. A microfluidic platform with integrated flow sensing for focal chemical stimulation of cells and tissue. Sensors and Actuators B: Chemical. 2011 1 March 2011;152(2):267-76.

63. Richter M, Woias P, Weiß D. Microchannels for applications in liquid dosing and flow-rate measurement. Sensors and Actuators A: Physical. 1997 July 1997;62(1):480-3.

64. Ahrens M, Klein S, Nestler B, Damiani C. Design and uncertainty assessment of a setup for calibration of microfluidic devices down to 5 nL min^{-1}. Measurement Science and Technology. 2014;25:015301.

65. Westin KJA, Choi C-, Breuer KS. A novel system for measuring liquid flow rates with nanoliter per minute resolution. Exp Fluids. 2003 05/01;34(5):635-42.

66. Temiz Y, Delamarche E. Sub-nanoliter, real-time flow monitoring in microfluidic chips using a portable device and smartphone. Scientific Reports. 2018 07/13;8(1):10603.

67. Levy A. The accuracy of the bubble meter method for gas flow measurements. J Sci Instrum. 1964 07;41(7):449-53.

68. Kusnetz HL. Air Flow Calibration of Direct Reading Colorimetric Gas Detecting Devices. Am Ind Hyg Assoc J. 1960 08/01;21(4):340-1.

69. Schnell G. Measurement of flow in infusion systems. Med Biol Eng Comput. 1997 Nov;35(6):737-41.

70. Geller EW. An electrochemical method of visualizing the boundary layer. Journal of the Aeronautical Sciences. 1955;22(12):869-70.

71. Bannerot RB, Tu Y, Scott A, Placke G, Poché T. A simple device for monitoring flow rates in thermosyphon solar water heaters. Journal of solar energy engineering. 1992;114(1):47-52.

72. Khalifa AJN, Mehdi MM. On the verification of a hydrogen bubble flow meter used for monitoring flow rates in thermosyphon solar water heaters. Energy Conversion and Management. 1998 August 1998;39(12):1295-302.

73. Wu J, Sansen W. Electrochemical time of flight flow sensor. Sensors and Actuators A: Physical. 2002;97:68-74.

74. Lippmann JM, Pisano AP. Bubble time-of-flight: A simple method for measuring microliter per minute flows without calibration. Sensors and Actuators A: Physical. 2012 April 2012;177:60-6.

75. Togawa T, Nemoto T, Tsubakimoto H. Thermal pulse flowmeter. 1984.

76. Poghossian A, Berndsen L, Schöning MJ. Chemical sensor as physical sensor: ISFET-based flow-velocity, flow-direction and diffusion-coefficient sensor. Sensors and Actuators B: Chemical. 2003 15 October 2003;95(1):384-90.

77. Sugarman JH, Prud'homme RK. Effect of photobleaching on the output of an on-column laser fluorescence detector. Ind Eng Chem Res. 1987;26(7):1449-54.

78. Wang G. Laser induced fluorescence photobleaching anemometer for microfluidic devices. Lab on a Chip. 2005;5(4):450-6.

79. Sharma P, Motte J, Fournel F, Cross B, Charlaix E, Picard C. A direct sensor to measure minute liquid flow rates. Nano Letters. 2018;18(9):5726-30.

80. Huang W, Seetasang S, Azizi M, Dasgupta PK. Functionalized Cycloolefin Polymer Capillaries for Open Tubular Ion Chromatography. Anal Chem. 2016 12/20;88(24):12013-20.

81. Conductance or Admittance? Q&More. http://q-more.chemeurope.com/q-more-articles/215/conductance-or-admittance.html.October 2015.

82. Zhang M, Stamos BN, Amornthammarong N, Dasgupta PK. Capillary scale admittance detection. Anal Chem. 2014;86(23):11538-46.

83. 3M. Fluorinert Electronic Liquid FC-40. http://multimedia.3m.com/mws/media/64888O/fluorinert-electronic-liquid-fc-40.pdf.

84. Zhang M, Stamos BN, Dasgupta PK. Admittance Detector for High Impedance systems: design and applications. Anal Chem. 2014;86(23):11547-53.

85. Takeuchi M, Li Q, Yang B, Dasgupta PK, Wilde VE. Use of a capacitance measurement device for surrogate noncontact conductance measurement. Talanta. 2008;76(3):617-20.

86. Chun H, Dennis PJ, Welch ERF, Alarie JP, Jorgenson JW, Ramsey JM. Development of a conductivity-based photothermal absorbance detection microchip using polyelectrolytic gel electrodes. Journal of Chromatography A. 2017;1523:140-7.

87. Huang W, Chouhan B, Dasgupta PK. Capillary Scale Admittance and Conductance Detection. Anal Chem. 2018;90(24):14561-8.

88. Stone J. Optical Transmission in Liquid-Core Quartz Fibers. Appl Phys Lett. 1972;20(7):239-41.

89. Walrafen G, Stone J. Intensification of spontaneous Raman spectra by use of liquid core optical fibers. Appl Spectrosc. 1972;26(6):585-9.

90. Wei L, Fujiwara K, Fuwa K. Determination of phosphorus in natural waters by long-capillary-cell absorption spectrometry. Anal Chem. 1983;55(6):951-5.

91. Dasgupta PK. Multipath cells for extending dynamic range of optical absorbance measurements. Anal Chem. 1984;56(8):1401-3.

92. Fuwa K, Lei W, Fujiwara K. Colorimetry with a total-reflection long capillary cell. Anal Chem. 1984;56(9):1640-4.

93. Fujiwara K, Fuwa K. Liquid core optical fiber total reflection cell as a colorimetric detector for flow injection analysis. Anal Chem. 1985;57(6):1012-6.

94. DuPont™ Teflon® AF. Amorphous Fluoroplastic Resin. https://www.chemours.com/Teflon_Industrial/en_US/assets/downloads/h44015.pdf. Last accessed June 26, 2019.

95. Yang MK, French RH, Tokarsky EW. Optical properties of Teflon® AF amorphous fluoropolymers. Journal of Micro/Nanolithography, MEMS, and MOEMS. 2008;7(3):033010.

96. Pinnau I, Toy LG. Gas and vapor transport properties of amorphous perfluorinated copolymer membranes based on 2, 2-bistrifluoromethyl-4, 5-difluoro-1, 3-dioxole/tetrafluoroethylene. J Membr Sci. 1996;109(1):125-33.

97. Dasgupta PK, Genfa Z, Poruthoor SK, Caldwell S, Dong S, Liu S. High-sensitivity gas sensors based on gas-permeable liquid core waveguides and long-path absorbance detection. Anal Chem. 1998;70(22):4661-9.

98. Dasgupta PK, Liu SY. Chemical sensing techniques employing liquid-core optical fibers. 2000.

99. Liao H, Dasgupta PK. Permeative amine introduction for very weak acid detection in ion chromatography. Anal Chem. 2016;88(4):2198-204.

100. Liao H, Shelor CP, Dasgupta PK. Water ICE: Ion exclusion chromatography of very weak acids with a pure water eluent. Anal Chem. 2016;88(9):4965-70.

101. Ganranoo L, Mishra SK, Azad AK, Shigihara A, Dasgupta PK, Breitbach ZS, et al. Measurement of Nitrophenols in Rain and Air by Two-Dimensional Liquid Chromatography− Chemically Active Liquid Core Waveguide Spectrometry. Anal Chem. 2010;82(13):5838-43.

102. Shelor CP, Dasgupta PK. Automated programmable pressurized carbonic acid eluent ion exclusion chromatography of organic acids. Journal of Chromatography A. 2017;1523:300-8.

103. Shelor CP, Yoshikawa K, Dasgupta PK. Automated programmable preparation of carbonate-bicarbonate eluents for ion chromatography with pressurized carbon dioxide. Anal Chem. 2017;89(18):10063-70.

104. Zuman P, Szafranski W. Ultraviolet spectra of hydroxide, alkoxide, and hydrogen sulfide anions. Anal Chem. 1976;48(14):2162-3.

105. May J, Hickey M, Triantis I, Palazidou E, Kyriacou PA. Spectrophotometric analysis of lithium carbonate used for bipolar disorder. Biomedical optics express. 2015;6(3):1067-73.

106. Dress P, Franke H. A cylindrical liquid-core waveguide. Applied Physics B. 1996;63(1):12-9.

107. Dress P, Franke H. Optical fiber with a liquid H2O core. Integrated Optics and Microstructures III; International Society for Optics and Photonics; 1996.

108. Dress P, Franke H. Increasing the accuracy of liquid analysis and p H-value control using a liquid-core waveguide. Rev Sci Instrum. 1997;68(5):2167-71.

109. Manor R, Datta A, Dhar A, Holtz M, Berg J, Gangopadhyay S, et al. Microfabricated liquid core waveguides for microanalysis systems. SENSORS, 2002 IEEE; IEEE; 2002.

110. Dallas T, Dasgupta PK. Light at the end of the tunnel: recent analytical applications of liquid-core waveguides. TrAC Trends in Analytical Chemistry. 2004;23(5):385-92.

111. Kraiczek KG, Rozing GP, Zengerle R. Relation between chromatographic resolution and signal-to-noise ratio in spectrophotometric HPLC detection. Anal Chem. 2013;85(10):4829-35.

112. Gilby A, Carson W. Patent 5,184,192, February 2, 1993. There is no corresponding record for this reference.[Google Scholar].

113. http://www.waters.com/webassets/cms/library/docs/720001322en.pdf. Last accessed June 26, 2019.

114. Thermo Scientific. Accela PDA Detector. http://tools.thermofisher.com/content/sfs/manuals/AccelaPDADet-Hardware.pdf. Last accessed June 26, 2019.

115. Larsson H, Dasgupta PK. Liquid core waveguide-based optical spectrometry for field estimation of dissolved BTEX compounds in groundwater: A feasibility study. Anal Chim Acta. 2003;485(2):155-67.

116. Liu S. Aqueous fluid core waveguide. 1996.

117. WPI, Inc. Liquid Waveguide Capillary Cell. https://www.wpiinc.com/spectroscopy/flow-cells/long-path-flow-cells. Last accessed June 26, 2019.

118. Yao W, Byrne RH, Waterbury RD. Determination of nanomolar concentrations of nitrite and nitrate in natural waters using long path length absorbance spectroscopy. Environ Sci Technol. 1998;32(17):2646-9.

119. Testa G, Persichetti G, Bernini R. Liquid core arrow waveguides: A promising photonic structure for integrated optofluidic microsensors. Micromachines. 2016;7(3):47.

120. Guerra M, Sanchez A, Javan A. v= 2← 1 Absorption spectroscopy of vibrationally heated NO molecules using optical pumping in a wave guide. Phys Rev Lett. 1977;38(9):482.

121. Schwab SD, McCreery RL. Remote, long-pathlength cell for high-sensitivity Raman spectroscopy. Appl Spectrosc. 1987;41(1):126-30.

122. TsUNODA K, NOMURA A, YAMADA J, NIsHI S. Long capillary cell with the use of successive total reflection at outer cell surface for liquid absorption spectrometry. Analytical sciences. 1988;4(3):321-3.

123. Tsunoda K, Nomura A, Yamada J, Nishi S. The possibility of signal enhancement in liquid absorption spectrometry with a long capillary cell utilizing successive total reflection at the outer cell surface. Appl Spectrosc. 1989;43(1):49-55.

124. Agilent Technologies. Agilent Infinitylab LC Series. Diode Array Detectors. http://agilent.com/cs/library/usermanuals/public/G7117ABCUser.pdf Last accessed June 26, 2019.

125. Shimadzu Scientific. High Sensitivity Cell. https://www.shimadzu.it/high-sensitivity-cell-optional Last accessed June 26, 2019.

126. Kraiczek K, Mannion J, Post S, Tsupryk A, Raghunathan V, Brennen R, et al. Micromachined fused silica liquid core waveguide capillary flow cell. Anal Chem. 2015;88(2):1100-5.

127. Ruzicka JJ. Redesigning flow injection after 40 years of development: Flow programming. Talanta. 2018;176:437-43.

128. Hatta M, Measures CI, Ruzicka JJ. Programmable Flow Injection. Principle, methodology and application for trace analysis of iron in a sea water matrix. Talanta. 2018;178:698-703.

129. Christian S.; Christian, G. A Short History of FIAlab Instruments. http://www.flowinjectiontutorial.com/History%205.3.1..html Last accessed June 26, 2019.

130. Toda K, Yoshioka K, Ohira S, Li J, Dasgupta PK. Trace gas measurement with an integrated porous tube collector/long-path absorbance detector. Anal Chem. 2003;75(16):4050-6.

131. Li J, Li Q, Dyke JV, Dasgupta PK. Atmospheric ozone measurement with an inexpensive and fully automated porous tube collector-colorimeter. Talanta. 2008;74(4):958-64.

132. Tian Y, Dasgupta PK, Mahon SB, Ma J, Brenner M, Boss GR. A disposable blood cyanide sensor. Anal Chim Acta. 2013;768:129-35.

133. International Union of Pure and Applied Chemistry. Beer–Lambert law (or Beer–Lambert–Bouguer law). https://goldbook.iupac.org/plain/B00626-plain.html Last accessed June 26, 2019.

134. American Meteorological Society. Glossary of Meteorology. http://glossary.ametsoc.org/wiki/Bouguer's_law Last accessed June 26, 2019.

135. Liu H, Dasgupta PK, Zheng HJ. High performance optical absorbance detectors based on low noise switched integrators. Talanta. 1993;40(9):1331-8.

136. Schottky W. Über spontane Stromschwankungen in verschiedenen Elektrizitätsleitern. Annalen der physik. 1918;362(23):541-67.

137. Wahab MF, Reising AE. The Ultimate Limit in Measurements by Instrumental Analysis: An Interesting Account of Schroteffekt and Shot Noise. J Chem Educ. 2018;95(9):1668-71.

138. McClain RL, Wright JC. Description of the Role of Shot Noise in Spectroscopic Absorption and Emission Measurements with Photodiode and Photomultiplier Tube Detectors: Information for an Instrumental Analysis Course. J Chem Educ. 2014;91(9):1455-7.

139. McCreery RL. Raman spectroscopy for chemical analysis. John Wiley & Sons; 2005.

140. Ibsen Photonics. Noise in Detectors for Spectroscopy. 2019. https://ibsen.com/technology/detector-tutorial/noise-in-detectors/.

141. Pereplitsa, D. V. Johnson Noise and Shot Noise. 2004. https://web.mit.edu/dvp/Public/noise-paper.pdf.

142. Ingle, J. D.; Crouch S. R. Spectrochemical Analysis, Prentice Hall: Englewood Cliffs, NJ, 1988. pp 141-144.

143. Xu Z, Larsen DW. Development of ultra-low-noise spectrophotometry for analytical applications. Anal Chem. 2005;77(19):6463-8.

144. Culbertson CT, Jorgenson JW. Lowering the UV absorbance detection limit and increasing the sensitivity of capillary electrophoresis using a dual linear photodiode array detector and signal averaging. J Microcolumn Sep. 1999;11(9):652-62.

145. Durry G, Pouchet I, Amarouche N, Danguy T, Megie G. Shot-noise-limited dual-beam detector for atmospheric trace-gas monitoring with near-infrared diode lasers. Appl Opt. 2000;39(30):5609-19.

146. Sonnenfroh DM, Allen MG. Ultrasensitive, visible tunable diode laser detection of NO 2. Appl Opt. 1996;35(21):4053-8.

147. Jones K, Malcolme-Lawes DJ. High-performance ultraviolet absorption detector for liquid chromatography: I. Preliminary Experiments. Journal of Chromatography A. 1985;329:25-32.

148. Baumann W. Optische Detektoren in der Flüssigkeits-Chromatographie. Fresenius' Zeitschrift für analytische Chemie. 1977;284(1):31-8.

149. Poppe H. The performance of some liquid phase flow-through detectors. Anal Chim Acta. 1983;145:17-26.

150. Bergström ET, Goodall DM, Pokrić B, Allinson NM. A charge coupled device array detector for single-wavelength and multiwavelength ultraviolet absorbance in capillary electrophoresis. Anal Chem. 1999;71(19):4376-84.

151. Aiello M, McLaren R. A sensitive small-volume UV/Vis flow cell and total absorbance detection system for micro-HPLC. Anal Chem. 2001;73(6):1387-92.

152. Tsih, I.T.; Salerno, M. Validating Slope Spectroscopy Methods: A Formula for Robust Measurements. https://cdn.technologynetworks.com/TN/Resources/PDF/spwp2.pdf. Last accessed June 26, 2019.

153. Dasgupta PK, Shelor CP, Kadjo AF, Kraiczek KG. Flow-Cell-Induced Dispersion in Flow-through Absorbance Detection Systems: True Column Effluent Peak Variance. Anal Chem. 2018;90(3):2063-9.

154. Agilent Technologies. Agilent 1200 Infinity Series High Dynamic Range Diode Array Detector Solution. User Guide. http://www.agilent.com/cs/library/usermanuals/Public/HDR_USR_EN.pdf Last accessed June 26, 2019.

155. Leveille MJ, DeLuca JM. Approach to short measurement path-length flow cells. 2004.

156. Tsukamoto M. Comparaison entre l'absorption par l'eau et celle par le quartz dans l'UV-lointain. Rev.opt. 1928;7:89-108.

157. Buiteveld H, Hakvoort J, Donze M. Optical properties of pure water. Ocean Optics XII; International Society for Optics and Photonics; 1994.

158. Prahl, S.; Jacques S. Light Absorption by Water. https://omlc.org/spectra/water/index.html Last accessed June 26, 2019.

159. Hale GM, Querry MR. Optical constants of water in the 200-nm to 200-μm wavelength region. Appl Opt. 1973;12(3):555-63.

160. Pope RM, Fry ES. Absorption spectrum (380–700 nm) of pure water. II. Integrating cavity measurements. Appl Opt. 1997;36(33):8710-23.

161. Mason JD, Cone MT, Fry ES. Ultraviolet (250–550 nm) absorption spectrum of pure water. Appl Opt. 2016;55(25):7163-72.

162. Lu, Z, Optical Absorption of Pure Water in the Blue and Ultraviolet. PhD Dissertation, Texas A&M University, May, 2006. http://hdl.handle.net/1969.1/5828.

163. https://www.wpiinc.com/pub/media/wysiwyg/pdf/DS/LWCC.pdf Last accessed June 26, 2019.

164. Weidner VR, Hsia JJ. Reflection properties of pressed polytetrafluoroethylene powder. JOSA. 1981;71(7):856-61.

165. Silva C, Pinto da Cunha J, Pereira A, Chepel V, Lopes M, Solovov V, et al. Reflectance of polytetrafluoroethylene for xenon scintillation light. J Appl Phys. 2010;107(6):064902.

166. Nutter S, Bower C, Gebhard M, Heinz R, Spiczak G. Sintered Halon as a diffuse reflecting liner for light integration boxes. Nuclear Instruments and Methods in Physics Research Section A: Accelerators, Spectrometers, Detectors and Associated Equipment. 1991;310(3):665-70.

167. Tsai BK, Allen DW, Hanssen LM, Wilthan B, Zeng J. A comparison of optical properties between high density and low density sintered PTFE. Reflection, Scattering, and Diffraction from Surfaces; International Society for Optics and Photonics; 2008.

168. Li Y, Shelor CP, Dasgupta PK. Nonlinear Absorbance Amplification Using a Diffuse Reflectance Cell: Total Organic Carbon Monitoring at 214 nm. Anal Chem. 2014;87(2):1111-7.

169. Braun CL, Smirnov SN. Why is water blue? J Chem Educ. 1993;70(8):612.

170. Afif C, Jambert C, Michoud V, Colomb A, Eyglunent G, Borbon A, et al. NitroMAC: An instrument for the measurement of HONO and intercomparison with a long-path absorption photometer. Journal of Environmental Sciences. 2016;40:105-13.

171. Worsfold PJ, Clough R, Lohan MC, Monbet P, Ellis PS, Quétel CR, et al. Flow injection analysis as a tool for enhancing oceanographic nutrient measurements—A review. Anal Chim Acta. 2013;803:15-40.

172. Páscoa RN, Tóth IV, Rangel AO. Review on recent applications of the liquid waveguide capillary cell in flow based analysis techniques to enhance the sensitivity of spectroscopic detection methods. Anal Chim Acta. 2012;739:1-13.

173. Sinkov SI. Plutonium Speciation in Support of Oxidative-Leaching Demonstration Test. 2007.

174. Wang W, He Q, Wang T, Fen M, Liao Y, Ran G. Absorbance study of liquid-core optical fibers in spectrophotometry. Anal Chem. 1992;64(1):22-5.

175. Villena G, Bejan I, Kurtenbach R, Wiesen P, Kleffmann J. Development of a new Long Path Absorption Photometer (LOPAP) instrument for the sensitive detection of NO 2 in the atmosphere. Atmospheric Measurement Techniques. 2011;4(8):1663-76.

176. Kleffmann J, Lörzer J, Wiesen P, Kern C, Trick S, Volkamer R, et al. Intercomparison of the DOAS and LOPAP techniques for the detection of nitrous acid (HONO). Atmos Environ. 2006;40(20):3640-52.

177. Kleffmann J, Wiesen P. Quantification of interferences of wet chemical HONO LOPAP measurements under simulated polar conditions. Atmospheric Chemistry and Physics. 2008;8(22):6813-22.

178. Novak M, Mannino A, Nelson N, D'sa E, Miller R, Werdell J, et al. Measurements of CDOM absorption spectra using different instruments and techniques: a round robin exercise and extensive field data set. Ocean Optics XXII Conference; ; 2014.

Biographical Information

Chuchu Qin got her B.S. in Pharmaceutical Sciences from Central South University in China in 2012. After that, she came to the United States, continued her study in Pharmaceutical Sciences at the University of Pittsburgh and obtained a non-thesis M.S. in 2013 summer. She had realized she is not really into medicinal chemistry by the time. In 2013 fall, she became a PhD student in the chemistry department at the University of Texas at Arlington. She joined Dr. Dasgupta's group out of curiosity and finally found the enthusiasm and sense of accomplishment that she couldn't find before.

Under Dr. Dasgupta's supervision, Chuchu mainly worked on designing and developing novel sensing strategies and instruments for ultra-low liquid flow measurement. She developed inline hydrocephalus flow sensor and nano flow sensor.